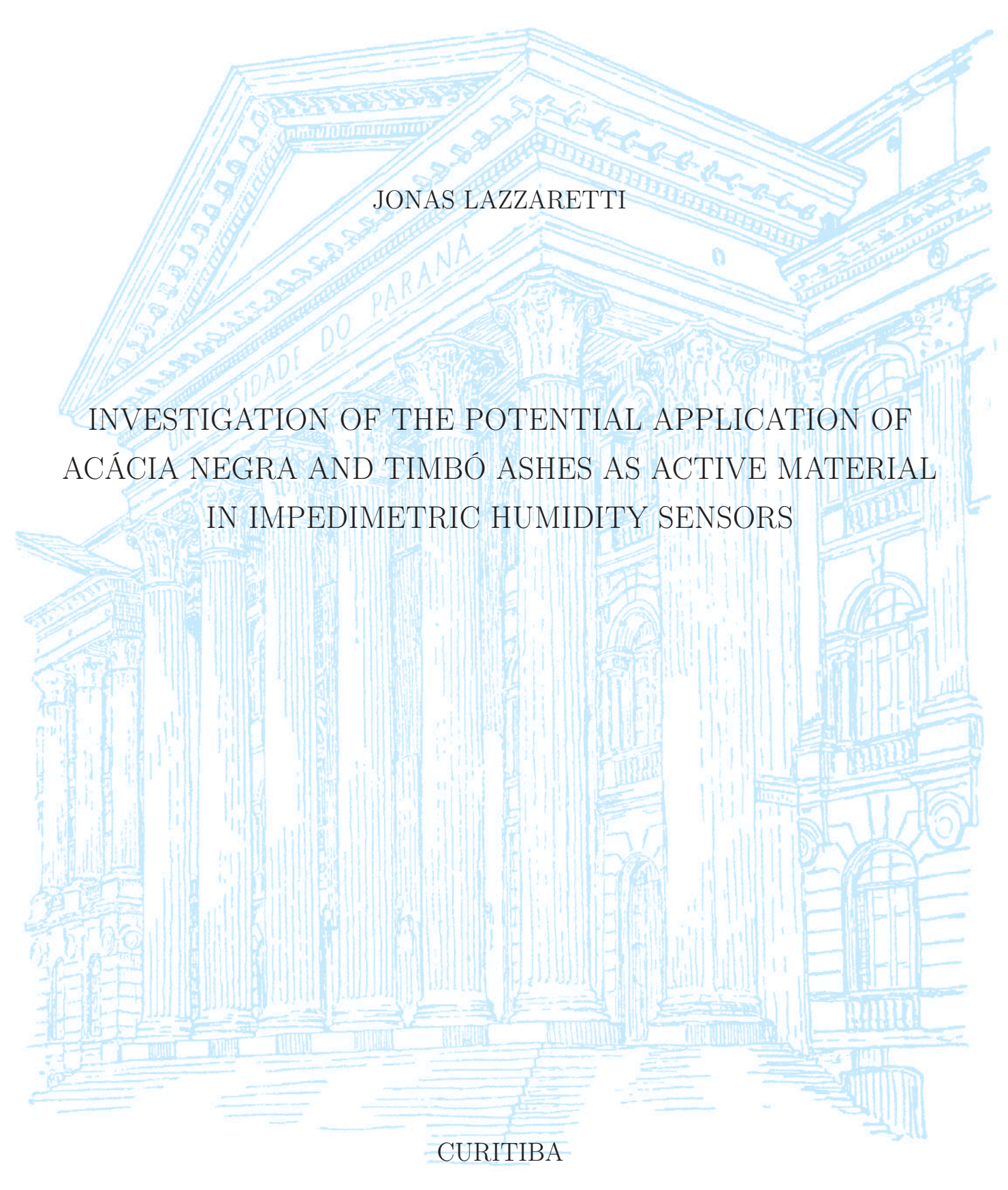
UNIVERSIDADE FEDERAL DO PARANÁ



2025

JONAS LAZZARETTI

INVESTIGATION OF THE POTENTIAL APPLICATION OF ACÁCIA NEGRA AND TIMBÓ ASHES AS ACTIVE MATERIAL IN IMPEDIMETRIC HUMIDITY SENSORS

Tese apresentada como requisito parcial para a obtenção do título de Doutor em Física no Departamento de Física da Universidade Federal do Paraná.

Orientador: Prof. Dr. José Pedro Mansueto Serbena

CURITIBA

DADOS INTERNACIONAIS DE CATALOGAÇÃO NA PUBLICAÇÃO (CIP) UNIVERSIDADE FEDERAL DO PARANÁ SISTEMA DE BIBLIOTECAS – BIBLIOTECA DE CIÊNCIA E TECNOLOGIA

Lazzaretti. Jonas

Investigation of the potential application of acácia negra and timbó ashes as active material in impedimetric humidity sensors / Jonas Lazzaretti. – Curitiba, 2025.

1 recurso on-line: PDF.

Tese (Doutorado) - Universidade Federal do Paraná, Setor de Exatas, Programa de Pós-Graduação em Física.

Orientador: José Pedro Mansueto Serbena

1. Umidade. 2. Biomassa. 3. Análise espectral. 4. Acácia (Planta). 5. Timbó (Planta). 6. Materiais – Aspectos ambientais. I. Universidade Federal do Paraná. II. Programa de Pós-Graduação em Física. III. Serbena, José Pedro Mansueto. IV. Título.

Bibliotecário: Douglas Lenon da Silva CRB-9/1892



MINISTÉRIO DA EDUCAÇÃO
SETOR DE CIÊNCIAS EXATAS
UNIVERSIDADE FEDERAL DO PARANÁ
PRÓ-REITORIA DE PÓS-GRADUAÇÃO
PROGRAMA DE PÓS-GRADUAÇÃO FÍSICA - 40001016020P4

TERMO DE APROVAÇÃO

Os membros da Banca Examinadora designada pelo Colegiado do Programa de Pós-Graduação FÍSICA da Universidade Federal do Paraná foram convocados para realizar a arguição da tese de Doutorado de JONAS LAZZARETTI, intitulada: "Investigation of the Potential Application of Acácia Negra and Timbó Ashes as Active Material in Impedimetric Humidity Sensors", sob orientação do Prof. Dr. JOSÉ PEDRO MANSUETO SERBENA, que após terem inquirido o aluno e realizada a avaliação do trabalho, são de parecer pela sua APROVAÇÃO no rito de defesa.

A outorga do título de doutor está sujeita à homologação pelo colegiado, ao atendimento de todas as indicações e correções solicitadas pela banca e ao pleno atendimento das demandas regimentais do Programa de Pós-Graduação.

CURITIBA, 27 de Agosto de 2025.

Assinatura Eletrônica 27/08/2025 14:20:03.0 JOSÉ PEDRO MANSUETO SERBENA Presidente da Banca Examinadora

Assinatura Eletrônica 27/08/2025 13:37:55.0 NEY PEREIRA MATTOSO FILHO Avaliador Externo (UNIVERSIDADE FEDERAL DO PARANÁ) Assinatura Eletrônica 27/08/2025 20:32:28.0 CARLOS FREDERICO DE OLIVEIRA GRAEFF Avaliador Externo (UNIVERSIDADE EST.PAULISTA JÚLIO DE MESQUITA FILHO/BAURU)

Assinatura Eletrônica 27/08/2025 14:07:58.0 ISMAEL LEANDRO GRAFF Avaliador Interno (UNIVERSIDADE FEDERAL DO PARANÁ)

ACKNOWLEDGEMENTS

First and foremost, I would like to express my heartfelt gratitude to my family, especially my parents, Valdir Lazzaretti and Cecília Lermen Lazzaretti, for their unconditional love and unwavering support throughout all these years of academic pursuit. It is much easier to have the courage to chase one's dreams when you know there will always be a place to return to if everything goes wrong.

I would also like to thank the Federal University of Paraná (UFPR) for providing the infrastructure necessary for this research. My sincere thanks extend to all members of the Group of Optoelectronic Organic Devices (GOOD) for their companionship, support, and assistance, especially to my colleagues in the sensors research area: Renan Barbieri Estefani and Thayna Lunetta Grimaldi. I am particularly grateful to my advisor, Prof. José Pedro Mansueto Serbena, who was always able to offer solutions to the problems that kept me awake at night.

I am also thankful to the laboratories and research facilities that contributed to this thesis: the Center for Electron Microscopy (CME-UFPR), the Multi-User Infrared Absorption Spectroscopy Laboratory (LaMIV-UFPR), and the Gleb Wataghin Physics Institute (IFGW-Unicamp). Each of these contributions was essential for the development and consolidation of this research.

Lastly, I am grateful for the wide circle of friendships I have built during my time in Curitiba. These friends played a key role in making me feel at home in this city, turning my years here into a truly rewarding and memorable chapter of my life.

This study was financed in part by the Coordenação de Aperfeiçoamento de Pessoal de Nível Superior – Brasil (CAPES) – Finance Code 001.



RESUMO

Este estudo apresenta o desenvolvimento e a caracterização de sensores de umidade baseados em cinzas de biomassa derivadas da Acácia Negra e do Timbó. Um método de fabricação foi estabelecido, resultando em dispositivos com respostas exponenciais consistentes às variações na umidade relativa (RH). Os materiais foram analisados estruturalmente por meio de Microscopia Eletrônica de Varredura (MEV), Espectroscopia de Energia Dispersiva (EDS), Espectroscopia de Fotoelétrons Excitados por Raios X (XPS) e Espectroscopia de Infravermelho por Transformada de Fourier (FTIR). As análises de EDS e XPS revelaram a predominância de O, Ca, C, K nas regiões centrais das deposições, e principalmente O, C e K nas bordas. A análise de FTIR sugeriu a presença de CaCO₃, embora testes experimentais tenham descartado a participação deste composto na resposta dos dispositivos. A caracterização elétrica foi realizada por espectroscopia de impedância elétrica em 1 kHz, revelando dois regimes distintos de sensibilidade: abaixo e acima de 50% RH. As sensibilidades dos dispositivos baseados em Acácia Negra foram de $0.10 \ \mathrm{dec} \cdot (\%\mathrm{RH})^{-1} = 0.04 \ \mathrm{dec} \cdot (\%\mathrm{RH})^{-1}$, enquanto os dispositivos baseados em Timbó apresentaram sensibilidades de 0,13 dec $\cdot (\%RH)^{-1}$ e 0,05 dec $\cdot (\%RH)^{-1}$. Os limites de detecção foram de 22% e 23% RH, com tempos de resposta/recuperação de 18/37 s e 12/46 s, respectivamente. Para interpretar o mecanismo de detecção, foi proposto um modelo de circuito equivalente, composto por um elemento de fase constante (CPE) representando o material de base e uma associação em série R-CPE representando a condução iônica decorrente da adsorção de água. Os resultados demonstram o potencial das cinzas de biomassa como materiais sustentáveis para aplicações em sensores de umidade de baixo custo.

Palavras-chave: Sensor de umidade; Cinza de biomassa; Espectroscopia de impedância; Acácia Negra; Timbó; Materiais sustentáveis; Umidade relativa.

ABSTRACT

This study presents the development and characterization of humidity sensors based on biomass ash derived from Acácia Negra and Timbó. A fabrication method was established, resulting in devices with consistent exponential responses to variations in relative humidity (RH). The materials were structurally analyzed using Scanning Electron Microscopy (SEM), Energy-dispersive X-ray Spectroscopy (EDS), X-ray Photoelectron Spectroscopy (XPS), and Fourier Transform Infrared Spectroscopy (FTIR). EDS and XPS analyses revealed the predominance of O, Ca, C, and K in the central regions of the depositions, and mainly O, C, and K at the edges. FTIR analysis suggested the presence of CaCO₃, although experimental tests ruled out the participation of this compound in the device response. Electrical characterization was carried out by electrical impedance spectroscopy at 1 kHz, revealing two distinct sensitivity regimes: below and above 50% RH. The sensitivities of the Acacia Negra-based devices were $0.10 \, \mathrm{dec} \cdot (\% \mathrm{RH})^{-1}$ and $0.04 \, \mathrm{dec} \cdot (\% \mathrm{RH})^{-1}$, while the Timbó-based devices presented sensitivities of 0.13 dec \cdot (%RH)⁻¹ and 0.05 dec \cdot (%RH)⁻¹. The detection limits were 22% and 23% RH, with response/recovery times of 18/37 s and 12/46 s, respectively. To interpret the sensing mechanism, an equivalent circuit model was proposed, consisting of a constant phase element (CPE) representing the base material and a series R-CPE association representing ionic conduction due to water adsorption. The results demonstrate the potential of biomass ash as a sustainable material for low-cost humidity sensor applications.

Keywords: Humidity sensor; Biomass ash; Impedance spectroscopy; Acácia Negra; Timbó; Sustainable materials; Relative humidity.

LIST OF FIGURES

Figure 1 –	Areas where humidity control is crucial, including health, indoor air quality,	
	industry and electronics	16
Figure 2 –	Wearable humidity sensor based on paper ash to monitor humidity and	17
		17
Figure 3 –	Schematic representation of an olfactory system of a dog illustrating the components and stages of the chemical sensing process	20
Figure 4 –	Representation of physisorption and chemisorption of a gas on a solid surface.	23
Figure 5 –	Humidity interaction mechanisms	24
Figure 6 –	Illustrative example of (a) time series (response curve) and (b) calibration	
	curve for a sensor	25
Figure 7 –	Representation of the response and recovery times in the response curve	26
Figure 8 –	Representation of the relation between signal and noise and the response of	
	the limit of detection (R_{LoD})	27
Figure 9 –	Acácia Negra cultivation in Rio Grande do Sul, Brazil (a) and an adult-sized	
	Acácia Negra in Australia (b)	30
Figure 10 –	Photos of (a) an adult-sized Timbó and (b) the typical bark of the tree	31
Figure 11 –	Signals and their representation as phasors in the complex plane. To produce	
	the waves, the phasors rotate counterclockwise with angular frequency ω and	
	the current phasor is ϕ radians ahead of the voltage	35
Figure 12 –	Bode plots for (a) modulus and (b) phase of a resistor and a capacitor in	
	series, R-C, and in parallel, (R,C). In this simulation, $R=1$ Ohm and $C=1$ F.	37
Figure 13 –	Nyquist graphs for a resistor and a capacitor (a) in series, R-C, and (b) in	
	parallel, (R,C). In this simulation, $R=1$ Ohm and $C=1$ F	38
Figure 14 –	Bode (a,b) and Nyquist (c,d) plots for circuits containing a CPE with $T=$	
	$1 F \cdot s^{1-\alpha}$ and $\alpha = 0,5,\ldots$	41
Figure 15 –	Structure of the humidity sensor based on Acácia Negra and Timbó ash	43

Figure 16 –	Schematic representation of the deposition method. The substrate is first cleaned using ultrasonic baths in acetone, deionized water, and isopropyl alcohol at 60 °C for 20 minutes each, followed by drying in a vacuum stove and treatment with U.V./O ₃ . The sensing material is prepared by dispersing $10\mathrm{mg}$ of ash in $1\mathrm{mL}$ of deionized water using an ultrasonic bath, and $20\mu\mathrm{L}$ of the resulting dispersion is deposited on the substrate by drop casting. Finally, the sample is dried again in a vacuum stove	45
Figure 17 –	Schematic representation of the gas flow system used for relative humidity control during sensor testing. (1) Nitrogen generator; (2) silica-based humidity filter; (3) pressure regulator; (4–5) flowmeters; (6) bubbler containing the analyte (water); (7) gas mixer; (8) sealed test chamber; (9) potentiostat for impedance measurements; (10) computer; (11) airlock with glycerin for maintaining constant flow and pressure. Flow 1 is the dry dilution stream, and flow 2 is the humidified stream. Relative humidity inside the chamber is	
	controlled by adjusting these flows	46
Figure 18 –	EDS spectra of (a) Acácia Negra and (b) Timbó ash	48
Figure 19 –	XPS spectra of (a) Acácia Negra and (b) Timbó ash	49
Figure 20 –	FTIR spectrum for (a) Acácia Negra and (b) Timbó ash, and (c) far infrared spectrum of Timbó ash	50
Figure 21 –	SEM images of the center part of the deposition site from a device based on Timbó ash with magnifications of 500x (a), 2 kx (b), 5 kx (c), 10 kx (d), 20 kx (e) and 60 kx (f)	51
Figure 22 –	SEM images of the border of the deposition site from a device based on Timbó ash with magnifications of 1 kx (a), 5 kx (b), 20 kx (c)	52
Figure 23 –	SEM images of the center and border parts of the deposition site from a device based on Acácia Negra ash. (a), (b) and (c) are the center region with 1 kx, 20 kx, and 60 kx magnification, respectively, and (d), (e), and (f) are the border, with 900 x, 5 kx, and 20 kx magnification	53
Figure 24 –	EDS spectra for Timbó and Acácia Negra ash over FR4 substrate. (a) and (b) show the results for Timbó in the center and border of the deposition site, respectively, and (c) and (d) for Acácia Negra, center and border	54

Figure 25 -	- Nyquist plot for sensor based on (a) Acácia Negra and (b) Timbó ash, for				
	frequencies ranging from 0,5 Hz to 200 kHz	55			
Figure 26 –	Nyquist plot for sensors based on (a) Acácia Negra and (b) Timbó ash in				
	logarithmic scale, for frequencies ranging from 0,5 Hz to 200 kHz	56			
Figure 27 –	Bode graphs for the (a) modulus, (b) the phase, (c) the real and (d) imaginary				
	parts of the electric impedance of a sensor based on Acácia Negra ash, in				
	different concentrations	57			
Figure 28 –	Evolution of the four parameters: (a) modulus, (b) phase, (c), real part, and				
	(d) imaginary part of the impedance, with increasing relative humidity, for				
	some representative frequencies	58			
Figure 29 –	Calibration curve of (a) the modulus and (b) the imaginary part of the electric				
	impedance for some representative frequencies, using the lower concentration				
	(10%) as the blank, for Acácia Negra based sensors	59			
Figure 30 –	Time series for the modulus of the electric impedance ($ \mathbf{Z} $) at 1 kHz and				
	corresponding calibration curve for samples based on (a-b) Acácia Negra and				
	(c-d) Timbó	61			
Figure 31 –	Calibration for (a) Acácia Negra and (b) Timbó showing the 2 regimes of				
	sensor operation. Limit of detection lines are presented for both cases	62			
Figure 32 –	Calibration curve obtained from the spectroscopy, using the lower concentra-				
	tion (10 %) as the blank value, for (a) Acácia Negra and (b) Timbó	63			
Figure 33 –	Time series measurements for obtaining the response and recovery times for				
	(a) Acácia Negra and (b) Timbó. The response and recovery intervals are				
	marked as red and blue rectangles, respectively	64			
Figure 34 –	Time series for the modulus of the electric impedance ($ \mathbf{Z} $) at (a) 10, (b) 100,				
	(c) 10 k, and (d) 100 kHz for samples based on Timbó ash $\ \ldots \ \ldots \ \ldots$	65			
Figure 35 –	Nyquist plot (a) and time series (b) for a sample based on $CaCO_3$	67			
Figure 36 –	Nyquist diagram for (a) Acácia Negra and (b) Timbó devices at 40 $\%$ and 30				
	% RH, respectively	67			
Figure 37 –	Bode graph for (a) modulus and (b) phase. The points represent experimen-				
	tal data for various concentrations and the dashed line corresponds to the				
	simulated capacitor of 0.135 nF	68			

Figure 38 –	Bode graphs for (a) modulus and (b) real part of the electric impedance with	
	the simulation of a CPE. The points represent experimental data for various	
	concentrations and the dashed line corresponds to the simulated CPE with	
	exponent $\alpha = 0.99$ and T = 0.135 $n(F.s^{\alpha-1})$	69
Figure 39 –	Bode graph for (a) modulus and (b) phase of a device based on Acácia	
	Negra, at 40% RH, with CPE1 and R-CPE2 simulated. The points represent	
	experimental data and the dashed lines correspond to the simulations: CPE1	
	with exponent $\alpha_1 = 0.99$ and $T_1 = 0.135$ nF \cdot s ^{α_1-1} for the high-frequency	
	regime, and R-CPE2 with $R=3.2\times10^5~\Omega,~\alpha_2=0.38$ and $T_2=1\times10^{-6}~\mathrm{F\cdot s^{\alpha_2-1}}$	
	for low-frequency	70
Figure 40 –	Proposed equivalent circuit (a) and the simulated curves in (b) the Nyquist	
	plot and the Bode graphs for (c) the modulus and (d) the phase of the	
	electric impedance of a device based on Acácia Negra at 40% RH. The points	
	represent experimental data while the dashed line corresponds to the simulated	
	circuit with the following parameters: $\alpha_1 = 0.99$, $T_1 = 0.135 \text{ nF} \cdot \text{s}^{\alpha_1 - 1}$,	
	$R = 3.2 \times 10^5 \ \Omega, \ \alpha_2 = 0.38, \ T_2 = 1 \times 10^{-6} \ F \cdot s^{\alpha_2 - 1}. \dots \dots \dots \dots$	71
Figure 41 –	Simulation of the equivalent circuit for (a) Acácia Negra and (c) Timbó and	
	their parameter values by concentration (b,d)	72

LIST OF TABLES

Table 1 –	Humidity sensors in the literature. Materials marked with (*) are biomass-	
	based devices	28
Table 2 -	Characterization parameters for Acácia Negra and Timbó ash based devices	75
Table 3 -	Comparison between this work and similar studies from the literature	76

LIST OF SYMBOLS

- Z Impedance (complex), in Ω
- R Resistance, in Ω
- C Capacitance, in F
- i Imaginary unit, $i=\sqrt{-1}$
- ω Angular frequency, in rad/s
- f Frequency, in Hz
- Re(Z) Real part of the impedance
- Im(Z) Imaginary part of the impedance
- |Z| Modulus of the impedance
- ϕ Phase angle of the impedance, in degrees
- RH Relative humidity, in %
- RR Relative response (dimensionless)
- CPE Constant phase element
- α Exponent of the Constant Phase Element (CPE)
- T Impedance parameter of the CPE, in $(F\cdot s^{1-\alpha})$
- I Electric current
- V Voltage

CONTENTS

1	INTRO	DUCTION	16
2 HUMIDITY SENSORS, BIOMASS ASH AND ELECTRIC IMPED			
	ANALY	YSIS	19
	2.1	Humidity Sensors	19
	2.1.1	Humidity	20
	2.1.2	Humidity Interactions	22
	2.1.3	Characterization Parameters	24
	2.1.3.1	Sensitivity	24
	2.1.3.2	Response And Recovery Times	25
	2.1.3.3	Limit Of Detection (LoD)	26
	2.1.4	State Of The Art	27
	2.2	Biomass ash	28
	2.2.1	Acácia Negra	29
	2.2.2	Timbó	30
	2.2.3	Structural Characterization Techniques	30
	2.2.3.1	Scanning Electron Microscopy (SEM) and Energy-dispersive X-ray	
		Spectroscopy (EDS)	31
	2.2.3.2	X-ray Photoelectron Spectroscopy (XPS)	32
	2.2.3.3	Fourier Transform Infrared Spectroscopy (FTIR)	32
	2.3	Electric Impedance Analysis	33
	2.3.1	Electric Impedance	33
	2.3.2	Electric Impedance of Basic Elements and Circuits	35
3	IMPED	IMETRIC HUMIDITY SENSORS BASED ON ACÁCIA NEGRA	
	AND T	IMBÓ ASH	43
	3.1	Introduction	43
	3.2	Experimental	43
	3.3	Results and Discussions	47
	3.3.1	Structural Characterization	47

	3.3.2	Electric Impedance Spectroscopy	53		
	3.3.3	Sensor Characterization	60		
	3.3.4	Equivalent Circuits	66		
	3.3.4.1	Analytic expression for the impedance of the proposed circuit \dots .	73		
	3.3.5	Comparisons	75		
4	CONCLU	JSIONS	77		
FUTURE WORK					
RE	EFERENC	ES	79		

Introduction

The amount of water vapour in a gas sample, referred to as humidity, is a critical factor in many everyday contexts. It influences human comfort and indoor air quality [1], health [2], and general well-being [3]. Humidity also plays an important role in industrial processes [4] and the operation of electronic devices [5], as illustrated in Figure 1.



Figure 1 – Areas where humidity control is crucial, including health, indoor air quality, industry and electronics.

Over the past few decades, many studies have investigated the impact of humidity on health, well-being, and productivity, particularly in office environments. Although there was initially some skepticism regarding the benefits of humidity control [1], research has shown that maintaining relative humidity between 40–60% can reduce adverse health effects and enhance productivity [6]. Following the COVID-19 pandemic, humidity was also identified as a factor influencing the transmission of influenza-like viruses. Once again, maintaining relative humidity within the 40–60% range, along with temperature control and adequate ventilation, is considered essential for promoting health and productivity in workplace environments [1].

For electronic devices, exposure to high humidity can cause defects and accelerate corrosion, compromising both performance and longevity. Therefore, accurate monitoring of humidity

levels is essential in environments where electronic components are densely concentrated [5].

In industrial applications, maintaining low humidity is a critical requirement in the production of various goods, such as lithium batteries, processed meat, and natural gas. It is also a key factor in storage environments, to prevent material degradation, mold growth, and corrosion over time [7].

As a result, the demand for humidity control in industrial and storage settings continues to grow. This calls for improvements not only in dehumidification processes, but also in humidity monitoring systems based on reliable sensors [8].

Humidity sensors can be manufactured from various materials, however, most commercial sensors are based on porous ceramic materials such as alumina [9], which, when produced in high purity, can be expensive and difficult to manufacture. Alternative materials include polymers and carbon-based substances, as well as more eco-friendly options like biomass materials or biomass ash. In this context, biomass ash offers a sustainable source of porous ceramics, allowing for the reuse of discarded biomass and contributing to waste reduction [10]. Due to their non-toxicity, these materials can be employed in applications such as wearable humidity sensors. For example, Figure 2 shows a sensor based on paper ash attached to a face mask, which monitors humidity and respiration rate in real time [11].

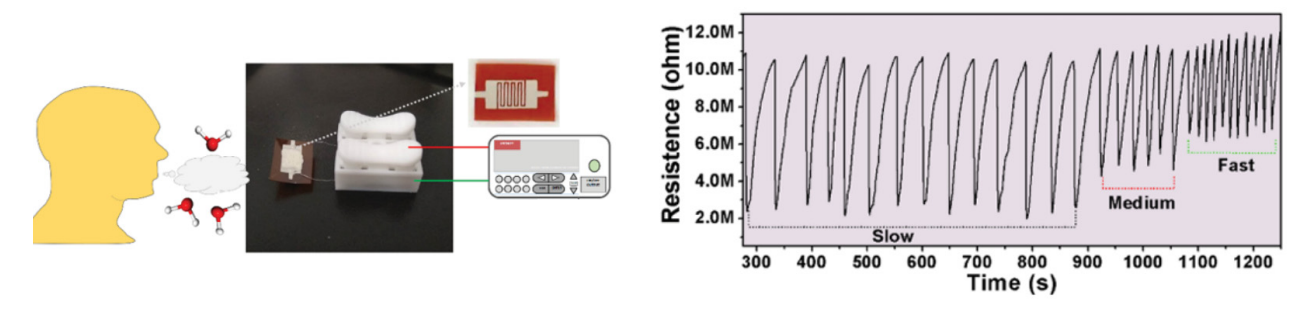


Figure 2 – Wearable humidity sensor based on paper ash to monitor humidity and respiration rate in human breath. Adapted from [11].

This work aims to develop relative humidity sensors using ash derived from the wood waste of two local tree species: Timbó and Acácia Negra. The study includes the characterization of the material's composition and the investigation of the sensing mechanism through electrical impedance spectroscopy. It builds upon a previous study conducted within the same research group [12], in which the development of sensors based on biomass ash was first explored. However, limitations in the experimental setup at the time led to inconclusive results and prevented full

sensor characterization. In the present study, significant improvements to the measurement system enabled the fabrication of reliable sensors, along with a comprehensive performance analysis and a detailed investigation of their operating behavior. Characterization techniques were employed to examine the composition of the sensing material. Furthermore, an equivalent circuit model was proposed to interpret the sensing mechanism, and a comparative analysis was carried out with similar sensors reported in the literature.

2

Humidity Sensors, Biomass Ash and Electric Impedance Analysis

2.1 Humidity Sensors

Humidity sensors are a type of chemical sensor, that is, a device capable of providing information about the chemical composition of a system through interaction with one of its constituent species [13]. A chemical sensor typically consists of three main components: the sensing material, the transducer, and the analyzer [14]. The sensing process begins with the interaction between the sensing material and the analyte, which is the target substance under analysis. This interaction is then converted into a readable signal through a process known as transduction, in which a change in a physical property of the sensing material generates a measurable response, such as an electrical, optical, or mechanical signal. Finally, the signal is analyzed and interpreted to identify a chemical property of the analyte [15]. Figure 3 illustrates this process through a biological example: in the olfactory system of a dog, the analyte interacts with receptors in the nasal epithelium, is transduced into an electrical signal by the nervous system, and is then analyzed by the brain [16].

In chemical sensors, the interaction with the analyte is most commonly transduced into an electrical signal through changes in the electrical properties of the sensing material. Depending on the property being measured, the sensors can be classified as resistive, capacitive, or impedimetric [14]. Capacitive sensors operate based on variations in capacitance, which may result from changes in the geometry of the device or in the dielectric constant of the sensing



Figure 3 – Schematic representation of an olfactory system of a dog illustrating the components and stages of the chemical sensing process.

material. In contrast, resistive and impedimetric sensors rely on changes in the material's ability to oppose electrical current in direct and alternating current regimes, respectively [13, 14].

Humidity sensors, also known as hygrometers, have a long history, with early examples dating back to the 1500s, when Leonardo da Vinci described a device that registered weight changes in a ball of wool due to its hygroscopic nature (tendency to absorb moisture) [17]. In 1783, de Saussure developed the first hair hygrometer, which estimated atmospheric moisture by measuring the change in length of a human hair resulting from humidity absorption [17]. Modern humidity sensors are generally classified as either relative or absolute humidity sensors. For reasons that will be discussed in Section 2.1.1, the vast majority of commercially available sensors are of the relative humidity type, which will be the focus of this review [18].

In the 1980s, humidity sensors were broadly classified into three main categories: organic polymers, electrolytes, and porous ceramics [19]. Capacitive sensors based on electrolytes quickly fell out of favor, and by the 1990s, polymer and ceramic-based sensors became dominant, primarily due to their high surface area and porosity [20,21]. Today, sensor development is led by porous ceramic materials such as alumina and other metal oxides, including nanoparticles, nanowires, and nanorods, as well as polymer-based materials like cellulose and polyaniline, 2D materials such as graphene, and even electrolytes like lithium chloride [9,18,22]. A comparative analysis of these sensor types will be presented in Section 2.1.4.

2.1.1 Humidity

Humidity is defined as the amount of water vapor present in a gas mixture [23]. It can be expressed through different physical quantities, each with a distinct meaning. The most common are absolute humidity (AB) and relative humidity (RH), with RH being the most widely used in indoor air quality monitoring, research laboratories, and industrial applications due to the simplicity of its measurement [18].

Absolute humidity refers to the total mass of water vapor per unit volume of gas and is typically expressed in grams per cubic meter (g/m^3) [18]:

$$AB = \frac{m_w}{V},\tag{2.1}$$

where m_w is the total mass of water vapor and V is the volume of the gas. Absolute humidity is not commonly used in sensor applications because it does not account for the temperature of the gas mixture. Temperature directly affects human comfort, contributes to static electricity issues, and significantly influences the interaction between the analyte and the sensing material. Moreover, this dependency makes absolute humidity more complex to measure, since sensor readings are affected by temperature. It is therefore more practical to measure a parameter that inherently incorporates temperature effects [24].

Relative humidity is a more practical parameter and will therefore be used in this work. In addition to its simplicity, it accounts for the maximum amount of water vapor that a gas can hold at a given temperature before condensation occurs, a quantity known as saturation humidity (SH), which incorporates the effect of temperature. Saturation humidity is defined as the total mass of water vapor at the saturation limit (m_{ws}) per unit volume of gas (V) [18]:

$$SH = \frac{m_{ws}}{V}. (2.2)$$

The parameter m_{ws} is temperature-dependent, as a gas can hold a greater amount of water vapor at higher temperatures [25].

Relative humidity (RH) is expressed as a percentage and defined as the ratio between absolute humidity (AB) and saturation humidity (SH), as follows [18, 25–27]:

$$RH = \frac{AB}{SH} \times 100\% = \frac{m_w}{m_{ws}} \times 100\%.$$
 (2.3)

This means that relative humidity represents the ratio between the actual amount of water vapor in the gas and the maximum amount it can hold before condensation, which is temperaturedependent.

2.1.2 Humidity Interactions

In solid-state sensors, humidity detection occurs through the interaction of water vapor molecules with the surface of a solid material. This interaction induces changes in the electrical properties of the material, which are reflected in variations in resistance, capacitance, or electrolytic conduction, depending on the type of sensor used [18].

This type of gas and solid interaction occurs due to Van der Waals forces between the gas molecules and the surface, which may involve permanent or induced dipoles [28]. Gas molecules can either penetrate the solid, a process known as absorption, or remain attached to the surface, called adsorption. Absorption usually happens in highly porous materials with large internal surfaces and is generally irreversible. Therefore, adsorption is the main interaction relevant for chemical sensors. The adsorption capacity of a surface depends on factors such as temperature, pressure, morphology, and the nature of the materials, specifically how strongly they interact [29].

Adsorption can occur in two different ways: physical adsorption, or physisorption, and chemical adsorption, or chemisorption [30]. In physisorption, if the gas molecule loses enough energy, it approaches the surface and is attracted to a potential well with energies (heat of adsorption) on the order of the thermal energy at room temperature. The molecule can be easily desorbed from the surface by receiving energy from the lattice itself or from external sources [28,30]. Chemisorption, in contrast, involves the formation of bonding orbitals between the gas molecule and the solid, resulting in a much higher heat of adsorption, typically several electron volts [31]. This interaction is more difficult to reverse and is more selective because it requires a dangling bond that matches the gas species. Chemisorption is usually limited to a monolayer since, after all dangling bonds are occupied, additional molecules can only physisorb [28]. Figure 4 illustrates these two types of adsorption processes.

The interaction between a solid surface and water vapor molecules is a well-known process that involves both chemisorption and physisorption. Due to its amphoteric nature, meaning the ability to act as both an acid and a base, water molecules readily self-ionize or react when in contact with surfaces or other reactive species [18]. At low humidity levels, when the first water vapor molecules contact the surface, a solid material previously exposed to air will have its surface populated with adsorbed oxygen species. These oxygen species react with the vapor

2.1. Humidity Sensors

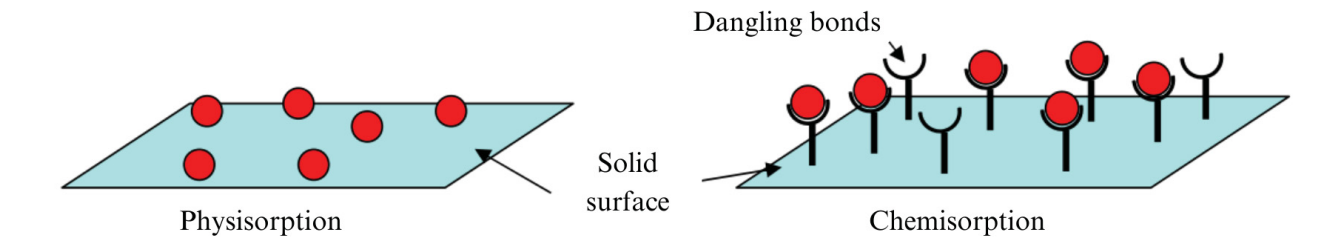


Figure 4 – Representation of physisorption and chemisorption of a gas on a solid surface.

Adapted from [31].

and desorb from the surface through reactions such as the following [11]:

$$2H_2O + O_2^- \Rightarrow 2H_2O_2 + e^-.$$
 (2.4)

These oxygen species had previously trapped free electrons on the material's surface to remain adsorbed. As they desorb, the electrons are freed to participate in conduction processes, as described in equation (2.4), thereby altering the material's electrical behavior [11].

As the concentration of water vapor in the gas increases, the molecules begin to interact with the surface and undergo self-ionization [18]:

$$H_2O \Rightarrow OH^- + H^+. \tag{2.5}$$

If available, hydroxide ions (OH^-) remain chemisorbed at matching sites on the surface, while hydrogen nuclei (H^+) protonate other molecules, forming hydronium ions (H_3O^+) . At this stage, protons can also migrate between hydroxide sites, contributing to electrical conduction [18]. As humidity further increases, hydrogen bonding between adjacent hydroxides leads to the formation of a water multilayer, where additional water vapor molecules physisorb and proton conduction is enhanced [11, 18, 32]. This proton conduction occurs via the Grotthuss chain reaction, or Grotthuss mechanism, first described by Theodor von Grotthuss in 1806 [33]:

$$H_3O^+ + H_2O \Rightarrow H_2O + H_3O^+.$$
 (2.6)

In this mechanism, protons move between adsorbed water molecules via hydrogen bonds with high mobility [34]. These processes are illustrated in Figure 5.

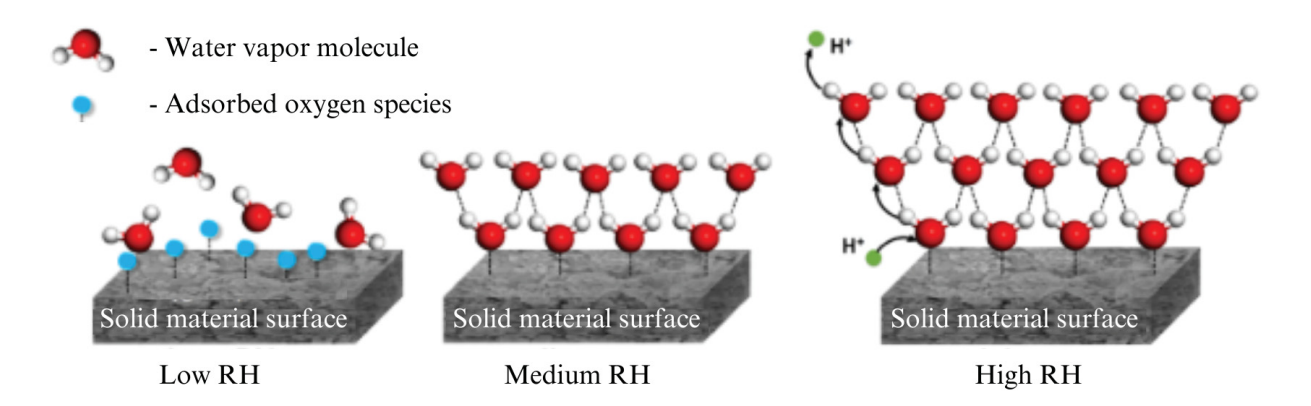


Figure 5 – Humidity interaction mechanisms. Adapted from [11].

2.1.3 Characterization Parameters

To characterize the operation of a sensor, a property of the sensing material must be monitored over time as the sensor is exposed to the analyte. This measurement produces a time series known as the response curve, from which key characterization parameters can be derived. The main parameters include sensitivity, response and recovery times, and the limit of detection (LoD) [13]. These parameters are described in the following sections.

2.1.3.1 Sensitivity

Sensitivity is a key parameter not only for characterizing a sensor but also for calibrating it, as it indicates how the sensor responds to changes in analyte concentration [13,27].

To analyze the sensor's response, it is important to consider the baseline value of the measured property when the sensor is not exposed to the analyte, known as the blank (R_0) . To facilitate this, the relative response (RR) is defined as follows [35]:

$$RR = \frac{|R - R_0|}{R_0},\tag{2.7}$$

Here, R is the response at a given analyte concentration, R_0 is the blank value, and RR is the relative response. The relative response indicates how much the property value changes at that concentration relative to the blank. In some cases, it is useful to express the relative response as a percentage by multiplying the definition in equation (2.7) by 100%. When the sensor response causes a decrease in the property value, it is helpful to redefine the relative response to avoid values constrained below 100%:

$$RR = \frac{|R - R_0|}{R}. ag{2.8}$$

To obtain the sensitivity, a calibration curve must be constructed. This curve represents the change in relative response as a function of analyte concentration (C). The slope of the calibration curve corresponds to the sensitivity (S), which quantifies the rate of change of the response with respect to concentration [27,35]:

$$S = \frac{\partial(RR)}{\partial(C)}. (2.9)$$

Figure 6 shows an illustrative example of a time series representing the response of a sensing material property that decreases when exposed to a certain analyte concentration, along with a calibration curve constructed from multiple such response curves at different concentrations.

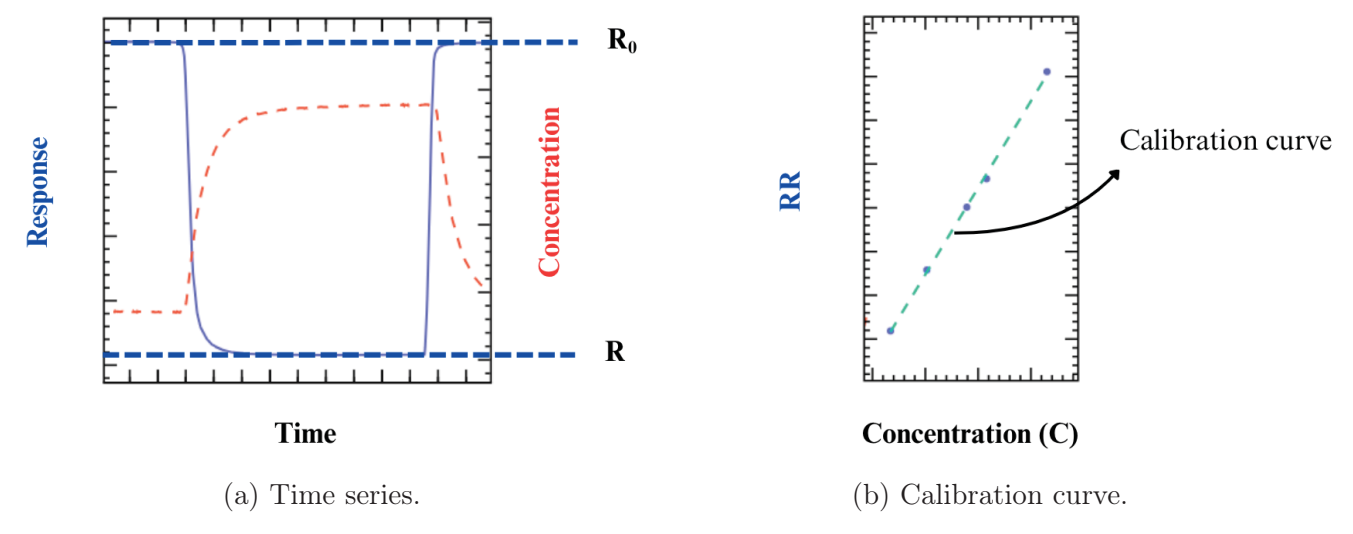


Figure 6 – Illustrative example of (a) time series (response curve) and (b) calibration curve for a sensor.

2.1.3.2 Response And Recovery Times

The response and recovery times are parameters that indicate how quickly the sensor reacts to the presence of the analyte and, once the analyte is removed, how quickly it returns to the baseline value [27].

From Figure 6(a), it can be observed that the response curve begins at the blank value (R_0) , increases toward a saturation value (R) after exposure to a set concentration of analyte, and then returns to the blank once the analyte is removed. This behavior occurs because, depending

on the interaction mechanism, the property of the sensing material tends to reach a stable response after a certain period of exposure. The transition to saturation typically follows an S-shaped curve. Initially, the property changes rapidly, and then gradually approaches the saturation value.

Due to this behavior, it is conventionally accepted that the sensor has fully responded once 90% of the total change from the blank to the saturation value is reached. Likewise, the recovery is considered complete when the response returns to within 10% of the same interval [35]. This convention is illustrated in Figure 7.

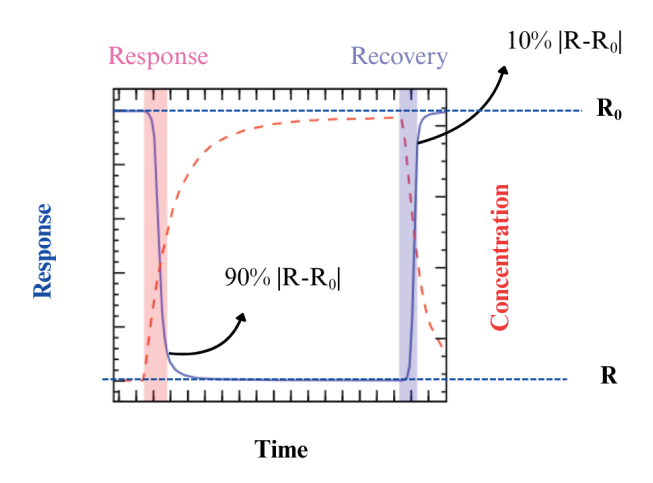


Figure 7 – Representation of the response and recovery times in the response curve.

2.1.3.3 Limit Of Detection (LoD)

The last parameter is the limit of detection (LoD), which represents the lowest concentration at which the sensor's response can be statistically distinguished from measurement noise [13,27]. To determine the LoD, it is necessary to evaluate the signal-to-noise ratio, defined as the ratio between the response value and the standard deviation of the blank [36]. The LoD is conventionally defined as the concentration at which the response (R_{LoD}) exceeds the mean of the blank (R_0) by more than three times the standard deviation (σ) , ensuring the signal rises above the noise level with 99.7% confidence. This criterion is illustrated in Figure 8 [27,36].

The LoD is determined by identifying the concentration at which the sensor exhibits a response equal to R_{LoD} . This is done by representing the relative response corresponding to the LoD, as defined in equation (2.8), as a horizontal line on the calibration curve in Figure 6 (b), and locating its intersection with the calibration curve.

2.1. Humidity Sensors 27

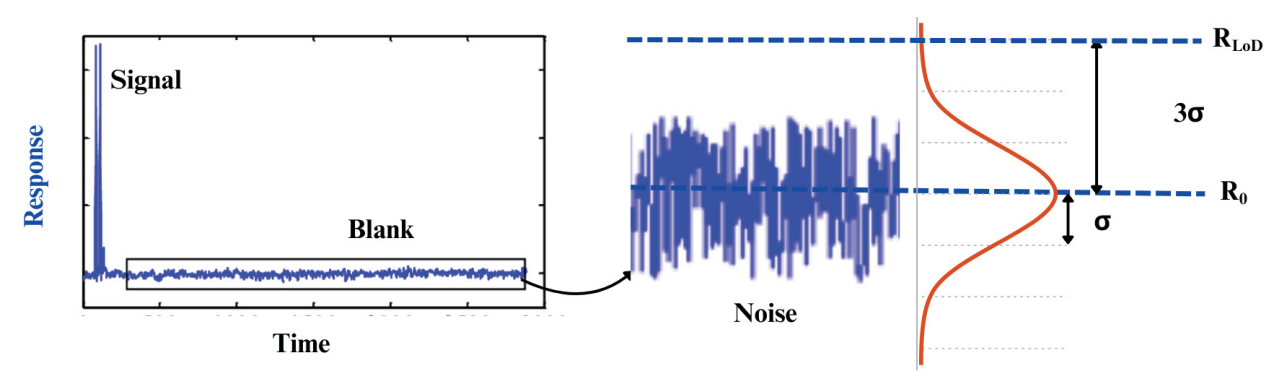


Figure 8 – Representation of the relation between signal and noise and the response of the limit of detection (R_{LoD}) . Adapted from [36].

2.1.4 State Of The Art

As previously stated, humidity sensors can be based on various types of signals. Since this work focuses on devices that use electrical signals, Table 1 presents a compilation of sensors from the literature, grouped by the type of electrical signal analyzed. A wide range of materials is currently being explored, with emphasis on porous ceramics, polymers, carbon-based materials, and composites [26,32]. Among the different types of electrical signals, resistive devices are the most common due to their simple implementation. Capacitive devices are preferred for very low relative humidity measurements because of the large variations in the dielectric constant in that regime [9].

In terms of sensitivity, comparing results across studies is challenging due to differences in sensing mechanisms, which lead to varying calibration curves. For this reason, sensitivity is better interpreted as a calibration parameter rather than a direct indicator of performance.

It is also important to note that, although less common, biomass-based devices are being studied as potential substitutes for more expensive conventional materials [10]. This approach also motivates the present work.

Table 1 – Humidity sensors in the literature. Materials marked with (*) are biomass-based devices.

Material	Signal	Sensitivity	RH Limits	m Resp./Rec.	Ref.
PEEK-co- PEG/LiCl	Impedimetric	$0.062~\rm logZ/\%RH$	11-97%	$3~/~52~\mathrm{s}$	[37]
CuO	Impedimetric	22611%	13-97%	32 / - s	[38]
GO	Impedimetric	1117,3	11-93%	5 / 11 s	[39]
CNF/CB	Resistive	120%	30-90%	10 / 6 s	[40]
FG	Resistive	$0{,}22\%$ / $\%\mathrm{RH}$	20-80%	$82\ /\ 125\ \mathrm{s}$	[41]
Paper*	Resistive	1647	41- $91%$	$472\ /\ 19\ \mathrm{s}$	[42]
Paper ash*	Resistive	10^{6}	15-90%	2 / 10 s	[11]
Potato peel*	Resistive	$70k\Omega$ /%RH	45-80%	0,96 / 1,65 s	[10]
Rice husk ash*	Resistive	_	0-93%	$20~/~23~\mathrm{s}$	[43]
Al_2O_3	Capacitive	0,53	1-10%	$10~/~16~\mathrm{s}$	[44]
PVA	Capacitive	$0.324~\mathrm{pF}/\%\mathrm{RH}$	0-20%	$70~/~120~\mathrm{s}$	[45]

2.2 Biomass ash

Biomass is defined as biodegradable material originating from living or recently living organisms. It can be sourced from animals, plants, and microorganisms, and includes materials such as agricultural residues, forestry products, and municipal waste. Biomass is widely applied as a renewable and environmentally friendly energy source [46,47]. Plant-based biomass is among the most commonly used, with applications in heating and soil fertilization [48,49]. The residue and waste generated from biomass, in the form of ash, can be reused for various purposes. These include correcting soil acidity in agriculture [50,51], neutralizing mine drainage [52], producing cement for construction [53], and, as explored in this work, serving as a material for chemical and electrochemical sensors [11,54].

The chemical composition of biomass ash varies depending on its source. However, plant-based biomass ash is known to contain elements such as calcium, potassium, silicon, and sodium [55–57]. The molecular organization depends on whether the combustion was complete or incomplete. For example, functional groups such as CO₃ decompose at high temperatures,

2.2. Biomass ash 29

so some ashes may contain carbonates and bicarbonates, while others resulting from complete combustion may consist primarily of simpler oxides [11,58].

High porosity, large surface area, and the presence of functional groups on the surface are key characteristics that make biomass ash a promising material for chemical sensors. These properties enable high sensitivity to humidity, which is the focus of this study [11, 43]. The biomass ash used in this work is derived from Acácia Negra and Timbó trees, which are commonly used as renewable energy sources through direct combustion for heat generation [59]. This process produces a significant amount of ash as a byproduct, which is often treated as waste. However, as discussed in this section, this ash can be repurposed as a functional material for chemical sensing. The general characteristics of these two tree species are presented in the following sections. Additionally, the techniques employed to investigate the physical and chemical characteristics of the ash, including its composition and morphology, are described and discussed in subsequent sections.

2.2.1 Acácia Negra

Acacia mearnsii De Wild., known in Brazil as Acácia Negra (black wattle), is a tree native to southwestern Australia that was introduced to Brazil in the 1930s for commercial planting in the state of Rio Grande do Sul [60]. It is considered a large shrub or a small tree, typically reaching heights between 6 and 10 meters, and up to 15 meters in exceptional cases. Mature plants have a main stem that is usually straight, with hard, fissured bark and a characteristic blackish-brown color [61].

In Brazil, it is cultivated to improve soil quality for agriculture, to provide shade and support for cattle grazing in the undergrowth, and its wood is used in various applications, including the production of wine barrels and vegetable charcoal [59,62]. Figure 9 shows the species being cultivated for commercial use in Brazil (a), and a mature specimen in the Australian National Botanic Gardens (b).





(a) Cultivation of Acácia Negra. Source: [62]

(b) Adult sized Acácia Negra. Source: [63]

Figure 9 – Acácia Negra cultivation in Rio Grande do Sul, Brazil (a) and an adult-sized Acácia Negra in Australia (b).

2.2.2 Timbó

Ateleia glazioveana, known in the southern states of Brazil as Timbó, is a tree ranging from 5 to 15 meters in height and reaching up to 25 meters in some cases. It typically presents a main straight stem around 8 meters tall, with smooth, light-gray bark [64]. This species is native to Brazil and naturally occurs in the states of Paraná, Rio de Janeiro, Rio Grande do Sul, Santa Catarina, and São Paulo.

Timbó is known for its medicinal properties, being used as a tea to treat appendicitis, and it also exhibits insecticidal effects [65]. Its leaves serve as cattle fodder during drought periods, however, ingestion in large quantities is toxic and can cause symptoms such as abortion in bovines [66]. Figure 10 shows an adult specimen (a) and a close-up of its characteristic bark (b).

2.2.3 Structural Characterization Techniques

To understand the sensing behavior of the materials used in this study, it is essential to investigate their structural and compositional properties. This section presents the characterization techniques employed to analyze the physical, chemical, and morphological features of the ash derived from *Acácia Negra* and *Timbó*. These techniques provide insights into elemental composition, morphology, and surface characteristics, all of which influence the sensor's performance. The selected methods include scanning electron microscopy (SEM) and energy-dispersive X-ray

2.2. Biomass ash 31







(b) Timbó's bark. Source: [66]

Figure 10 – Photos of (a) an adult-sized Timbó and (b) the typical bark of the tree.

spectroscopy (EDS) for morphological and elemental analysis, Fourier-transform infrared spectroscopy (FTIR) for the detection of functional groups, and X-ray photoelectron spectroscopy (XPS) to identify elemental composition and chemical states. Each technique is described in detail in the following subsections.

2.2.3.1 Scanning Electron Microscopy (SEM) and Energy-dispersive X-ray Spectroscopy (EDS)

Scanning Electron Microscopy (SEM) is a widely used technique in materials science and physics for investigating the surface morphology and microstructure of materials. SEM operates by focusing a high-energy electron beam onto the surface of a sample, generating various signals through electron matter interactions. Among these, secondary electrons (SE), which are emitted from the top few nanometers of the sample, can provide high-resolution images of the surface topology with nanometer-scale resolution. The imaging is conducted under vacuum, and the sample must be electrically conductive or coated with a thin conductive layer (like gold or carbon) to prevent charge accumulation [67,68].

SEM systems are frequently equipped with Energy Dispersive X-ray Spectroscopy (EDS), which enables localized elemental analysis by detecting characteristic X-rays emitted from the sample during electron bombardment [69]. This combination allows simultaneous morphological and compositional characterization.

2.2.3.2 X-ray Photoelectron Spectroscopy (XPS)

X-ray Photoelectron Spectroscopy (XPS) is a surface-sensitive analytical technique used to determine the elemental composition, chemical state, and electronic environment of atoms within the top few nanometers of a material's surface. XPS works based on the photoelectric effect: a material is irradiated with monochromatic X-rays, causing core-level electrons to be ejected from atoms in the sample. The kinetic energy of these photoelectrons is measured, and their binding energy is calculated, which is characteristic of each element and its chemical state [70]. XPS can detect all elements with atomic number greater than 3 (excluding hydrogen and helium) and provides both qualitative and quantitative surface composition data. Lighter elements such as hydrogen and helium are not detectable because they lack core electrons with sufficient binding energy and have extremely low photoionization cross-sections, making their emitted photoelectrons undetectable or indistinguishable from background noise [71].

The interpretation of XPS spectra involves analyzing peak positions (to identify elements) and chemical shifts (to determine bonding environments). XPS is especially useful in examining coatings, and thin films, where surface chemistry is critical to material performance, such as in sensors [72, 73].

2.2.3.3 Fourier Transform Infrared Spectroscopy (FTIR)

Fourier-Transform Infrared Spectroscopy (FTIR) is a non-destructive analytical technique used to identify molecular structures and functional groups by measuring how a material absorbs infrared light at different wavelengths. It works on the principle that different chemical bonds vibrate at characteristic frequencies when exposed to IR radiation [74]. FTIR measurements can be performed using attenuated total reflectance (ATR) or in absorbance mode depending on the sample type and preparation. In FTIR, a broad-spectrum IR beam is passed through a sample, and the resulting absorption spectrum is produced using a mathematical Fourier transform. The position and intensity of the absorption bands reveal the presence of specific functional groups and provide insight into the chemical composition of organic and inorganic materials [75].

FTIR is widely used for qualitative and quantitative analysis of polymers, pharmaceuticals, minerals, thin films, and biological tissues [76]. Data interpretation involves matching absorption

peaks to known vibrational frequencies of functional groups, and the presence or change of these peaks can indicate molecular interactions, degradation, or phase transitions [77].

2.3 Electric Impedance Analysis

2.3.1 Electric Impedance

To monitor the electrical behavior of the sensor, a voltage is applied and the resulting current is measured, or vice versa. This technique can be performed using either direct current (DC) or alternating current (AC), depending on the objectives of the experiment [78]. Both DC and AC measurements enable sensor characterization. However, in this work, AC measurement is employed because it provides additional information about the solid–gas interactions involved in the device's operation and the underlying charge transport phenomena.

Since AC measurements can be performed across a range of frequencies, they allow the distinction of different physical processes based on their characteristic time scales, as will be discussed in section 2.3.2 [79]. Furthermore, DC measurements often require higher voltages than AC, which may lead to device degradation due to energy dissipation caused by high current levels [80].

DC measurements are simpler in nature, as the ratio between the applied voltage and the resulting current directly yields the resistance of the device. In AC measurements, the analysis involves the relationship between two signals: the input and the output. If this relationship is linear and does not vary with time, it can be described by a transfer function that characterizes how the material interacts with the applied signal. When the input and output signals are voltage and current, respectively, the transfer function is referred to as the electrical impedance [81,82].

The mathematical foundation for analyzing electrical impedance was established by Heaviside in the late nineteenth century [83]. This laid the groundwork for the rapid development of impedance techniques in electrochemical systems, with significant contributions by researchers such as Warburg [84], Cole and Cole [85], and the introduction of equivalent circuit representations by Randles [86]. Since then, impedance analysis has seen growing application in the study of chemical reactions, materials characterization, and, more recently, in sensor development [87,88].

Consider now a sinusoidal voltage (V) of frequency f and the corresponding current (I), defined as:

$$V(t) = V_0 \sin(\omega t), \tag{2.10}$$

$$I(t) = I_0 sin(\omega t + \phi), \qquad (2.11)$$

where ω is the angular frequency ($\omega = 2\pi f$), V_0 and I_0 are the amplitudes of the signals, and ϕ is the phase shift of the current relative to the voltage. In this case, the applied signal and the response differ in amplitude and phase, but the relationship between them is time-independent, since both share the same angular frequency (ω). This allows for the construction of a transfer function to describe the device's response.

Operationally, when a measurement device such as a potentiostat performs this experiment, it records a time series of points for each frequency, for both voltage and current signals. To analyze the relationship between them, the instrument applies a discrete Fourier transform (DFT) to convert the time-domain data into phasors in the frequency domain. These phasors represent the amplitude and phase of each signal at a given frequency, as illustrated in Figure 11. The ratio between the voltage and current phasors yields the impedance (Z) [87]. Theoretically, this relationship can be expressed as follows [87,89]:

$$Z(\omega) = \frac{\mathcal{F}[V(t)]}{\mathcal{F}[I(t)]},\tag{2.12}$$

where $\mathcal{F}[f(t)]$ denotes the Fourier transform of the function f(t). Using the definition of impedance from equation (2.12), along with the expressions for voltage and current given in equations (2.10) and (2.11):

$$Z(\omega) = \frac{\mathcal{F}[V_0 sin(\omega t)]}{\mathcal{F}[I_0 sin(\omega t + \phi)]} = \frac{V_0 \mathcal{F}[sin(\omega t)]}{I_0 e^{-i\phi} \mathcal{F}[sin(\omega t)]} = \frac{V_0}{I_0} e^{i\phi}, \tag{2.13}$$

where i is the imaginary unit and the property of Fourier's transform with phase addition: $\mathcal{F}[f(t+t_0)] = e^{-iwt_0}\mathcal{F}[f(t)]$ was used. Being the ratio of two phasors, it can be seen from equation (2.13) that the impedance (Z) is a phasor itself, and thus, can be expressed as a complex number in two ways [90]:

$$Z(\omega) = |Z|e^{i\phi}, \tag{2.14}$$

or

$$Z(\omega) = Re(Z) + iIm(Z) = |Z|cos(\phi) + i|Z|sin(\phi), \tag{2.15}$$

where $|Z| = V_0/I_0$, ϕ , Re(Z) and Im(Z) represent the modulus, the phase, the real part and the imaginary part of the impedance, respectively. From equation (2.14), it can be seen that the modulus of the impedance, and thus the real and imaginary parts, have units of volts per ampere, which is ohm [91].

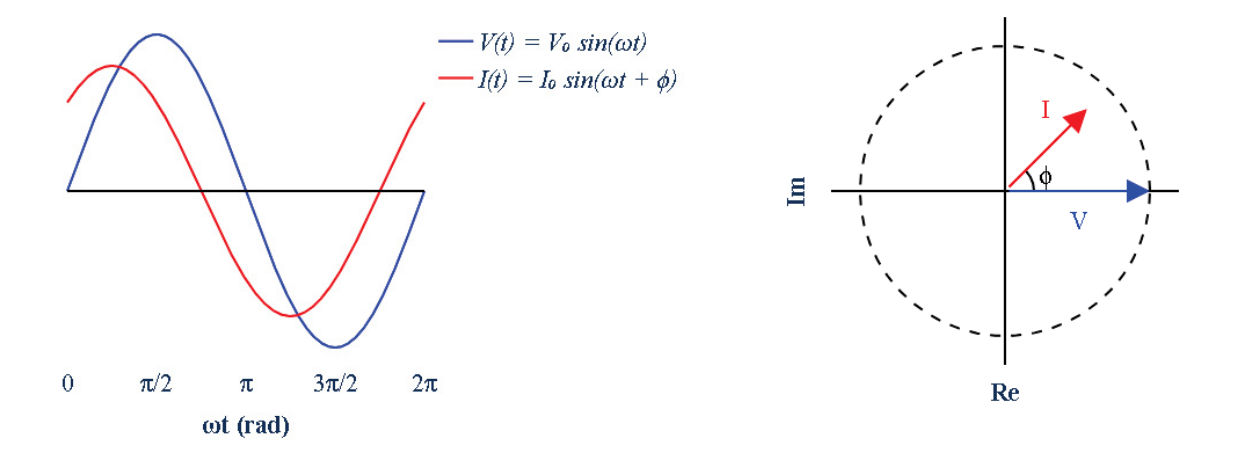


Figure 11 – Signals and their representation as phasors in the complex plane. To produce the waves, the phasors rotate counterclockwise with angular frequency ω and the current phasor is ϕ radians ahead of the voltage.

2.3.2 Electric Impedance of Basic Elements and Circuits

As stated in the electric impedance section (2.3.1), equivalent circuits composed of basic elements can be used to represent physical systems, such as those investigated in this work. Therefore, it is important to understand how the fundamental circuit components, namely resistors, capacitors, and inductors, behave in relation to electrical impedance.

Using equation (2.12), it is possible to compute the impedance for ideal components. In this study, impedance analysis is applied to monitor the electrical behavior of a sensor in the presence of an analyte. In this context, only resistive and capacitive behaviors are expected to appear,

and thus, only these two components will be discussed. Inductive effects can be neglected, since they usually arise in systems with significant current flow and closed-loop geometries, which are not present in the sensor configuration used in this work.

Considering the relationship between current (I) and voltage (V) in a resistor, as defined by Ohm's law, the impedance (Z_R) of a resistor with resistance R is given by [82]:

$$V = RI, (2.16)$$

$$Z_R(\omega) = \frac{\mathcal{F}(RI)}{\mathcal{F}(I)} = R.$$
 (2.17)

from which it can be seen that the impedance of an ideal resistor has only a real part, with a constant magnitude R and a constant phase of 0. This means that, in this case, the current is in phase with the voltage.

Considering now a capacitor with capacitance C, the impedance Z_C is given by [82]:

$$Q = CV, (2.18)$$

$$I = \frac{dQ}{dt} = C\frac{dV}{dt},\tag{2.19}$$

$$Z_C(\omega) = \frac{\mathcal{F}(V)}{\mathcal{F}(C\frac{dV}{dt})} = \frac{\mathcal{F}(V)}{C\mathcal{F}(\frac{dV}{dt})} = \frac{1}{i\omega C} = -\frac{1}{\omega C}i,$$
(2.20)

where the property of Fourier transforms $\mathcal{F}\left[\frac{df(t)}{dt}\right] = i\omega \mathcal{F}[f(t)]$ was used. For the capacitor, the impedance has only an imaginary part, with magnitude $1/(\omega C)$ and a constant phase of -90 degrees. This indicates that the current leads the voltage by 90 degrees, and the amplitude of the response decreases with increasing frequency.

Since a real system will exhibit both capacitive and resistive behavior, it is important to consider the two basic configurations of these components: a resistor and a capacitor in series (R-C) and in parallel (R,C). For the series configuration, the equivalent impedance Z_{R-C} can be computed using Kirchhoff's relations [81]:

$$Z = Z_R + Z_C, (2.21)$$

$$Z_{R-C} = R - \frac{1}{\omega C}i. \tag{2.22}$$

For the parallel association, the equivalent impedance $Z_{(R,C)}$ will be [81]:

$$\frac{1}{Z_{(R,C)}} = \frac{1}{Z_R} + \frac{1}{Z_C},\tag{2.23}$$

$$\frac{1}{Z_{(R,C)}} = \frac{1}{R} + i\omega C = \frac{i\omega RC + 1}{R}.$$
 (2.24)

$$Z_{(R,C)} = \frac{R}{i\omega RC + 1} = \frac{R - i\omega R^2 C}{1 + \omega RC} = \frac{R}{1 + \omega RC} - \frac{\omega R^2 C}{1 + \omega RC}i$$
(2.25)

First of all, it can be seen from equations (2.20), (2.22) and (2.25) that the imaginary part of the impedance for both circuits is negative because it originates from the capacitor, which has a negative imaginary impedance. Therefore, it is common to work with $-\operatorname{Im}(Z)$, so the phase of the impedance is represented as the angle whose tangent is given by $-\operatorname{Im}(Z)/\operatorname{Re}(Z)$, resulting in a positive value. Figure 12 shows the phase and magnitude of the impedance plotted against frequency on a logarithmic scale for both configurations. Such graphs of a parameter versus the logarithm of frequency are known as Bode plots [87].

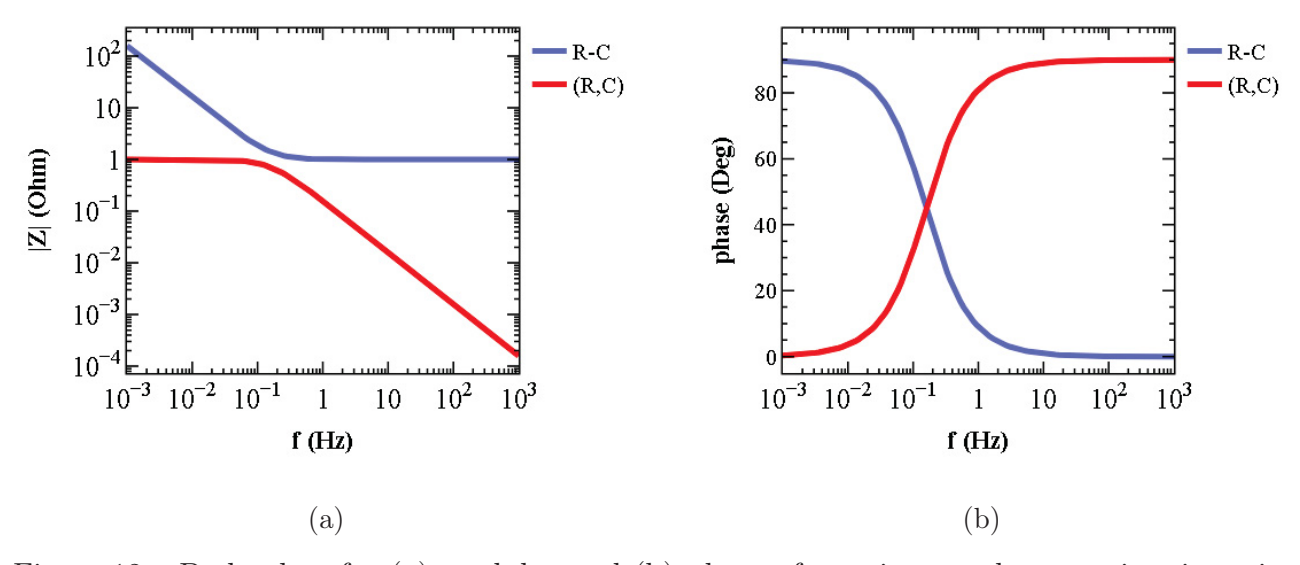


Figure 12 – Bode plots for (a) modulus and (b) phase of a resistor and a capacitor in series, R-C, and in parallel, (R,C). In this simulation, R=1 Ohm and C=1 F.

Since the Bode plot for the modulus is usually represented in log-log form, a straight line indicates a power-law relationship, with the slope corresponding to the exponent. In Figure 12

(a), the slope of the non-constant straight-line sections is -1, showing that the modulus is proportional to 1/f, as expected for a capacitor.

At low frequencies, the series R-C circuit is dominated by the capacitor, with the modulus following the 1/f trend and phase 90°, while the parallel (R,C) circuit is dominated by the resistor with the modulus equal to the resistance (1 Ω) and phase at 0°. At high frequencies, the resistor dominates the series configuration and the capacitor dominates the parallel one.

An alternative way to visualize these relationships is by plotting the imaginary part (or $-\operatorname{Im}(Z)$) versus the real part, for a range of frequencies. This plot, known as the Nyquist plot, is shown in Figure 13 [90].

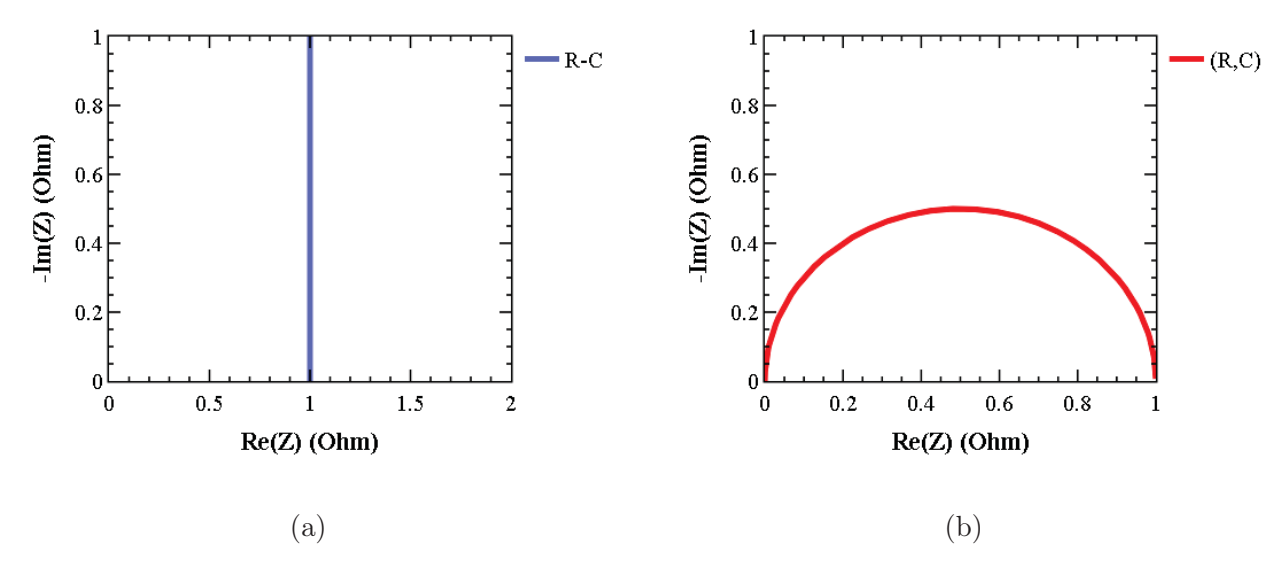


Figure 13 – Nyquist graphs for a resistor and a capacitor (a) in series, R-C, and (b) in parallel, (R,C). In this simulation, R=1 Ohm and C=1 F.

In the Nyquist plot for the series R-C circuit shown in Figure 13, there is a purely imaginary impedance corresponding to the capacitor, which is shifted along the real axis by exactly the value of the resistor. This illustrates that placing a resistor in series results in a horizontal displacement of the impedance by the resistor's value.

For the parallel (R,C) circuit, the Nyquist plot displays a semicircle, whose diameter equals the resistance of the resistor. This can be seen clearly by separating the real and imaginary parts of the impedance in equation (2.25) and rearranging the terms:

$$\operatorname{Re}(Z) = \frac{R}{1 + \omega^2 R^2 C^2}, \quad \operatorname{Im}(Z) = \frac{-\omega R^2 C}{1 + \omega^2 R^2 C^2}$$
 (2.26)

$$\frac{Im(Z)}{Re(Z)} = -\omega RC, \tag{2.27}$$

substituting (2.27) in the imaginary part from (2.26):

$$Im(Z) = \frac{R[\frac{Im(Z)}{Re(Z)}]}{1 + [\frac{Im(Z)}{Re(Z)}]^2},$$
 (2.28)

after some rearrangement:

$$Re(Z)^{2} - RRe(Z) + Im(Z)^{2} = 0.$$
 (2.29)

Adding $(R/2)^2$ to both sides to complete the square, the equation of a circle centered at (R/2, 0) with radius R/2 can be obtained:

$$\left(\text{Re}(Z) - \frac{R}{2}\right)^2 + \text{Im}(Z)^2 = \left(\frac{R}{2}\right)^2.$$
 (2.30)

In the Nyquist plot, it is common to show only the third quadrant but inverted to appear as the first quadrant by plotting -Im(Z) instead of Im(Z), as previously discussed [87]. It is important to note that, in this plot, the frequency decreases along the real axis from left to right.

For the parallel (R,C) circuit, at high frequencies near the origin, the impedance vector, drawn from the origin to a point on the curve, approximates that of a capacitor, which corresponds to a vertical line with a phase of 90°. At low frequencies, at the right end of the semicircle, the vector approaches that of a resistor, represented by a horizontal line with a phase of 0°, as previously explained.

The characteristic behavior of the (R,C) circuit occurs between these two extremes, specifically at the point on the semicircle that lies halfway between the high- and low-frequency limits along the curve. This point is the highest point on the semicircle, farthest from the real axis, and corresponds to the frequency where the phase angle is 45° ($\pi/4$ radians). This frequency can be found by evaluating the impedance at this phase angle:

$$\frac{\pi}{4} = tg^{-1}\left[\frac{-Im(Z)}{Re(Z)}\right] = tg^{-1}\left[\frac{\omega R^2 C}{R}\right] = tg^{-1}[\omega RC],\tag{2.31}$$

where the argument of the tg^{-1} function must be equal to 1,

$$\omega RC = 1. \tag{2.32}$$

Using $\omega = 2\pi f$ and f = 1/T, where T is the period of oscillation of the wave:

$$2\pi fRC = 2\pi \frac{RC}{T} = 1 \tag{2.33}$$

$$\frac{RC}{T} = \frac{1}{2\pi} = \frac{\tau}{T}.\tag{2.34}$$

The product $RC = \tau$ is known as the time constant, or the characteristic time of the circuit. In other words, equation (2.34) states that the period of the input signal must be close to the characteristic time of the circuit so that the full phenomenon can be observed. Equivalently, the frequency of the input signal must be such that its inverse is of the same order as the RC product, otherwise, the response will correspond to either a purely capacitive or purely resistive limit [81]. This means that selecting the frequency of the input signal enables obtaining information about different processes occurring in the circuit.

In real cases, ideal basic components often cannot fully model the behavior of the system. For these cases, non-ideal components such as the so-called constant phase element (CPE) are used [81]. The CPE models an element with behavior between that of an ideal resistor and an ideal capacitor and can be interpreted as a leaking capacitor, that is, a capacitor that allows charge leakage even when fully charged [87]. The impedance of the CPE (Z_{CPE}) is:

$$Z_{CPE} = \frac{1}{T(i\omega)^{\alpha}},\tag{2.35}$$

If $\alpha = 0$, the CPE behaves as a resistor, with 1/T = R, and if $\alpha = 1$, it behaves as a capacitor, with T = C. In general, α can take any value between 0 and 1, where values closer to 1 indicate a more capacitive behavior, and values closer to 0 indicate a more resistive behavior. This element is commonly used to model processes such as ionic adsorption or diffusion, especially in cases like pores filled with water molecules [92].

In this general case, the parameter T has units of $F \cdot s^{1-\alpha}$ or $\Omega^{-1} \cdot s^{\alpha}$ [81,87]. Figure 14 presents the Bode and Nyquist plots for circuits that use the CPE instead of an ideal capacitor.

The behavior at the limits remains similar to those previously discussed, with the CPE replacing the capacitor. However, it is important to highlight that the CPE produces a constant phase angle (which gives it its name) equal to $90^{\circ} \times \alpha$. This is evident from the slope of the curves in Figure 14 (a), the Bode plot for the CPE phase in Figure 14 (b), and the angle of the straight line in Figure 14 (c).

The slope of the CPE in the Bode plot for the modulus is $-\alpha$, as can be seen from equation (2.35). The Nyquist plot for the (R,CPE) circuit shows that when using the CPE instead of a capacitor, the semicircle-like curve becomes depressed at the top.

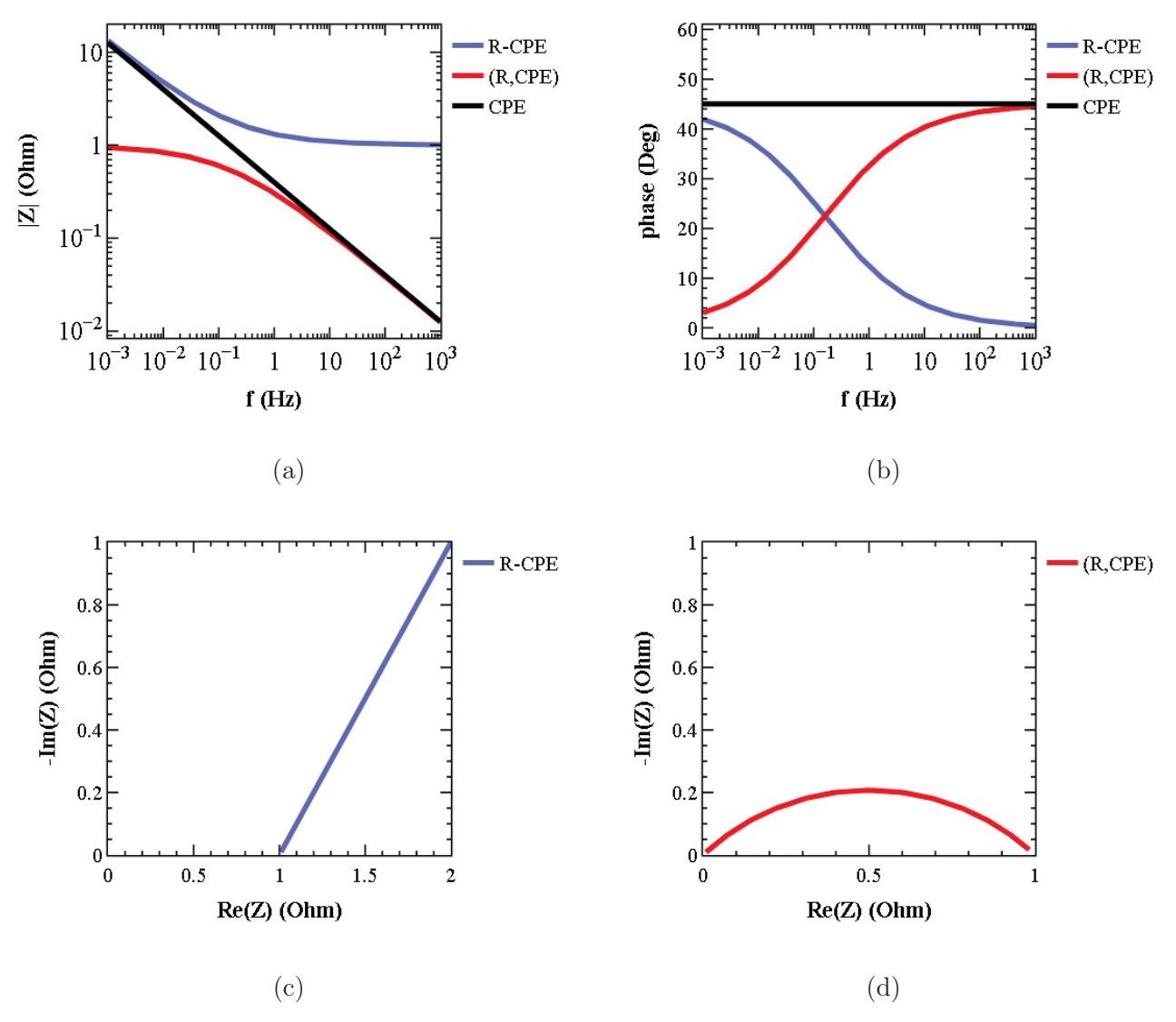


Figure 14 – Bode (a,b) and Nyquist (c,d) plots for circuits containing a CPE with $T = 1 F \cdot s^{1-\alpha}$ and $\alpha = 0.5$.

The phase behavior can be explicitly shown by rewriting equation (2.35) using the relation $i^{\alpha} = \cos\left(\frac{\alpha\pi}{2}\right) - i\sin\left(\frac{\alpha\pi}{2}\right)$ [87]:

$$Z_{CPE} = \frac{1}{T\omega^{\alpha}} \left[\cos \left(\frac{\alpha \pi}{2} \right) - i \sin \left(\frac{\alpha \pi}{2} \right) \right] = \frac{1}{T\omega^{\alpha}} e^{-i\alpha\pi/2}, \tag{2.36}$$

therefore, the phase angle equals $90^{\circ} \times \alpha$, as expected.

3

Impedimetric Humidity Sensors Based on Acácia Negra and Timbó Ash

3.1 Introduction

As shown in previous sections, there is a growing demand for relative humidity sensors for use in a wide range of applications. The objective of this chapter is to present how the ashes of Acácia Negra and Timbó have been employed to fabricate low-cost and eco-friendly devices capable of monitoring ambient relative humidity. Furthermore, it describes how the electrical impedance spectroscopy technique was used to investigate the electrochemical processes involved in the operation of these sensors.

3.2 Experimental

The devices used in this work follow the structure presented in Figure 15:

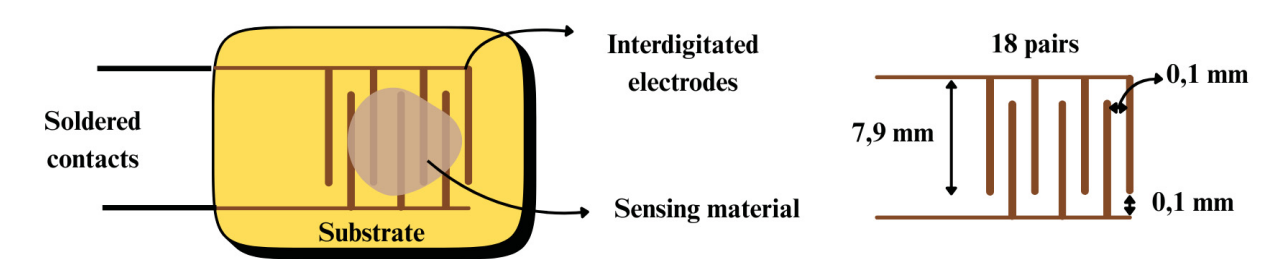


Figure 15 – Structure of the humidity sensor based on Acácia Negra and Timbó ash.

The substrate is made of FR4 (Fire Resistant 4), a material commonly used in the fabrication

of printed circuit boards. It consists of epoxy resin reinforced with fiberglass, offering the electrical insulation properties required for this application [93]. The interdigitated electrodes are composed of ENIG (*Electroless Nickel Immersion Gold*), a thin gold layer deposited over a nickel coating. This structure combines the excellent conductivity and oxidation resistance of gold with the lower cost of nickel [94]. The wires that connect the sample to the potentiostat are soldered onto the electrodes using commercial tin solder. The sensing material consists of a deposited layer obtained from dispersing Acácia Negra and Timbó ash in deionized water, as described later in this same section.

The wood ash was sourced from the Department of Forestry Technology Engineering at the Universidade Federal do Paraná (UFPR), and was produced in accordance with the D-1762–84 standard of the American Society for Testing and Materials (ASTM) [95]. According to this procedure, the biomass is initially placed in a crucible and subjected to calcination in a muffle furnace at 750 °C for 6 hours. After cooling, the sample is transferred to a desiccator for 1 hour and then weighed. This process is repeated in intervals of up to 1 hour to eliminate any remaining volatile compounds, until the mass loss between successive measurements is less than 0.0005 g [95].

Before deposition, the substrate undergoes a cleaning process using an ultrasonic bath for 20 minutes at 60 °C in three different solvents: acetone, deionized water, and isopropyl alcohol. After these three baths, the substrate is dried in a vacuum stove at 100 °C for 1 hour, and subsequently treated with ultraviolet radiation and ozone in a chamber for 20 minutes, as illustrated in Figure 16.

For the deposition onto the substrate, the ash powder must be dispersed in a solvent. Deionized water was selected as the dispersing medium due to its accessibility, non-toxic nature, and ease of handling. Additionally, water's relatively high viscosity, compared to solvents such as alcohols or toluene, aids in forming a more concentrated and uniform active layer within the designated area of the substrate.

Three different concentrations were tested: 5, 10, and 15 mg/mL, to evaluate layer consistency and sensor performance. Among these, the 10 mg/mL dispersion yielded more reproducible and functional sensors, and was therefore adopted for all subsequent experiments.

The resulting dispersion is subjected to ultrasonic agitation for 20 minutes at 60 °C to ensure

3.2. Experimental 45

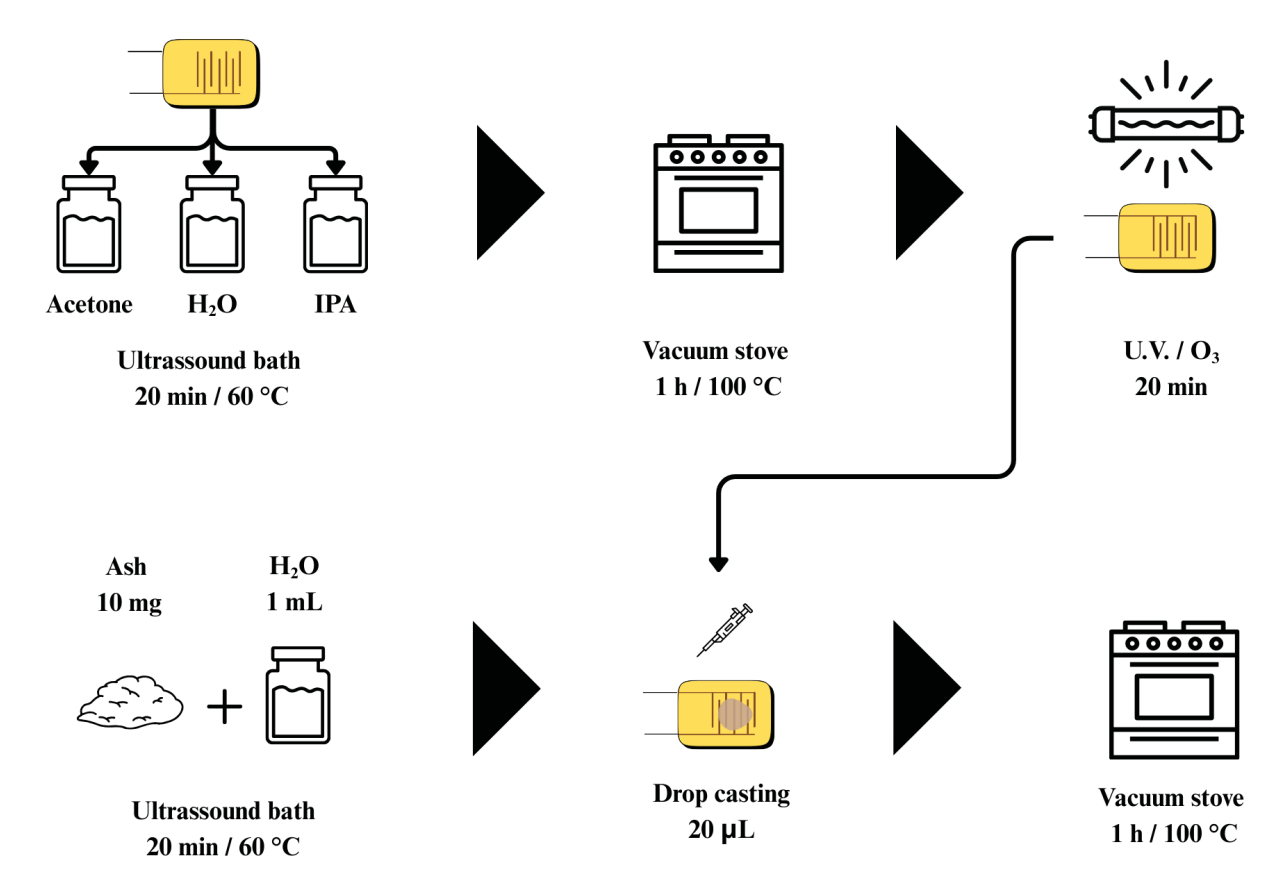


Figure 16 – Schematic representation of the deposition method. The substrate is first cleaned using ultrasonic baths in acetone, deionized water, and isopropyl alcohol at 60 °C for 20 minutes each, followed by drying in a vacuum stove and treatment with U.V./O₃. The sensing material is prepared by dispersing 10 mg of ash in 1 mL of deionized water using an ultrasonic bath, and 20 μ L of the resulting dispersion is deposited on the substrate by drop casting. Finally, the sample is dried again in a vacuum stove.

homogeneity. Then, $20 \,\mu\text{L}$ of the solution is deposited on the cleaned substrate using the drop casting method. The device is subsequently dried in a vacuum oven at $100\,^{\circ}\text{C}$ for 1 hour. While drop casting does not guarantee the formation of a uniform film, it remains the most viable technique in this case due to the low viscosity of the dispersion, which makes methods such as spin coating ineffective.

The analyte exposure tests are carried out in a sealed metallic chamber, where the gas flow is precisely controlled to achieve the desired concentrations. A schematic representation of the system is shown in Figure 17.

Following the schematic in Figure 17, gaseous nitrogen is generated by the machine (1) and used to establish an inert environment for the experiment. The gas first passes through a silica-based humidity filter (2) and then through a valve (3) that regulates the pressure at 3.5 bar. From this point, the flow is split into two branches, each controlled by an independent

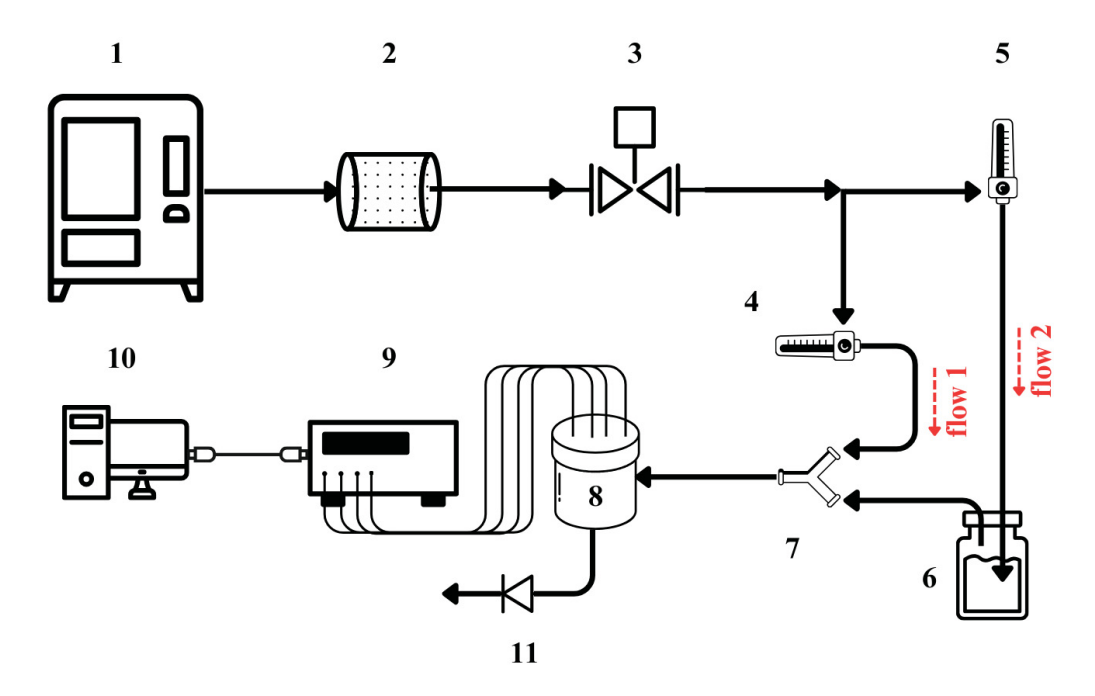


Figure 17 – Schematic representation of the gas flow system used for relative humidity control during sensor testing. (1) Nitrogen generator; (2) silica-based humidity filter; (3) pressure regulator; (4–5) flowmeters; (6) bubbler containing the analyte (water); (7) gas mixer; (8) sealed test chamber; (9) potentiostat for impedance measurements; (10) computer; (11) airlock with glycerin for maintaining constant flow and pressure. Flow 1 is the dry dilution stream, and flow 2 is the humidified stream. Relative humidity inside the chamber is controlled by adjusting these flows.

flowmeter (4 and 5): flow 1 goes directly to the mixer (7) and serves as the dilution stream, while flow 2 is directed into a bubbler (6) containing the analyte, in this case water, where it becomes saturated with moisture before joining the same mixer.

From the mixer, the resulting gas mixture is delivered to the chamber (8), where a commercial humidity sensor (SHTC3 [96]) monitors the relative humidity in real time. Inside the chamber, up to four sensor samples can be tested simultaneously using a potentiostat (9) connected to a computer (10). The excess gas exits the chamber through an airlock (11) filled with glycerin, which helps maintain constant pressure and flow.

This setup allows precise control of the relative humidity inside the chamber by adjusting the two flowmeters (4 and 5). For instance, increasing flow 2 while decreasing flow 1 raises the humidity, and the opposite adjustment lowers it.

The potentiostat used was a PalmSens MultiEmStat4 with four independent channels [97], which enables analysis with oscillating signals in the frequency range from 10 μ Hz to 200 kHz. Data acquisition was performed using the MultiTrace 4.5 software [98], provided by the same

manufacturer. Data processing was carried out in Python, primarily using the Pandas [99], NumPy [100], and Plotly [101] libraries. For the simulation of equivalent circuits, the impedance.py library was employed [102].

For structural characterization of the ashes, Scanning Electron Microscopy (SEM) and Energy-dispersive X-ray Spectroscopy (EDS) analyses were conducted on devices fabricated as described in this section, on the interdigitated substrate and on a pure silicon substrate. These analyses were performed at the Center for Electron Microscopy of the Universidade Federal do Paraná (CME-UFPR), using a TESCAN VEGA3 scanning electron microscope operating at 15 kV and equipped with an X-ray detection module.

Other characterization techniques were employed with the assistance of collaborators. Fourier Transform Infrared (FTIR) analysis was carried out in collaboration with laboratory technician Grazielli da Rocha, at the Multiuser Laboratory for Infrared Absorption Spectroscopy and XPS (LaMIV) of the Department of Chemistry at UFPR. Measurements in the mid infrared region were performed using a BRUKER Alpha II spectrometer in attenuated total reflectance (ATR) mode with a diamond crystal, covering the spectral range from 4000 to 400 cm⁻¹, with a resolution of 4 cm⁻¹ and 32 scans. Vibrational absorption spectra in the far infrared region were acquired using a BRUKER Vertex 70 spectrometer in absorbance mode, covering the spectral range from 400 to 200 cm⁻¹, with a resolution of 4 cm⁻¹ and 24 scans. The X-ray photoelectron spectroscopy (XPS) analyses were performed in collaboration with professors Guilherme Jean Pereira de Abreu and Richard Landers at the Gleb Wataghin Physics Institute (IFGW) at Unicamp, using AlK α radiation ($h\nu = 1486.6 \ eV$) from two different XPS chambers: a VSW HA-100 spherical analyzer instrument and a Thermo Scientific K-alpha model.

3.3 Results and Discussions

3.3.1 Structural Characterization

For the elemental characterization of the ashes, EDS analyses were performed on a silicon substrate, as described in Section 3.2. Figure 18 (a) presents the chemical composition of Acácia Negra ash, while Figure 18 (b) shows the composition of Timbó ash. Both materials are primarily composed of oxygen (O), calcium (Ca), carbon (C), and potassium (K), with smaller

amounts of other elements such as magnesium (Mg), phosphorus (P), and sodium (Na), among others. It is important to note that the silicon (Si) detected in this analysis may originate from the substrate itself, since the technique probes the exposed surface of the analyzed region, and the silicon substrate can be included in the measurement.

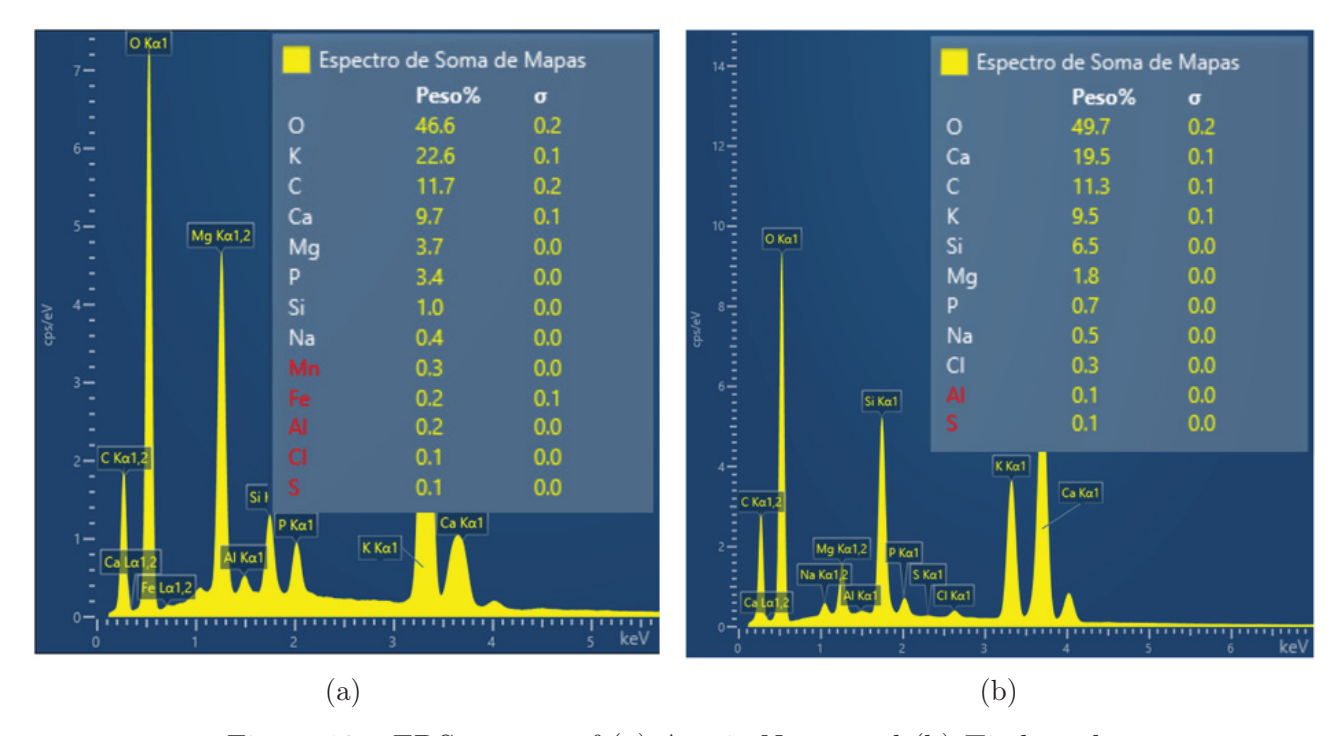


Figure 18 – EDS spectra of (a) Acácia Negra and (b) Timbó ash.

The XPS analyses corroborate the composition obtained by EDS, as shown in Figure 19, with prominent peaks corresponding to photoelectrons from O, Ca, C, and K. Both EDS and XPS results indicate that the composition of the two materials is very similar.

To investigate the molecular organization of these elements, FTIR analysis was carried out for both materials, as seen in Figures 20 (a) and (b). The absorption spectrum shows a predominance of functional groups typically associated with carbonates and bicarbonates (CO_3^{2-} / HCO_3^{-}) , with characteristic absorption bands in the wavenumber range between 1200 and 1500 cm⁻¹, likely related to Ca- and K-containing structures. Bands in the range of 550 to 1100 cm⁻¹ indicate the presence of silicates, aluminosilicates, or alumina (Si-O / O-Si-O / Al-O), along with confirmation of carbonates. In the higher wavenumber range, between 2000 and 3500 cm⁻¹, characteristic O-H stretching signals from acidic groups in minerals are observed. In the far-infrared region for Timbó ash (Figure 20 (c)), absorption bands typical of metal oxides such as Al-O, Fe-O, and Mn-O are detected.

Additional characterizations were carried out to study both the morphology and the compo-

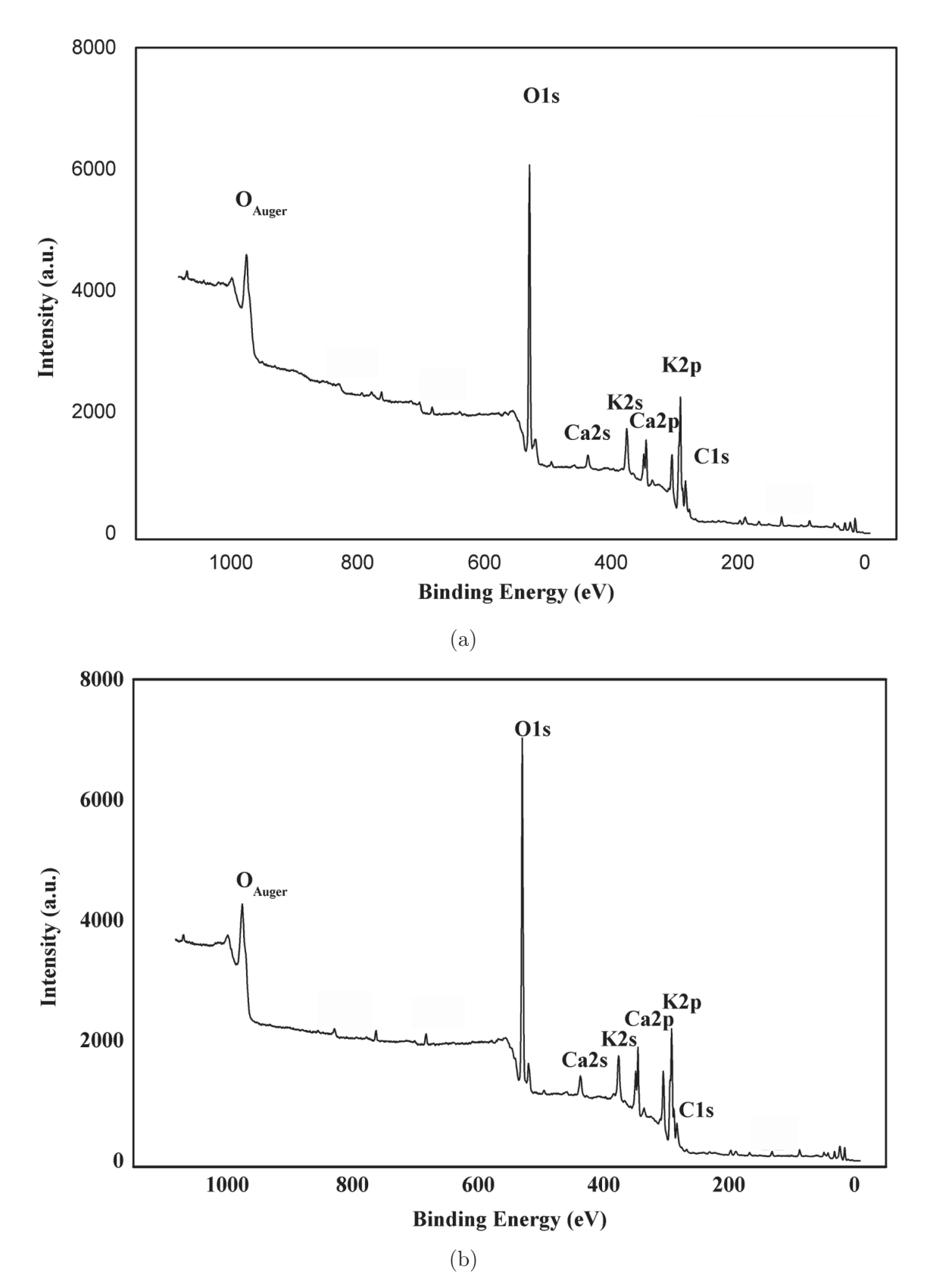


Figure 19 – XPS spectra of (a) Acácia Negra and (b) Timbó ash.

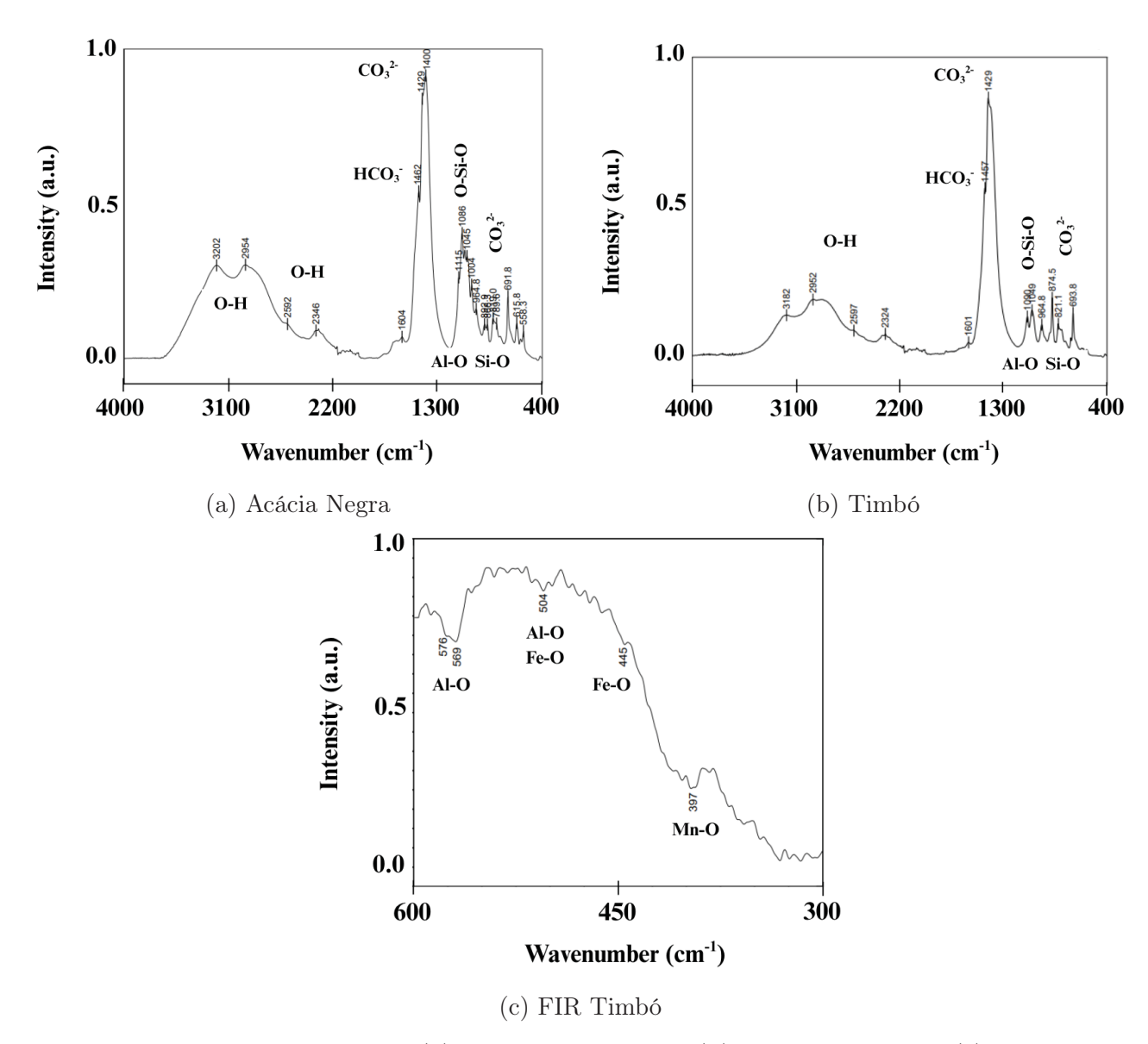


Figure 20 – FTIR spectrum for (a) Acácia Negra and (b) Timbó ash, and (c) far infrared spectrum of Timbó ash.

sition of the material on the sensor substrate. Figure 21 presents SEM images of the central region of Timbó ash deposition over the interdigitated FR4 substrate. In Figure 21(a), at 500×200 magnification, the interdigitated electrodes are visible, with ash deposited between and on top of them. The ash layer appears uniform in the central area, effectively covering the gaps between the electrode fingers.

At higher magnifications in Figures 21 (b), (c), (d), and (e), it becomes clear that the layer is not continuous but consists of a granular structure with interconnected regions. Figures 21 (d) and (e) highlight surface morphology, showing agglomerates of irregular particles with various sizes and rough surfaces that contribute to high surface area. Figure 21 (f) reveals well-defined,

plate-like crystalline features, indicating the presence of structured mineral phases within the ash.

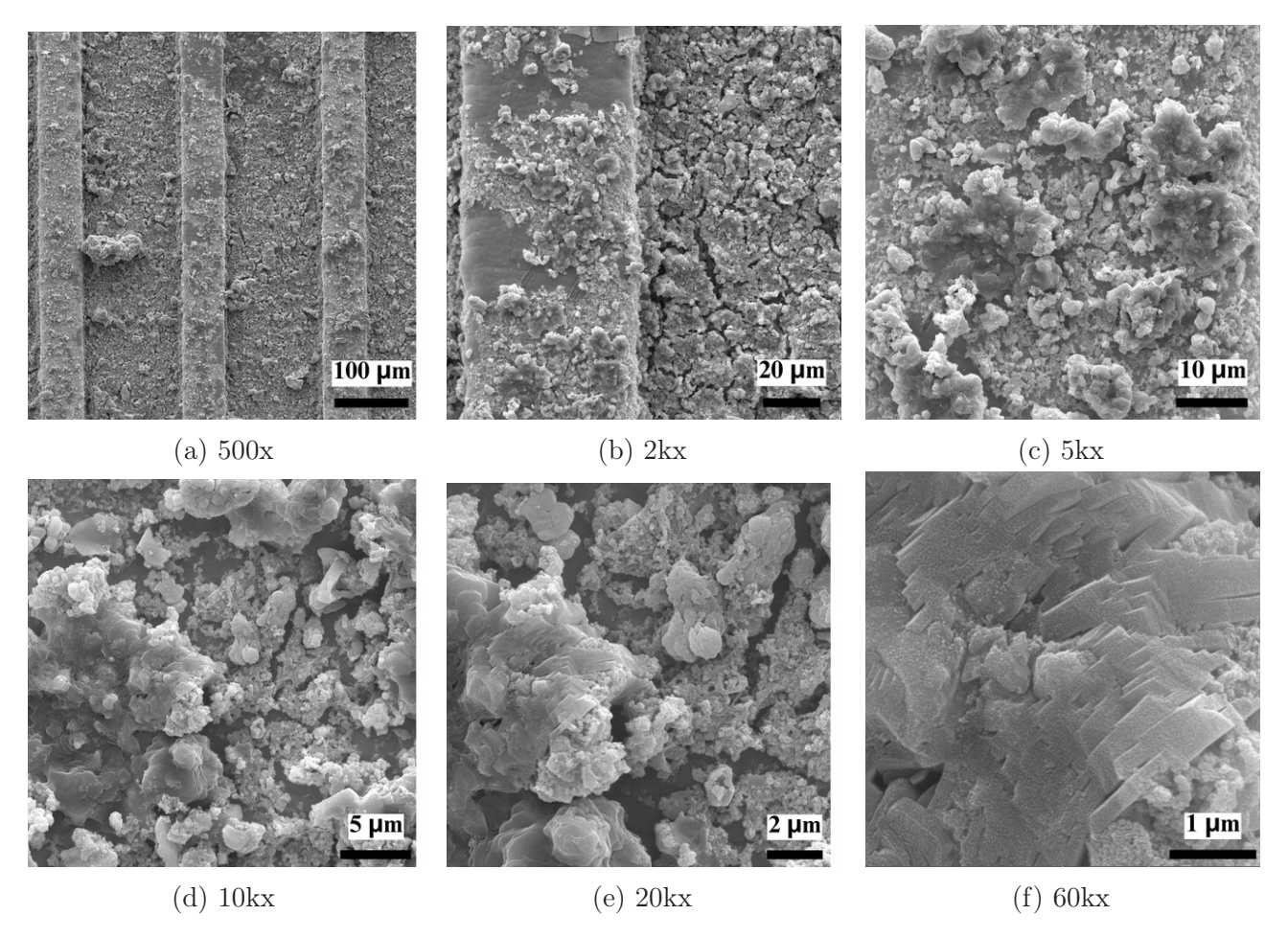


Figure 21 – SEM images of the center part of the deposition site from a device based on Timbó ash with magnifications of 500x (a), 2 kx (b), 5 kx (c), 10 kx (d), 20 kx (e) and 60 kx (f).

Following that, SEM images of the border of the deposition site of the same device demonstrate a clear contrast between the central and edge regions. Figure 22 (a) shows how the material accumulates at the border in a thick, film-like formation that connects the interdigitated electrode pairs. Since the deposition method used is drop casting, the dispersion spreads as a drop over the substrate. As the liquid evaporates, heavier particles tend to settle toward the center, while lighter components remain suspended for longer and are transported toward the edges, where they eventually accumulate. This results in a thicker deposit at the borders. Figures 22 (b) and (c) reveal that this formation consists of a dense agglomeration of porous and granular material.

For Acácia Negra, the SEM images in Figures 23 (a)–(c) show that the central region presents a morphology similar to that observed for Timbó, featuring interconnected granular regions.

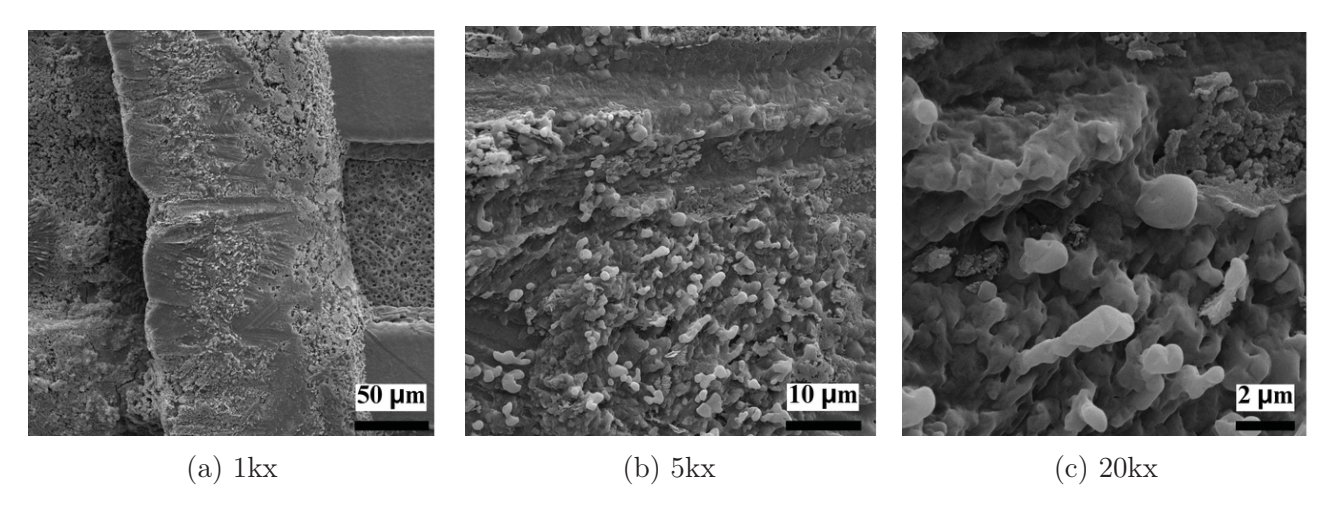


Figure 22 – SEM images of the border of the deposition site from a device based on Timbó ash with magnifications of 1 kx (a), 5 kx (b), 20 kx (c).

However, in this case, the crystalline structures appear more rod-shaped and are embedded within the porous ash matrix. At the border, shown in Figures 23 (d)–(f), a distinct morphology emerges, with the ash forming individual elongated structures with well-defined geometry. This suggests a higher degree of crystallinity, which may influence the overall sensing behavior due to local variations in porosity and active surface area. Additionally, these elongated formations are seen to span across adjacent electrodes, potentially creating direct conduction paths that can influence the electrical response of the device.

The chemical composition of the material deposited on the interdigitated substrate was analyzed using EDS, with the results presented in Figure 24. Since the electrodes are composed of ENIG, the detected Au and Ni can be attributed to this coating. The main components of the ash, namely O, Ca, C and K, are consistent with those previously identified. A notable difference is observed between the central and peripheral regions of the deposition. Comparing Figures 24 (a) and (c), which correspond to the central areas for Acácia Negra and Timbó respectively, with Figures 24 (b) and (d), representing the borders, reveals an increase in potassium content and a decrease, primarily in calcium, toward the edges. This trend suggests that calcium containing compounds, being denser, tend to settle in the central region, whereas lighter potassium based compounds accumulate near the periphery.

The FTIR data, together with the EDS analyses, suggest that the heavier component settling in the center of the deposition site is likely calcium carbonate (CaCO₃). This compound is commonly found in wood biomass ash under incomplete combustion [11], as discussed in Chapter 2, in the section about biomass ashes (Section 2.2). In addition, CaCO₃ may also form

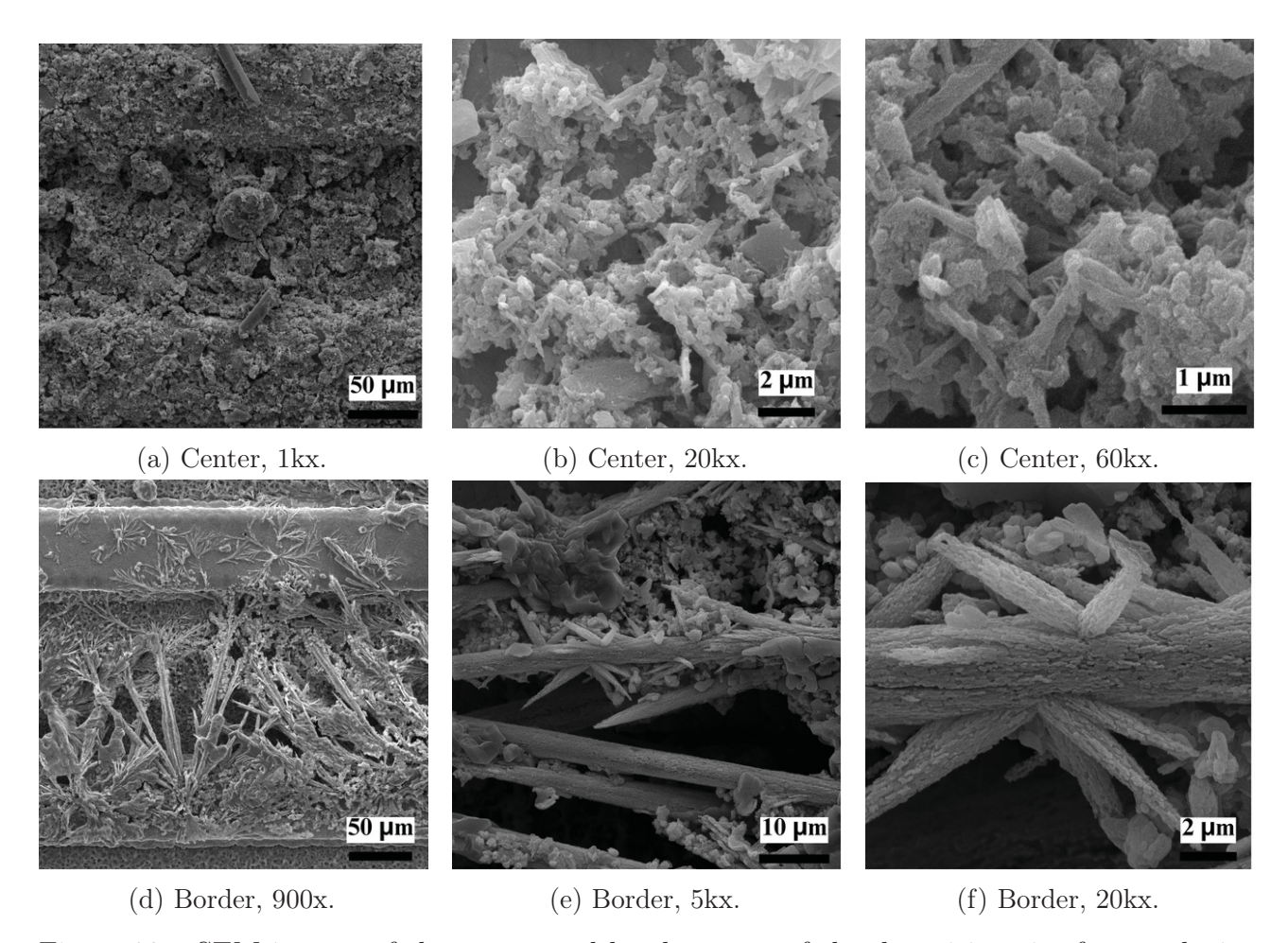


Figure 23 – SEM images of the center and border parts of the deposition site from a device based on Acácia Negra ash. (a), (b) and (c) are the center region with 1 kx, 20 kx, and 60 kx magnification, respectively, and (d), (e), and (f) are the border, with 900 x, 5 kx, and 20 kx magnification.

by recarbonation of calcium oxides generated during complete combustion when the material is exposed to ambient humidity and CO₂ [58,103], as is the case of these samples. As will be shown in Section 3.3.3, commercial CaCO₃ devices were also tested for humidity sensing but did not exhibit significant response, suggesting that this compound is not the main contributor to the sensing properties of the ash-based devices.

3.3.2 Electric Impedance Spectroscopy

Electric impedance spectroscopy was performed on four samples of each material, using the same parameters for both. The frequency spectrum ranged from 0.5 Hz to 200 kHz on a logarithmic scale, with 20 points per decade. The amplitude of the applied voltage was 0.9 V, with no DC bias. Measurements were carried out under different flow combinations in order to

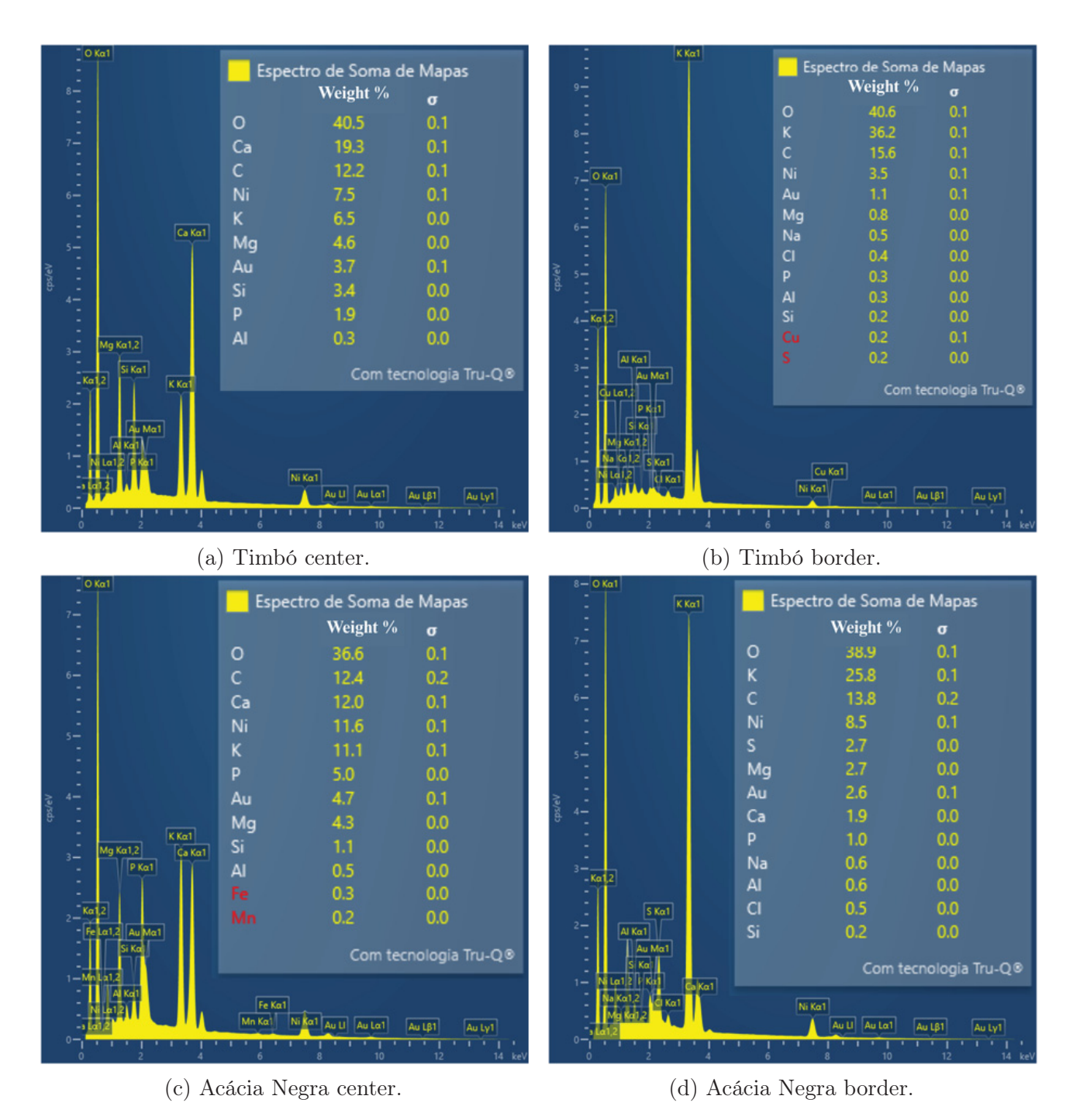


Figure 24 – EDS spectra for Timbó and Acácia Negra ash over FR4 substrate. (a) and (b) show the results for Timbó in the center and border of the deposition site, respectively, and (c) and (d) for Acácia Negra, center and border.

obtain spectra for various humidity concentrations. Since the chamber is not perfectly sealed, it is not possible to reach extreme values of relative humidity, such as 0% or 100%. Therefore, the experiment was conducted at concentrations ranging from 10% to 80%, with increments of approximately 10%.

Analyzing the Nyquist plots in Figure 25, there is a notable change in both the real and imaginary components as the relative humidity (RH) increases inside the chamber. In order to visualize all traces within the same graph, it was necessary to adopt a logarithmic scale on both axes, as shown in Figure 26. Regarding the shape and its implications, it is important to note that for all concentrations studied in this experiment, the overall shape of the curve remained consistent. However, as the concentration increased, different regions of the curve became visible. This phenomenon will be further explained, along with an extensive analysis of the curve shape, in the section on equivalent circuits (Section 3.3.4).

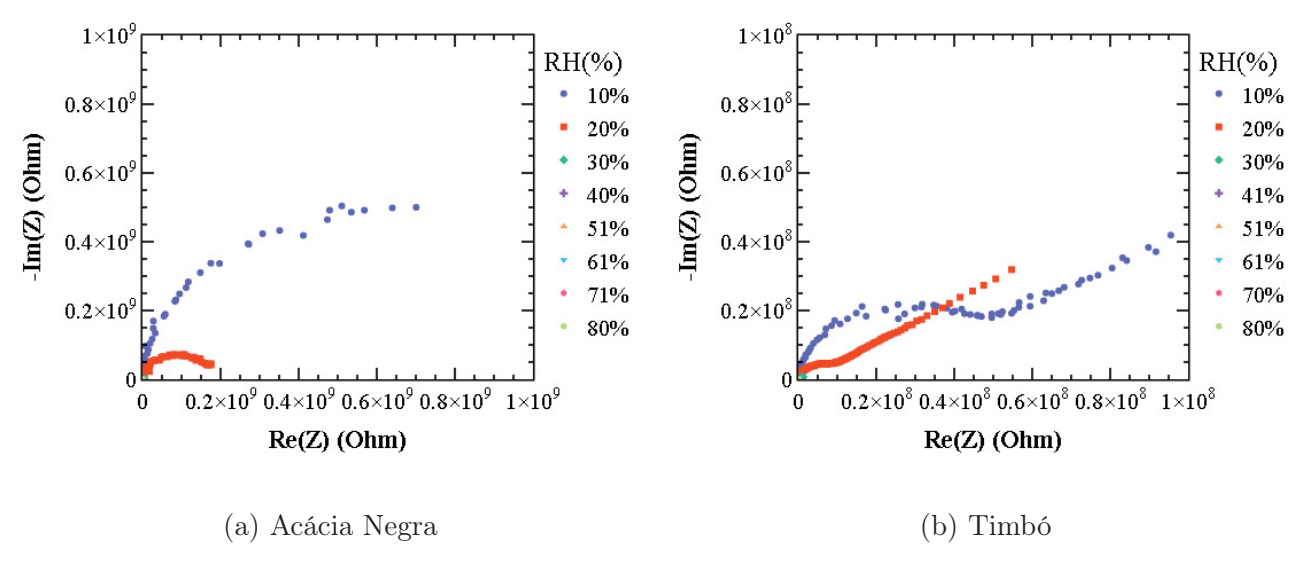


Figure 25 – Nyquist plot for sensor based on (a) Acácia Negra and (b) Timbó ash, for frequencies ranging from 0,5 Hz to 200 kHz.

It is also notable from Figure 26 that both materials exhibit similar behavior. For this reason, the analysis presented in the following paragraphs, which aims to identify the main characteristics of the electrical behavior of the sensors in order to determine the most appropriate parameters for their characterization, will be based on the Acácia Negra samples. The conclusions can also be applied to the Timbó samples. Specific differences between the results of the two materials will be discussed in the comparison section (Section 3.3.5).

When characterizing a sensor using electric impedance spectroscopy, it is necessary to select

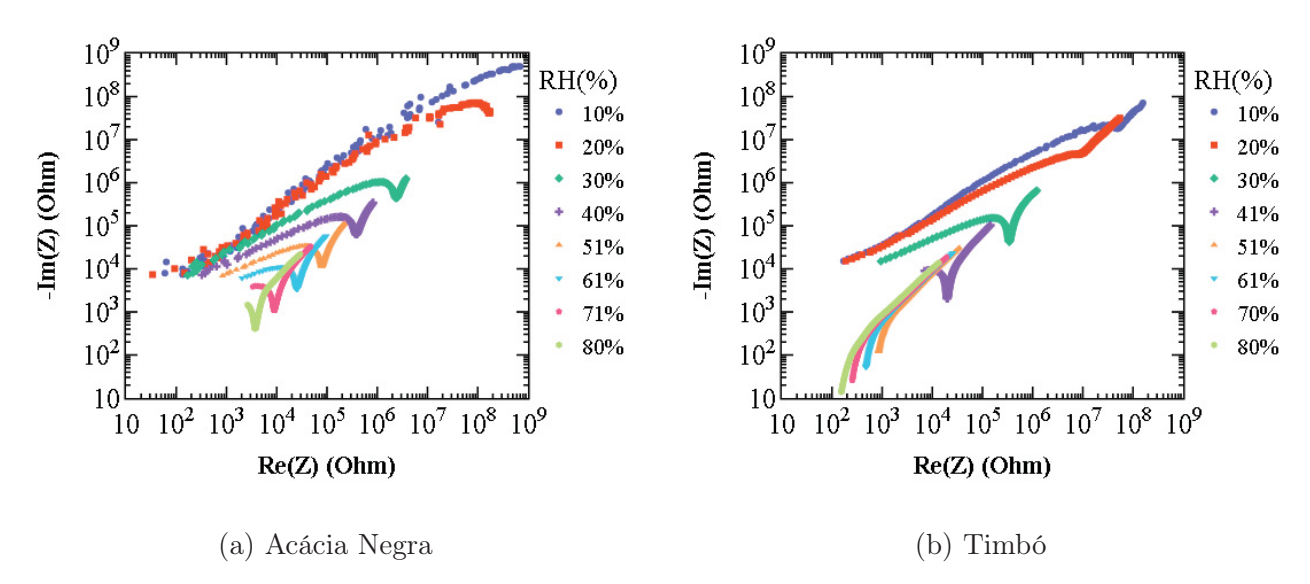


Figure 26 – Nyquist plot for sensors based on (a) Acácia Negra and (b) Timbó ash in logarithmic scale, for frequencies ranging from 0,5 Hz to 200 kHz.

which parameter will be monitored among the available ones, namely the modulus, the phase, the real part, and the imaginary part. It is also important to choose a frequency of operation at which the selected parameter will be observed as the humidity concentration varies.

As shown in the Bode plots in Figure 27, the ability to distinguish the curves for different concentrations decreases as the frequency increases. In contrast, at lower frequencies, the measurement becomes more sensitive to noise, especially for the lower humidity levels. This increased noise reduces the quality of the signal in relation to the background, which negatively affects the detection limit and the overall performance of the sensor. Therefore, both the resolution of the curves and the influence of noise must be carefully considered when selecting the most suitable frequency of operation.

From the graphs in Figure 27, it is also important to highlight that the phase and the real part of the electric impedance exhibit fluctuations along the frequency spectrum, which causes their values to not vary in a consistently increasing or decreasing manner as the relative humidity changes. In other words, as the concentration increases, these parameters may increase in some intervals and decrease in others, making it difficult to establish a clear and unambiguous correlation. This behavior can hinder the use of these parameters for sensor characterization, as discussed in Chapter 2. On the other hand, the modulus and the imaginary part of the impedance show a more monotonic behavior, meaning they consistently decrease as the concentration increases across the tested frequencies. This can be clearly seen in Figure 28, where the evolution

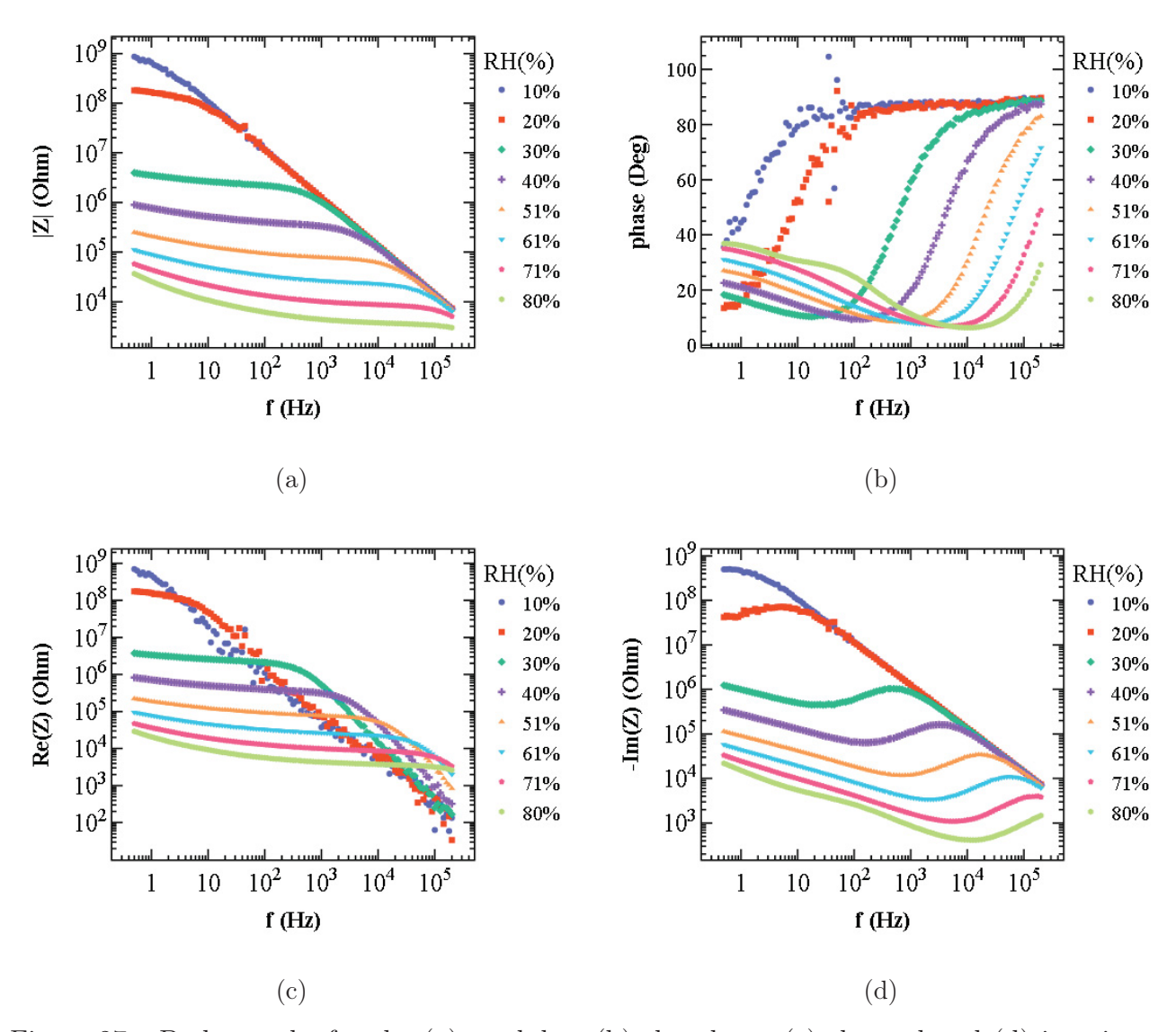


Figure 27 – Bode graphs for the (a) modulus, (b) the phase, (c) the real and (d) imaginary parts of the electric impedance of a sensor based on Acácia Negra ash, in different concentrations.

of all four parameters with respect to relative humidity is presented for some representative frequencies. As observed, while the phase and real part oscillate or change direction, the modulus and imaginary part demonstrate a clear and continuous decrease, which makes them more suitable for sensor characterization.

Physically speaking, this behavior is consistent with the discussion in Chapter 2. As the concentration increases, there is a reduction in the modulus of the impedance, which reflects a decrease in the overall resistance of the sensing material. This is expected, since the presence of more water molecules enhances the material's conductivity. Regarding the phase, and consequently the real part of the impedance, the results also align with theoretical

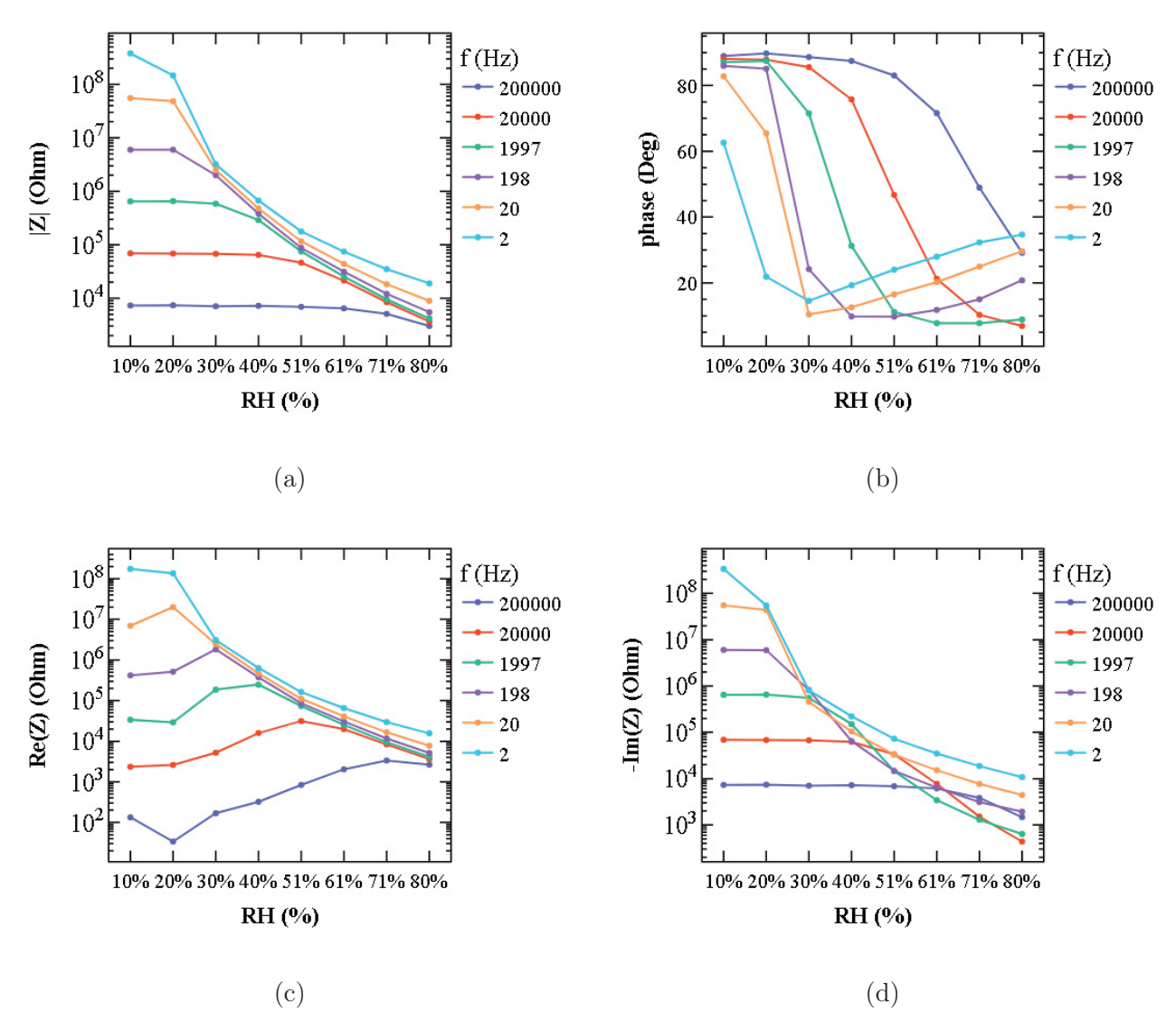


Figure 28 – Evolution of the four parameters: (a) modulus, (b) phase, (c), real part, and (d) imaginary part of the impedance, with increasing relative humidity, for some representative frequencies.

expectations: at different humidity levels, distinct electrochemical processes dominate the sensor's behavior. These shifts cause the sensor to alternate between more capacitive and more resistive characteristics, leading to the observed non-monotonic variations in phase and real impedance. These effects will be further analyzed in the equivalent circuits section (3.3.4).

It is also possible to use the sensor's response at the lowest tested concentration as a reference value, or blank, which allows for the calculation of a relative response (RR), as defined by equation (2.8). This approach provides an initial insight into the shape and behavior of the calibration curve. Figure 29 presents the RR values for each concentration, using the 10% relative humidity measurement as the baseline, and focusing on both the modulus and the

imaginary part of the impedance at some representative frequencies.

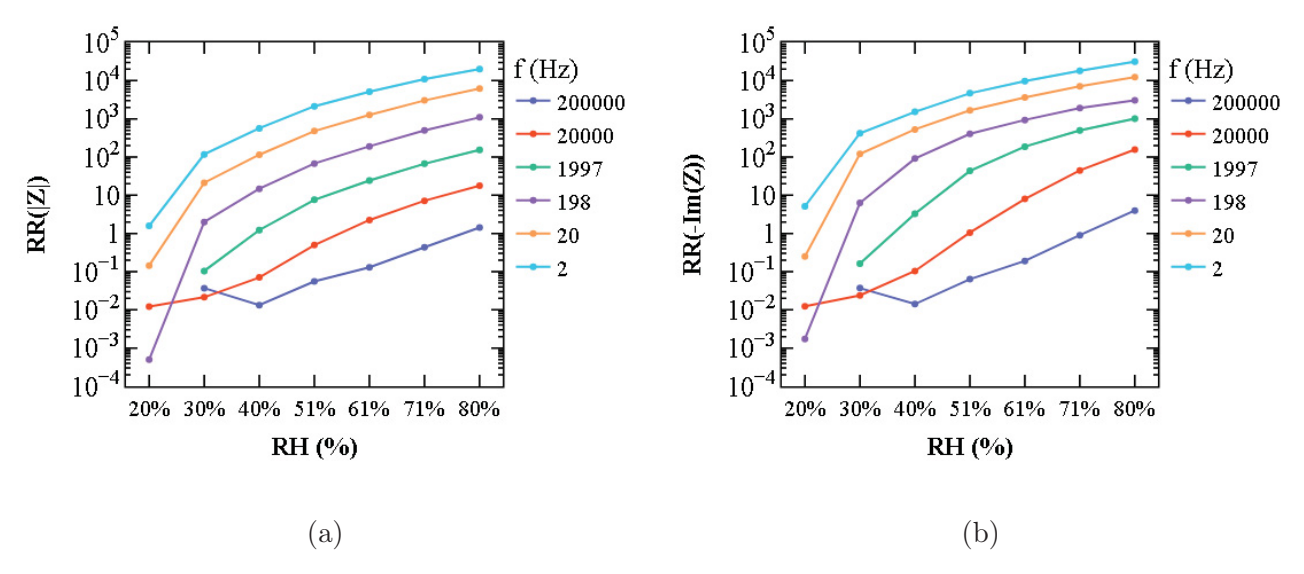


Figure 29 – Calibration curve of (a) the modulus and (b) the imaginary part of the electric impedance for some representative frequencies, using the lower concentration (10%) as the blank, for Acácia Negra based sensors.

As previously discussed, the slope of the calibration curve corresponds to the sensor's sensitivity. Since the increase in relative response exhibits an exponential behavior (further detailed in section 3.3.3), the graphs in Figure 29 are presented using a logarithmic scale. In this format, the slope indicates how many orders of magnitude (decades) the relative response increases per percentage point of relative humidity. Given that the magnitude and general behavior of the plots for both parameters are similar, the modulus was selected as the parameter for characterization in this work. This choice is justified by its more direct physical interpretation, being the ratio between the voltage and current amplitudes, whereas the imaginary part depends on both the modulus and the phase, and its interpretation can vary significantly depending on the equivalent circuit used.

From the same Figure 29, it is also evident that the relative response decreases by several orders of magnitude at higher frequencies, and that the slope of the curve, which represents the sensitivity, is smaller at lower frequencies. Therefore, the frequency chosen for the main characterization in this study was 1 kHz, as it represents a compromise between these two regimes. Additional tests at other frequencies were performed to validate the assumptions discussed here, and these results will be presented in the following section.

3.3.3 Sensor Characterization

As discussed in Chapter 2, the characterization parameters are obtained through time series analysis, in which the evolution of a selected parameter is monitored as the concentration changes. For reasons explained in Section 3.3.2, the parameter chosen for characterization in this work is the modulus of the electric impedance, and the frequency of operation is 1 kHz. For the sensors based on Acácia Negra, eight samples were tested under the same conditions, and for the ones based on Timbó, seven samples were analyzed. Although the complete results with proper statistical treatment will be shown later in this section, the data analysis procedure will first be discussed using one sample of each material.

Figure 30 presents examples of time series for two samples, one from Acácia Negra and one from Timbó, along with their corresponding calibration curves. The definition of relative response used follows equation (2.8), and the relative humidity (RH), indicated by dashed lines, was measured using the commercial SHTC3 sensor. These RH values correspond to specific combinations of flows 1 and 2, as described in the experimental setup section 3.2. The blank values used in the analysis refer to the lowest relative humidity that the system could achieve on each test day. These values are typically around 8 percent, although small variations can occur due to ambient humidity and temperature fluctuations.

It is important to highlight that these blank values are below the detection limit of the sensors, as will be confirmed by the results presented later in this section. Therefore, they are suitable to be used as baseline reference values. The goal of the measurement process is to evaluate the sensor's response over a range of concentrations that are representative of different humidity regimes, spanning from the blank value to the highest humidity level reached on the test day. The values of modulus |Z| and relative response (RR) are shown using logarithmic scale, since, as previously discussed, the response exhibits exponential variation with concentration.

In the time series presented for Acácia Negra in Figure 30 (a), the relative humidity (RH) values increase progressively throughout the measurement. In contrast, for the Timbó sample shown in Figure 30 (c), the RH first increases and then decreases. It is important to note that, for both materials, the order in which the concentrations are applied does not affect the final calibration curve. This is because the system always returns to the baseline humidity (blank) between each step in the sequence, ensuring that each concentration level is measured

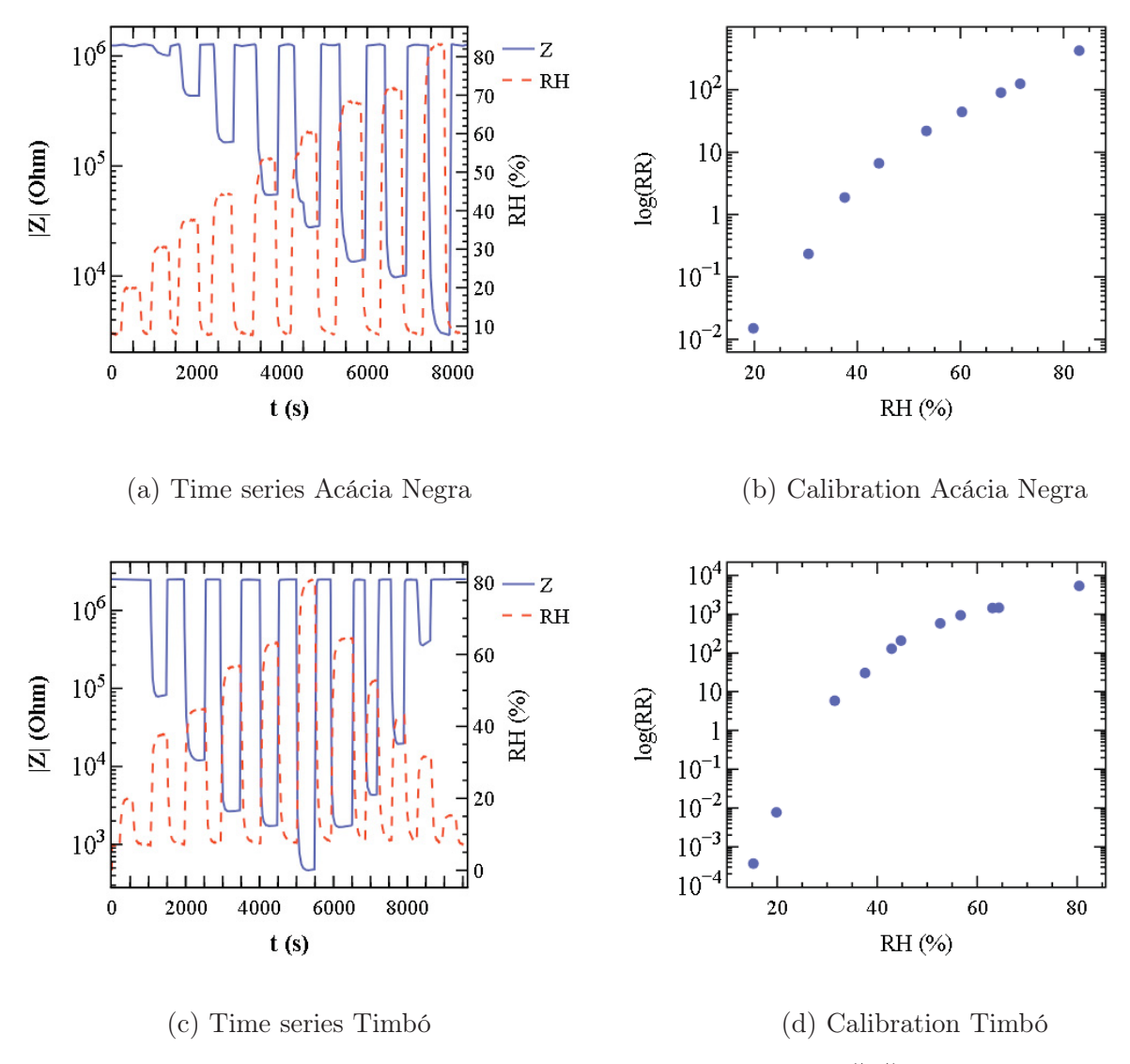


Figure 30 – Time series for the modulus of the electric impedance (|Z|) at 1 kHz and corresponding calibration curve for samples based on (a-b) Acácia Negra and (c-d) Timbó

independently under repeatable conditions.

The calibration curves shown in Figure 30 present the relationship between the relative response and the RH concentration. From both graphs, it is possible to identify two distinct calibration regimes with a transition point around 50 percent RH. These regimes can be described as regime 1 at lower concentrations and regime 2 at higher concentrations. In each regime, the response follows a linear trend, but the slope changes from one regime to the other, as further illustrated in Figure 31. To determine the limit of detection (LoD), a horizontal line can be added to these plots representing the average value of the blank plus three times its standard deviation, as discussed in chapter 2.1.3.

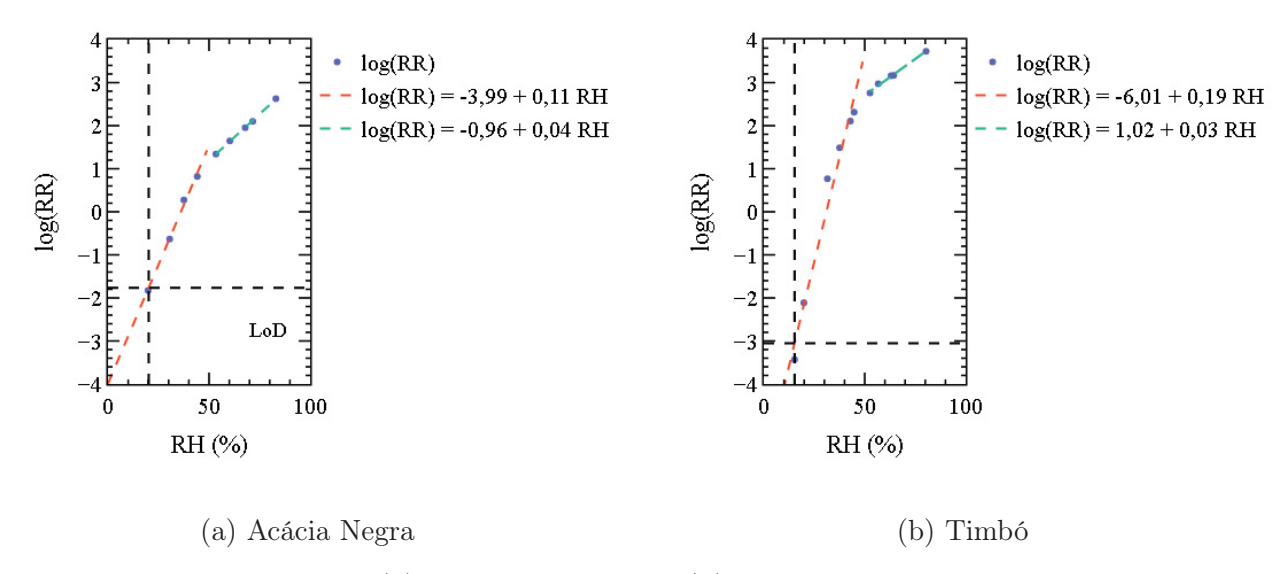


Figure 31 – Calibration for (a) Acácia Negra and (b) Timbó showing the 2 regimes of sensor operation. Limit of detection lines are presented for both cases.

The resulting calibration curves for both materials follow the expected trend based on the discussion in chapter 2. At concentrations below the limit of detection, the experiment operates in a regime where the first water molecules interact with adsorbed oxygen species on the surface of the sensing material. This interaction leads to the release of previously trapped electrons [11]. However, since the material has intrinsically high impedance, as observed from the measurements at low humidity levels, the number of released electrons is not sufficient to produce a measurable change in the electrical response. Consequently, the sensor cannot reliably distinguish these values from the baseline.

When the relative humidity exceeds the limit of detection, the experiment enters what is referred to in this work as regime 1. In this stage, water molecules begin to interact more directly with the surface of the sensing material. As previously explained, these molecules dissociate, releasing H⁺ and OH⁻ ions. The OH⁻ ions bind to defects on the surface, forming a chemisorbed layer, while the H⁺ ions contribute to charge transport by hopping between OH⁻ sites [18,37,38]. Prior studies have shown that this chemisorbed layer is typically completed around 50 percent relative humidity [37,104]. In this regime, increasing humidity enhances both carrier density and mobility. Since protons are the primary charge carriers and their mobility increases with the number of available OH⁻ sites, the impedance modulus decreases rapidly.

At even higher humidity levels, the system enters regime 2. In this regime, additional water molecules physisorb onto the existing chemisorbed layer, creating a multilayer of water on the

surface. Charge transport in this phase is governed by the Grotthuss mechanism [18,37]. By this point, the impedance has already decreased significantly due to the effects observed in regime 1. Further increases in humidity simply result in a thicker water layer, which does not cause significant additional changes in impedance. This is consistent with the lower slope of the calibration curve in regime 2.

This behavior is not exclusive to the 1 kHz frequency. Similar trends can be observed at other frequencies, as shown in Figure 32.

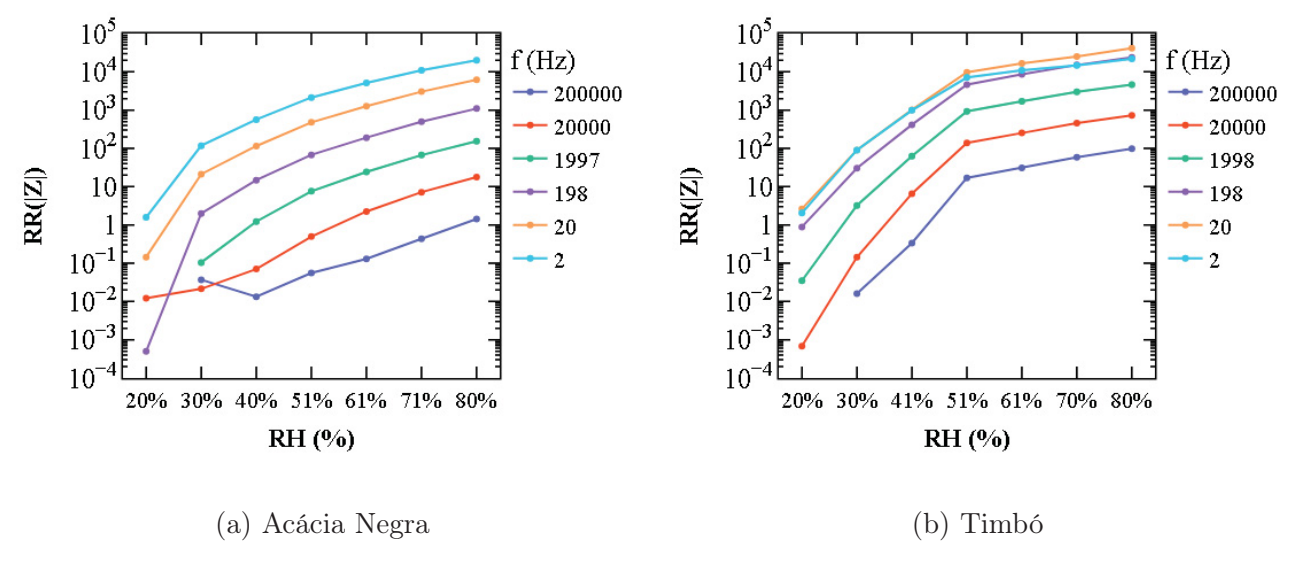


Figure 32 – Calibration curve obtained from the spectroscopy, using the lower concentration (10 %) as the blank value, for (a) Acácia Negra and (b) Timbó.

Figure 32 reveals that the transition between the two regimes occurs around 50 percent relative humidity for both materials across almost all frequencies. At very low or very high frequencies, however, this transition tends to be less pronounced or may not occur at all. This behavior can be attributed to the characteristic times associated with each physical process involved in the sensing mechanism. A more detailed discussion on this topic will be provided in section 3.3.4, where equivalent circuit models are analyzed.

The slopes of the fitted curves in Figure 31 indicate the sensitivity of the sensors in each regime, according to equation (2.9). These values are expressed in decades, or orders of magnitude, per percentage of relative humidity. From this point on, the sensitivity values obtained in regime 1 will be referred to as sensitivity 1, and those from regime 2 will be referred to as sensitivity 2. For Acácia Negra, the average sensitivity 1 was 0.10 ± 0.01 dec \cdot (%RH)⁻¹, and the sensitivity 2 was 0.04 ± 0.01 dec \cdot (%RH)⁻¹. For Timbó, the values were 0.13 ± 0.05 dec \cdot (%RH)⁻¹ for

sensitivity 1 and 0.05 ± 0.01 dec $\cdot (\% RH)^{-1}$ for sensitivity 2. The limit of detection was estimated as $22 \pm 2\%$ for Acácia Negra and $23 \pm 6\%$ for Timbó.

To evaluate the response and recovery behavior, time series measurements were conducted with relative humidity levels cycling between approximately 8 percent and 80 percent. The intervals used to compute the response and recovery times are highlighted in red and blue in Figure 33, respectively. In some cases, the red rectangles appear very small due to the fast response times observed.

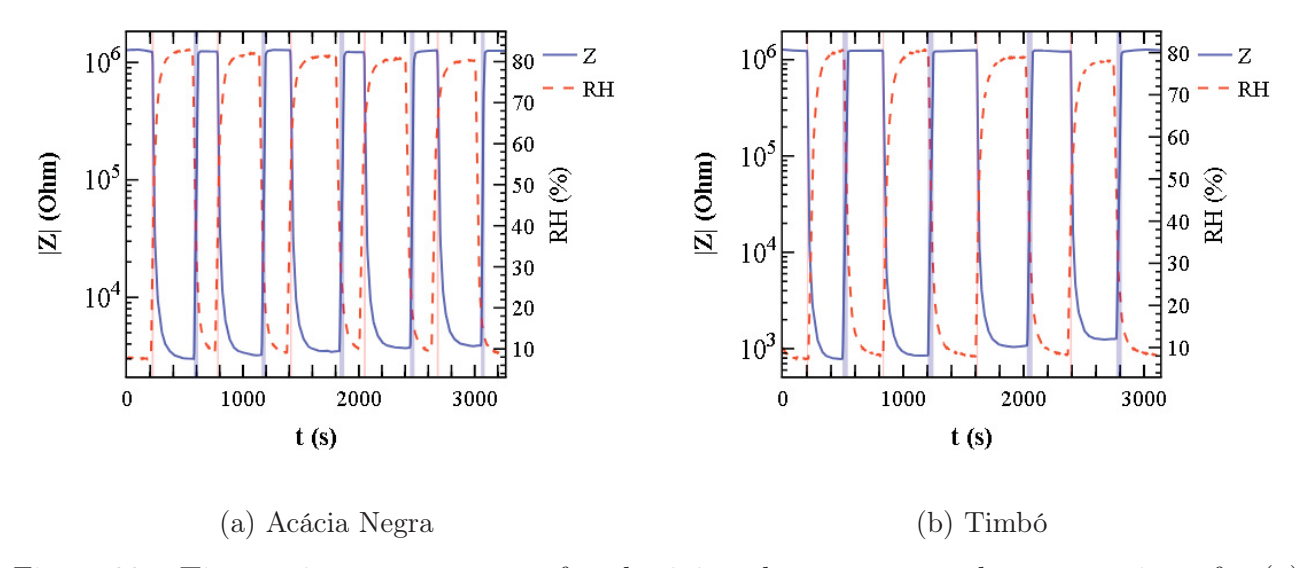


Figure 33 – Time series measurements for obtaining the response and recovery times for (a) Acácia Negra and (b) Timbó. The response and recovery intervals are marked as red and blue rectangles, respectively.

The mean values of response and recovery times for all the measurements of Acácia Negra were 18 ± 3 s and 37 ± 6 s, respectively. For Timbó, the values were 12 ± 2 s and 46 ± 2 s. A comparative analysis of all extracted parameters is presented in the comparisons section (3.3.5).

To further investigate the frequency-dependent behavior of the sensors, time series measurements were also performed at four additional frequencies besides 1 kHz: 10 Hz, 100 Hz, 10 kHz, and 100 kHz. Figure 34 presents results from four different devices based on Timbó ash. It can be observed that although the blank value of the modulus of the electric impedance decreases with increasing frequency, the relative response at different concentrations does not decrease proportionally. Consequently, the limit of detection increases with frequency. This trend is consistent with the expected behavior based on the ionic nature of the sensing mechanism, which involves processes with relatively long characteristic times. For the cases shown in Figure 34,

the estimated limits of detection were 4% at 10 Hz, 7% at 100 Hz, 31% at 10 kHz, and 35% at 100 kHz.

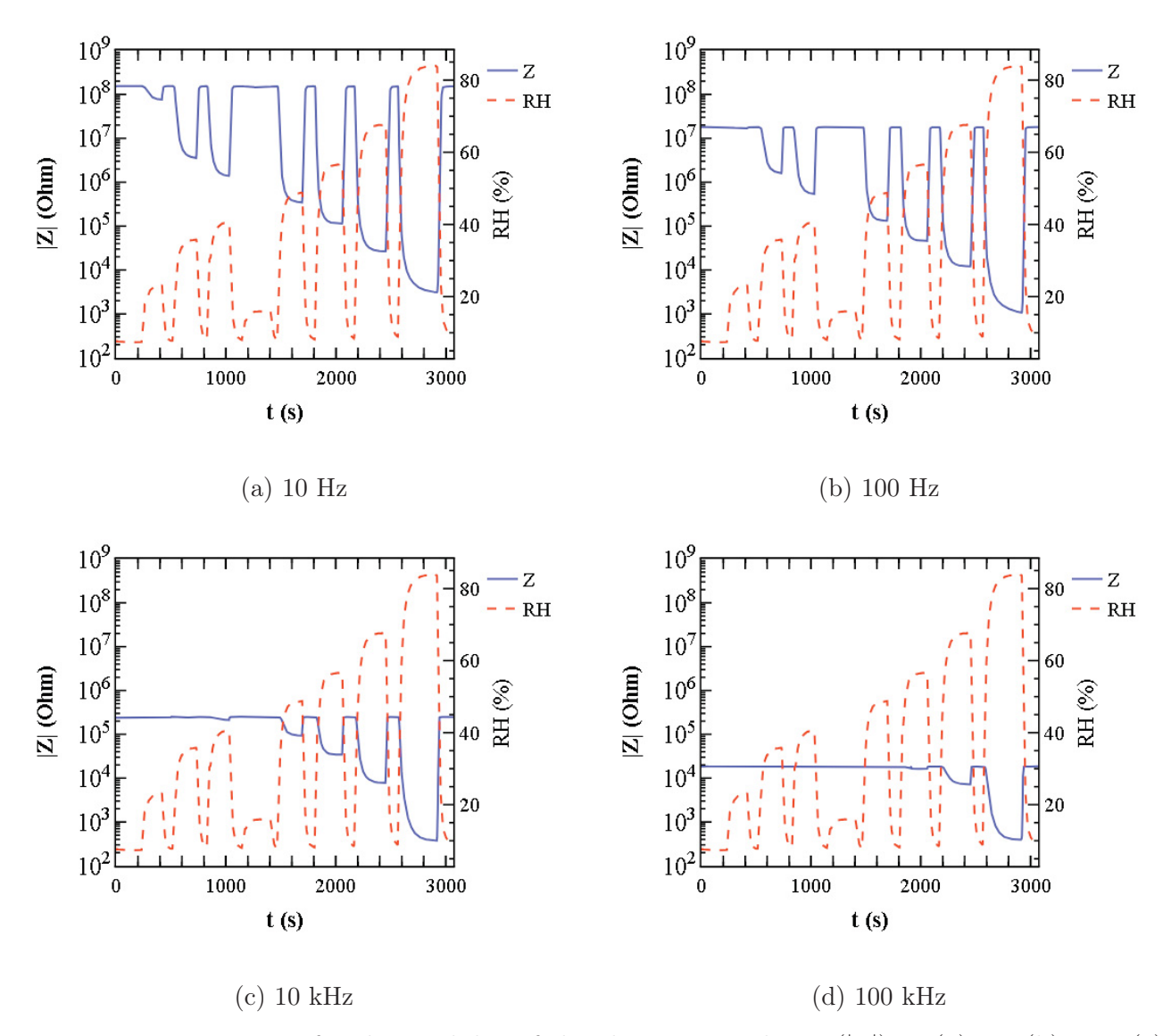


Figure 34 – Time series for the modulus of the electric impedance (|Z|) at (a) 10, (b) 100, (c) 10 k, and (d) 100 kHz for samples based on Timbó ash

For the other parameters, sensitivity 1 gradually decreased with frequency, from 0,13 dec $(\%RH)^{-1}$ at 10 Hz to 0,03 dec $(\%RH)^{-1}$ at 100 kHz, while sensitivity 2 increased, from 0,06 dec $(\%RH)^{-1}$ at 10 Hz to 0,09 dec $(\%RH)^{-1}$. This behavior is consistent with the expected response dynamics: at low frequencies, the sensor is more responsive to lower concentrations due to the compatibility between the characteristic time of the ionic processes and the excitation signal, resulting in a higher sensitivity 1. As frequency increases, the sensor becomes less responsive at low concentrations, reducing sensitivity 1, but starts to exhibit stronger responses at higher concentrations, where the relative impedance variation becomes more pronounced,

thereby increasing sensitivity 2.

The response and recovery times are also influenced by the frequency of operation. As frequency increases, the blank value of the impedance approaches the saturation value observed at high concentrations. Because the response is defined in terms of reaching a certain percentage (e.g., 90%) of the total signal variation, a smaller amplitude of variation results in a longer response time. Conversely, the recovery time shortens, since returning to a low percentage (e.g., 10%) of a smaller signal range occurs more quickly. As a result, the response time increased from approximately 10 s at 10 Hz to 88 s at 100 kHz, while the recovery time decreased from 54 s at 10 Hz to 15 s at 100 kHz. These results indicate that sensor behavior can be tuned for different applications by adjusting the operating frequency.

Finally, in the structural characterization section (3.3.1), it was suggested that these materials are composed of, among other compounds, calcium carbonate (CaCO₃). To verify its contribution, four sensors were fabricated using a solution of 10 mg/mL of CaCO₃ in deionized water, and the results are presented in Figure 35.

The results show that although the CaCO₃-based devices do exhibit a response to relative humidity, the magnitude of the response is significantly lower than that observed in the devices based on ash. Therefore, the sensing behavior of the original sensors cannot be attributed solely to the presence of CaCO₃. It is worth noting that morphology plays a crucial role in the performance of sensing devices, as it affects parameters such as surface area and porosity and the morphology of the CaCO₃ present in the ash might be different from that of the commercial material.

3.3.4 Equivalent Circuits

To propose an equivalent circuit that accurately represents the behavior of a physical system, it is necessary to reconcile the system's physical properties with the electrical response observed through impedance spectroscopy. The Nyquist diagram is typically used as the starting point, as the geometry of the curve provides insight into the probable elements that compose the circuit. Figure 36 shows the Nyquist diagrams for Acácia Negra devices at 40% RH and for Timbó devices at 30% RH. These specific concentrations were selected because the full shape of the impedance response is clearly visible at these levels, allowing for a more complete analysis.

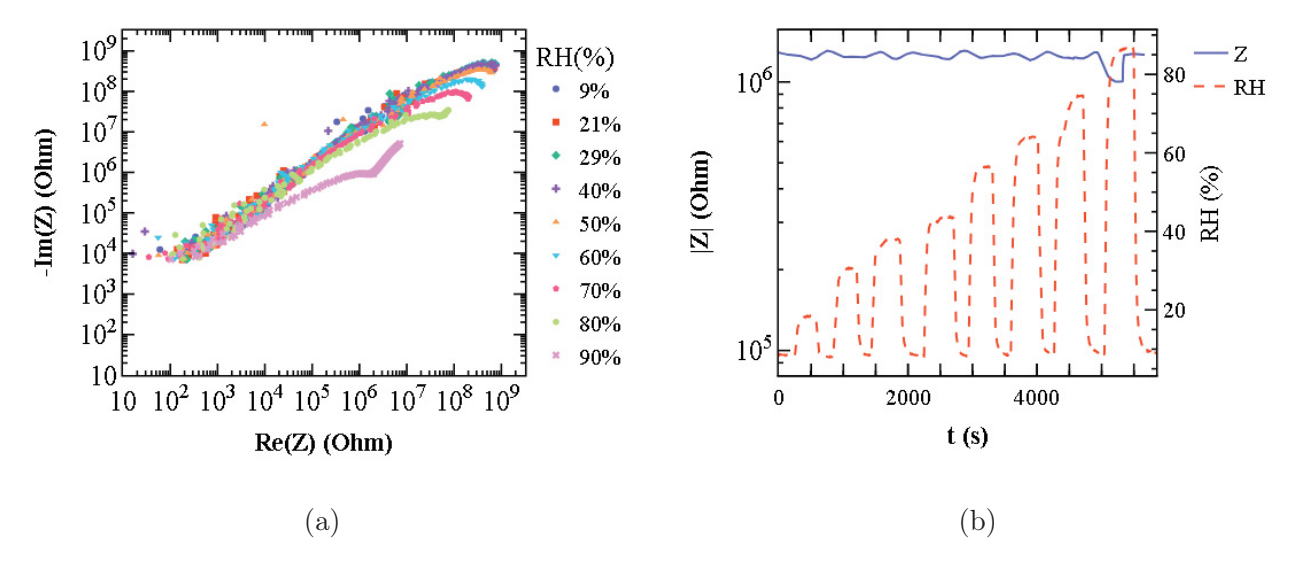


Figure 35 – Nyquist plot (a) and time series (b) for a sample based on CaCO₃.

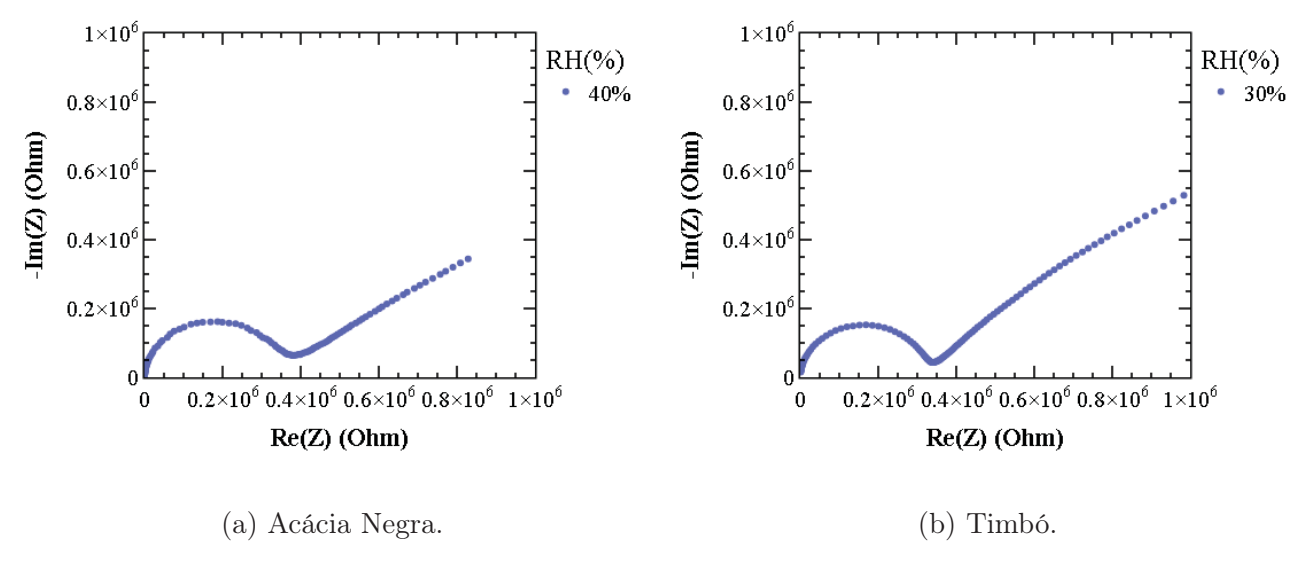


Figure 36 – Nyquist diagram for (a) Acácia Negra and (b) Timbó devices at 40 % and 30 % RH, respectively.

The first conclusion drawn from Figure 36 is that the shapes of the curves for both devices are very similar. Therefore, the following analysis will focus on the Acácia Negra device and can be extended to the Timbó device by analogy.

At high frequencies (near the origin of the Nyquist diagram), the impedance response resembles that of a semicircle, which is characteristic of a parallel RC circuit. This suggests that, in this frequency range, the system behaves predominantly like a resistor and capacitor in parallel.

As the frequency decreases and the curve moves away from the semicircular region, the impedance vector assumes a nearly constant phase angle between 0° and 90°, forming a straight line in the Nyquist plot with an intermediate slope. This behavior is typical of a Constant Phase Element (CPE), a component often used to model distributed or non-ideal capacitive behavior, with an exponent $0 < \alpha < 1$.

Focusing initially on the semicircular portion, we assume the system behaves as an RC parallel circuit. In the high-frequency limit, the impedance is dominated by the capacitive element, with the modulus tending toward that of a capacitor and the phase approaching 90°. A capacitor model can thus be fitted to this portion of the data to obtain an initial estimate for the capacitance, as shown in Figure 37.

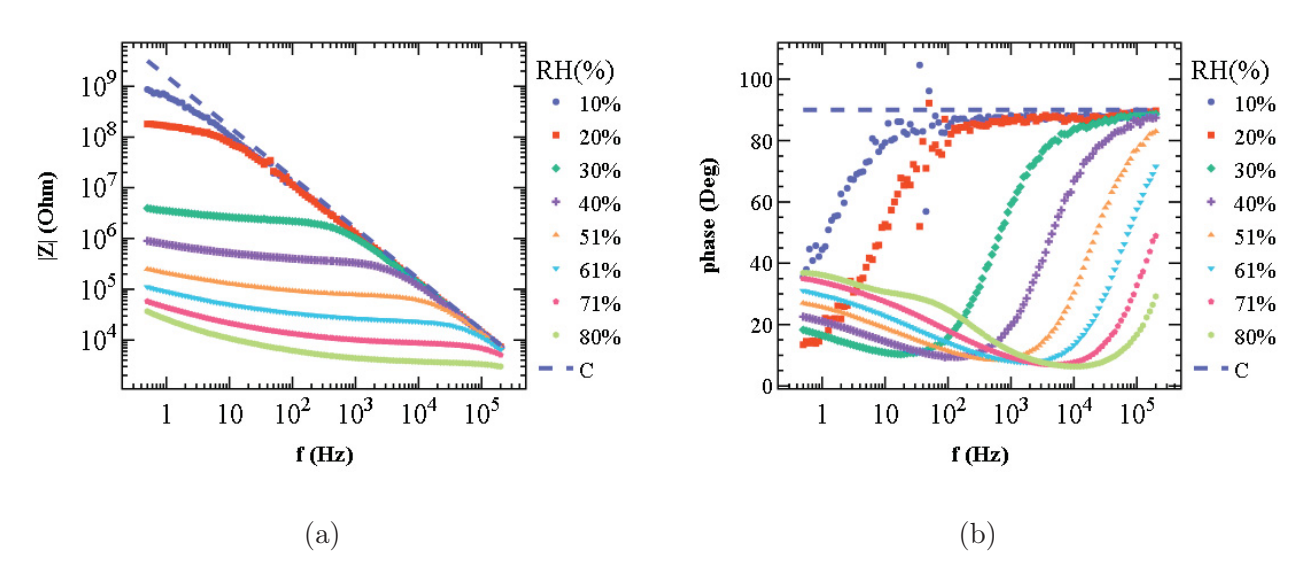


Figure 37 – Bode graph for (a) modulus and (b) phase. The points represent experimental data for various concentrations and the dashed line corresponds to the simulated capacitor of 0.135 nF.

The sensor's behavior at high frequencies approaches that of a capacitor with a value of

approximately 0.135 nF, as indicated by the simulation. This capacitance represents charge accumulation processes with a very short characteristic time, owing to its low value and dominance at high frequencies. Moreover, this behavior is concentration-independent, as all concentrations converge to the same response in this frequency regime.

Examining the real part of the impedance reveals that this component cannot be an ideal capacitor, since a capacitor's impedance is purely imaginary. The Bode plot for the modulus in Figure 38 demonstrates that the device approaches a straight line in a log-log plot, indicating a power-law relationship between the modulus and frequency. The slope of this line corresponds to the exponent, which in this case is close to but not exactly 1. Replacing the capacitor with a CPE (constant phase element) having an exponent near 1 resolves this issue while preserving the solution for both phase and modulus.

Figure 38 presents a simulation of a CPE with an exponent $\alpha = 0.99$ for both modulus and real part. Given that the exponent is nearly 1, the phase approximates 90°, and the imaginary part converges to the modulus. Consequently, graphs for these two parameters are straightforward and do not require additional simulation.

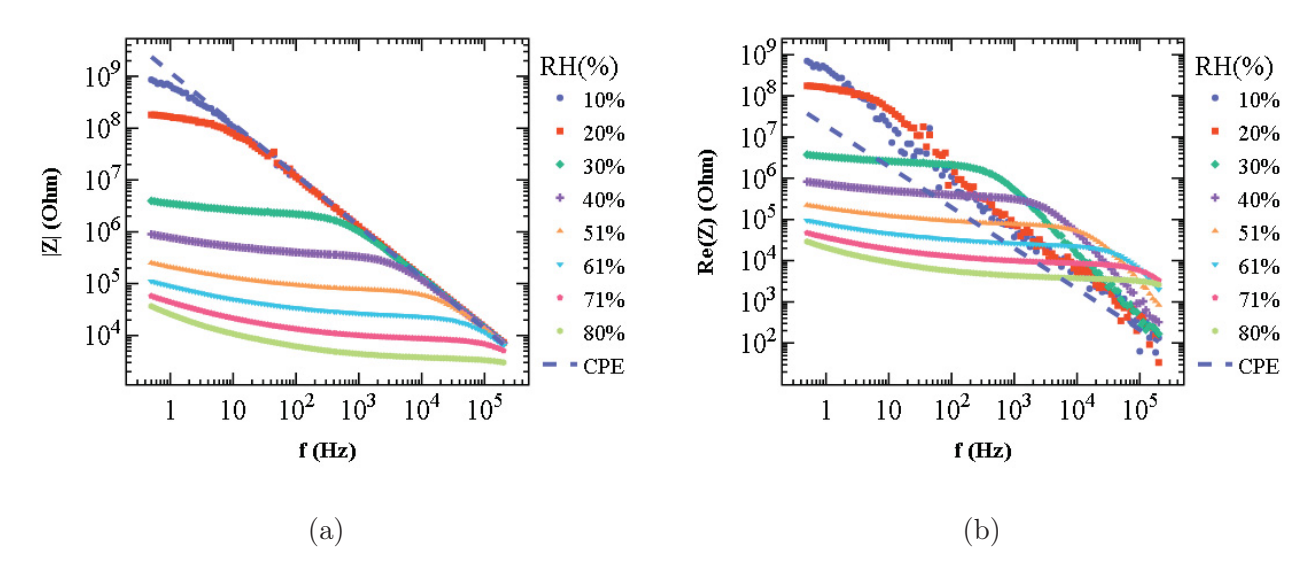


Figure 38 – Bode graphs for (a) modulus and (b) real part of the electric impedance with the simulation of a CPE. The points represent experimental data for various concentrations and the dashed line corresponds to the simulated CPE with exponent $\alpha = 0.99$ and $T = 0.135 \ n(F.s^{\alpha-1})$.

Analyzing the Nyquist plot in Figure 36, we observe that in the low-frequency regime (right side of the plot), the system approaches a CPE whose response does not begin at the origin. This behavior must therefore be modeled by a resistor in series with a CPE.

Figure 39 shows the modulus and phase, along with simulated responses for both frequency limits, for the Acácia Negra device at 40% RH. The high-frequency regime is well described by the initial CPE (denoted CPE1 hereafter), while the low-frequency response requires a resistor $R = 3.2 \times 10^5 \ \Omega$ in series with a second CPE (CPE2), where CPE2 has parameters $\alpha_2 = 0.38$ and $T_2 = 1 \times 10^{-6} \ {\rm F} \cdot {\rm s}^{\alpha_2-1}$.

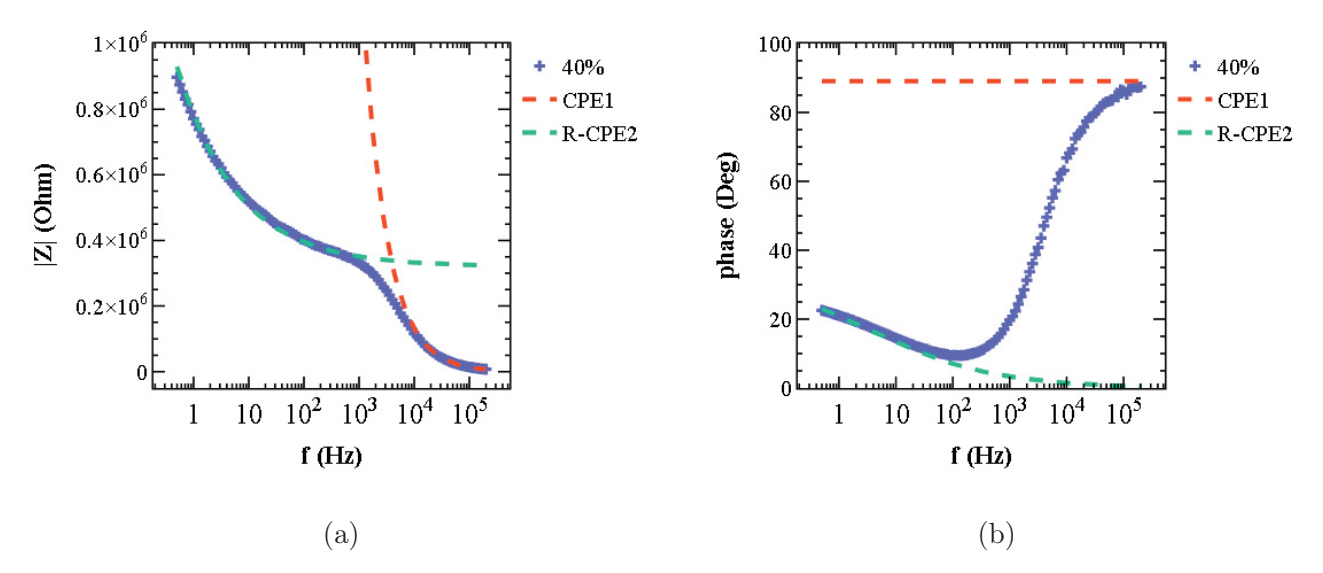


Figure 39 – Bode graph for (a) modulus and (b) phase of a device based on Acácia Negra, at 40% RH, with CPE1 and R-CPE2 simulated. The points represent experimental data and the dashed lines correspond to the simulations: CPE1 with exponent $\alpha_1 = 0.99$ and $T_1 = 0.135$ nF · s^{α_1 -1} for the high-frequency regime, and R-CPE2 with $R = 3.2 \times 10^5$ Ω , $\alpha_2 = 0.38$ and $T_2 = 1 \times 10^{-6}$ F · s^{α_2 -1} for low-frequency.

The proposed elements accurately describe the device behavior in both frequency limits. Therefore, the equivalent circuit must incorporate both solutions and simulate their transition. Figure 40 presents the complete circuit along with Nyquist and Bode plots (showing both modulus and phase) of the simulated device response.

A complete analytic expression for the impedance of the proposed circuit is derived in Section 3.3.4.1 and was used to generate all simulated curves presented in this work. Notably, while the same circuit components describe the behavior for all concentrations, their specific parameter values require appropriate adjustment. Figure 41 presents simulated curves for all concentrations for both materials and a bar graph showing the concentration-dependent parameter values.

At high frequencies, CPE1 dominates and its parameters remain constant for both materials, with $\alpha = 0.99$ for each, and $T = 0.135 \text{ n}(F \cdot s^{1-\alpha})$ for Acácia Negra and $0.05 \text{ n}(F \cdot s^{1-\alpha})$ for

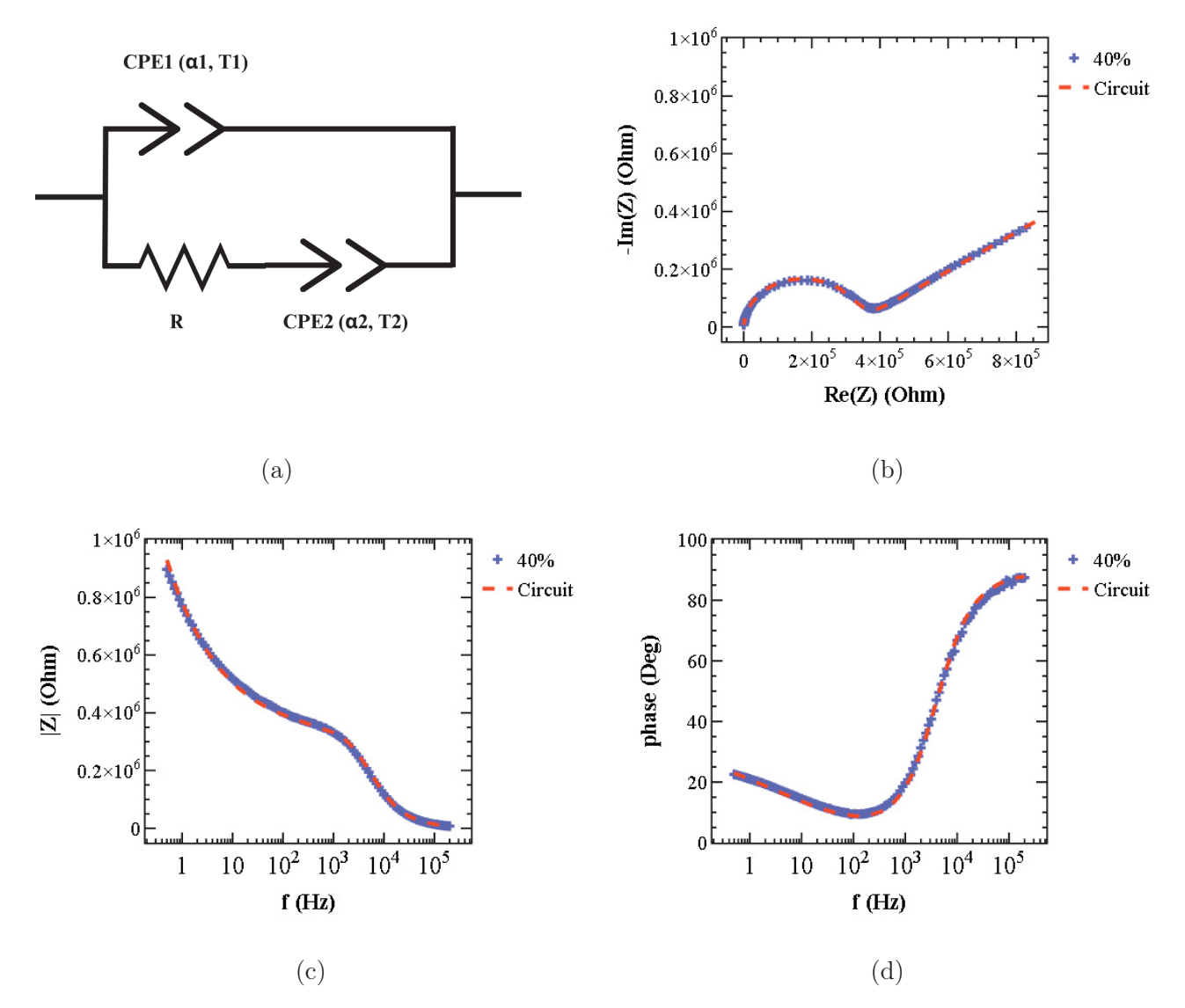


Figure 40 – Proposed equivalent circuit (a) and the simulated curves in (b) the Nyquist plot and the Bode graphs for (c) the modulus and (d) the phase of the electric impedance of a device based on Acácia Negra at 40% RH. The points represent experimental data while the dashed line corresponds to the simulated circuit with the following parameters: $\alpha_1 = 0.99$, $T_1 = 0.135$ nF · s^{α_1-1}, $R = 3.2 \times 10^5$ Ω , $\alpha_2 = 0.38$, $T_2 = 1 \times 10^{-6}$ F·s^{α_2-1}.

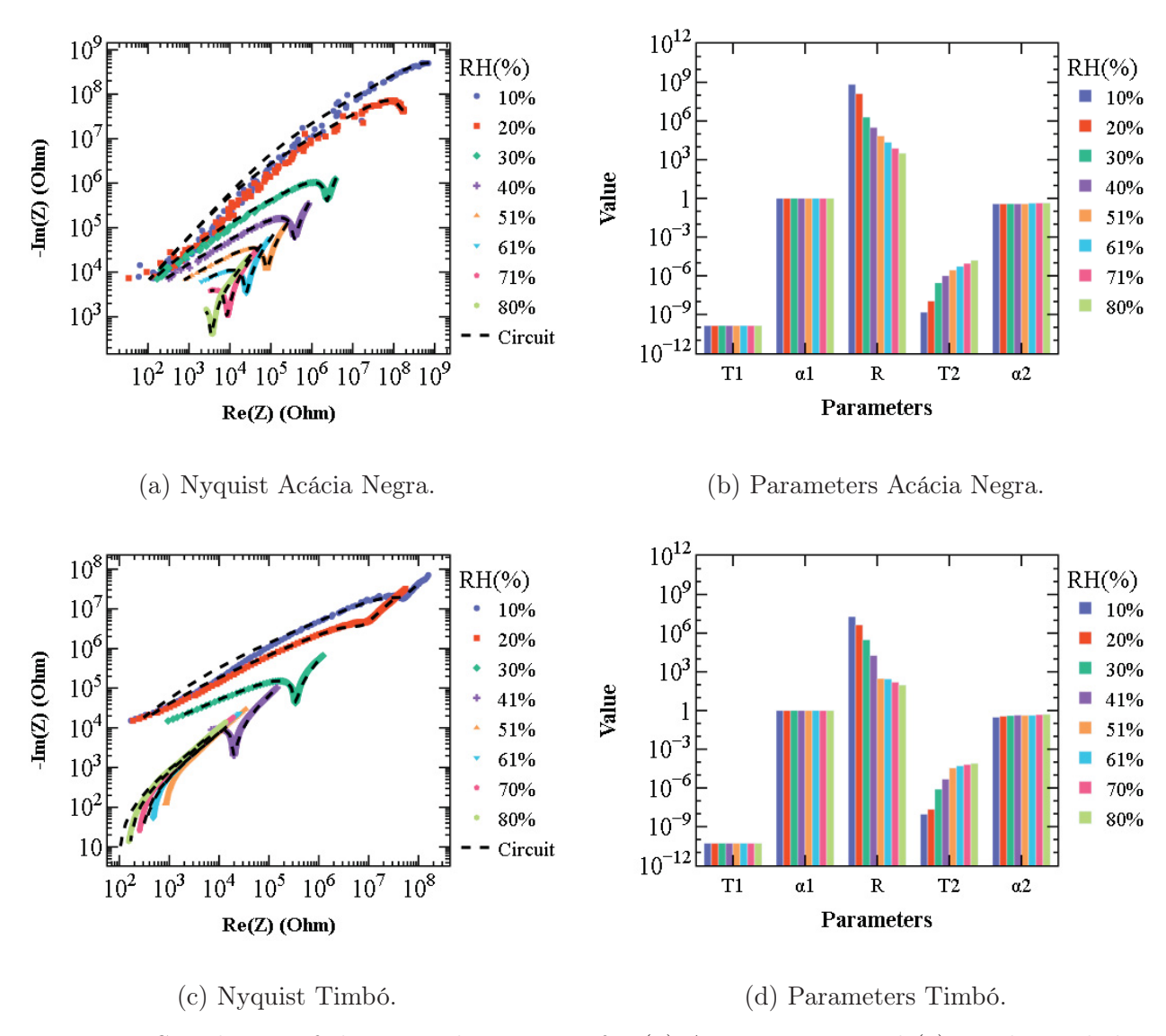


Figure 41 – Simulation of the equivalent circuit for (a) Acácia Negra and (c) Timbó and their parameter values by concentration (b,d).

Timbó. These parameter values indicate that CPE1 behaves almost like an ideal capacitor with very low capacitance (represented by T_1), which does not vary with concentration. Since the interaction with the analyte mainly introduces ionic species, there is no influence on the material's behavior at high frequencies because these species exhibit higher inertia than lighter charge carriers such as electrons or holes. In this context, CPE1 represents the configuration composed of two interdigitated electrodes separated by the active material, which acts as an almost ideal dielectric medium. At high frequencies, as the oscillation period becomes very short, only the contribution from lighter carriers oscillating at a characteristic time close to this period remains [37,38].

The Nyquist diagrams in Figure 41 (a) and (c), display an inversion region in the imaginary

part evolution for nearly every curve, corresponding to the right limit of the semicircle. Since the coefficient T_1 of CPE1 is smaller for Timbó, the characteristic time of this process is also smaller for this material, explaining why the lower frequency phenomena to the right of the inversion appear at lower concentrations for Timbó than for Acácia Negra.

At low frequencies, charge transport becomes dominated by ionic species resulting from the interaction with the analyte, a phenomenon characterized by longer times due to the carriers' inertia and transport nature. Initially, these ionic species occupy adsorption sites, and as the electric field pushes them, a certain time is required to overcome the potential well and drift to neighboring sites. This process can be modeled as a series of resistors and non-ideal capacitors (CPEs) connected in series, where the resistive behavior arises from carrier interactions with the medium during site-to-site drift, and the capacitive behavior stems from potential barriers and carrier inertia. This succession is represented here by an equivalent resistor (R) and an equivalent constant phase element (CPE2) in series. The parameter values for these elements are strongly affected by concentration up to approximately 50% RH, defined as regime 1 in Section 3.3.3. In this regime, conduction is dominated by protons (H^+) hopping between hydroxide ions (OH⁻) via the hydroxide Grotthuss mechanism [18]. Concentration directly influences carrier density and mobility, leading to a sharp reduction in resistance (R). At higher concentrations, this reduction is less pronounced because, in regime 2, multiple water layers form on the material surface. The conduction is now dominated by the Grotthuss mechanism, so increasing concentration expands water layers and facilitates proton transport, but less dramatically than in regime 1. Regarding CPE2 parameters, T_2 increases, implying a reduction in impedance since the impedance of a CPE is inversely proportional to T. Physically, this behavior follows the same reasoning as the reduction of R, with T_2 rising alongside R decreasing. The exponent α_2 exhibits a slight increase (ranging from 0.38 to 0.45 for Acácia Negra and from 0.3 to 0.5 for Timbó), indicating a mild increase in capacitive behavior during the transition from regime 1 to regime 2.

3.3.4.1 Analytic expression for the impedance of the proposed circuit

The idea is to analyze the total impedance of a circuit composed of a parallel association between CPE1 and R-CPE2:

$$Z_{\text{CPE1}} = \frac{1}{T_1(i\omega)^{\alpha_1}},\tag{3.1}$$

$$Z_{\text{R-CPE2}} = R + \frac{1}{T_2(i\omega)^{\alpha_2}}.$$
(3.2)

The total impedance of the parallel configuration is:

$$Z_{\text{total}} = \left[\frac{1}{Z_{\text{CPE}_1}} + \frac{1}{Z_{\text{R-CPE}_2}}\right]^{-1} = \left[T_1(i\omega)^{\alpha_1} + \frac{1}{R + \frac{1}{T_2(i\omega)^{\alpha_2}}}\right]^{-1},$$
 (3.3)

where the second term in the denominator can be simplified to:

$$\frac{1}{R + \frac{1}{T_2(i\omega)^{\alpha_2}}} = \frac{T_2(i\omega)^{\alpha_2}}{RT_2(i\omega)^{\alpha_2} + 1},$$
(3.4)

and thus, the total impedance becomes:

$$Z_{\text{total}} = \left[T_1 (i\omega)^{\alpha_1} + \frac{T_2 (i\omega)^{\alpha_2}}{R T_2 (i\omega)^{\alpha_2} + 1} \right]^{-1}. \tag{3.5}$$

To separate real and imaginary parts, the following relation can be used:

$$(i\omega)^{\alpha} = \omega^{\alpha} \cdot i^{\alpha} = \omega^{\alpha} \left[\cos \left(\frac{\alpha \pi}{2} \right) + i \sin \left(\frac{\alpha \pi}{2} \right) \right]. \tag{3.6}$$

To simplify the next steps, it is useful to define:

$$a = T_1 \omega^{\alpha_1} \cos\left(\frac{\alpha_1 \pi}{2}\right),$$
 $b = T_1 \omega^{\alpha_1} \sin\left(\frac{\alpha_1 \pi}{2}\right),$ (3.7)

$$u = T_2 \omega^{\alpha_2} \cos\left(\frac{\alpha_2 \pi}{2}\right), \qquad v = T_2 \omega^{\alpha_2} \sin\left(\frac{\alpha_2 \pi}{2}\right),$$
 (3.8)

thus:

$$T_1(i\omega)^{\alpha_1} = a + ib, \quad T_2(i\omega)^{\alpha_2} = u + iv. \tag{3.9}$$

Now, simplifying the second term in equation (3.5):

$$\frac{T_2(i\omega)^{\alpha_2}}{RT_2(i\omega)^{\alpha_2} + 1} = \frac{u + iv}{(Ru + 1) + iRv},$$
(3.10)

multiplying the numerator and denominator by the complex conjugate, and expanding the denominator to obtain the real and imaginary parts of it, defined here, for simplicity, as A and B:

$$A = \text{Re (second term)} = \frac{u(Ru+1) + v^2 R}{(Ru+1)^2 + (Rv)^2},$$
(3.11)

$$B = \text{Im (second term)} = \frac{v(Ru+1) - uRv}{(Ru+1)^2 + (Rv)^2},$$
(3.12)

the total impedance becomes:

$$Z_{total} = [(a+A) + i(b+B)]^{-1}. (3.13)$$

Finally, multiplying the numerator and the denominator by the complex conjugate, the real and imaginary parts can be obtained:

$$Re(Z_{total}) = \frac{a+A}{(a+A)^2 + (b+B)^2}$$
 (3.14)

$$Im(Z_{total}) = -\frac{b+B}{(a+A)^2 + (b+B)^2}.$$
 (3.15)

3.3.5 Comparisons

Table 2 presents the values of all characterization parameters for devices based on Acácia Negra and Timbó, using the modulus of the electric impedance at 1 kHz. The values are similar and, except for the response and recovery times, fall within one standard deviation of each other. This observation is consistent with the pattern described in the equivalent circuits section (3.3.4), where the behavior of devices using the two ashes showed strong similarity.

Table 2 – Characterization parameters for Acácia Negra and Timbó ash based devices.

Parameters	Acácia Negra	Timbó
LoD (% RH)	22 ± 2	23 ± 6
Response time (s)	18 ± 3	12 ± 2
Recovery time (s)	37 ± 6	46 ± 2
Sensitivity 1 [$\operatorname{dec} \cdot (\%RH)^{-1}$]	$0,\!10\pm0,\!01$	0.13 ± 0.05
Sensitivity 2 [$\operatorname{dec} \cdot (\%RH)^{-1}$]	0.04 ± 0.01	0.05 ± 0.01

Regarding literature values, Table 3 compares the parameters of both materials with similar studies mentioned in the state of the art section (2.1.4). It is evident that impedimetric analysis

Table 3 – Comparison between this work and similar studies from the literature.

Material	Signal	Sensitivity	$\begin{array}{c} {\rm RH} \\ {\rm Limits} \end{array}$	${\rm Resp./Rec.}$	Ref.
PEEK-co- PEG/LiCl	Impedimetric	$0.062 \ log(Z) \cdot (\%RH)^{-1}$	11-97%	$3\ /\ 52\ \mathrm{s}$	[37]
CuO	Impedimetric	22611%	1397%	32 / - s	[38]
GO	Impedimetric	1117.3	1193%	5 / 11 s	[39]
Paper	Resistive	1647	41–91%	$472~/~19~\mathrm{s}$	[42]
Paper ash	Resistive	10^{6}	1590%	$2 / 10 \mathrm{\ s}$	[11]
Potato peel	Resistive	$70 \ k\Omega \cdot (\%RH)^{-1}$	45-80%	$0,96 \ / \ 1,65$ s	[10]
Rice husk ash	Resistive	_	0 – 93%	$20~/~23~\mathrm{s}$	[43]
Acácia Negra ash	Impodimotric	Sens. 1: $0.10 \text{dec} \cdot (\%RH)^{-1}$ Sens. 2: $0.04 \text{dec} \cdot (\%RH)^{-1}$	22-80%	$18~/~37~\mathrm{s}$	This Work
Timbó ash	Impodimotric	Sens. 1: $0.13 \text{dec} \cdot (\%RH)^{-1}$ Sens. 2: $0.05 \text{dec} \cdot (\%RH)^{-1}$	23-80%	$12~/~46~\mathrm{s}$	This Work

was not employed in any of the biomass-based devices, which distinguishes this work from the others. As previously discussed, sensitivity is not standardized across studies and should be regarded merely as a calibration factor. Concerning the relative humidity (RH) limits, the limit of detection (LoD) is not defined in every study, and most papers report the limits as the lowest and highest concentrations tested, therefore, comparisons of the lower limit should consider this. Additionally, 80% RH is the highest value reached in the experimental setup used in this work, which does not imply that the sensor cannot operate at higher concentrations. Regarding response and recovery times, the values align with those found in the literature, although some of the lower values reported in Table 3 do not follow the same definitions used in this work.

4

Conclusions

This work focused on the production of humidity sensors based on ash from Acacia Negra and Timbó, the characterization of these materials, and the analysis of their humidity sensing behavior through electric impedance spectroscopy. A preparation method was developed that consistently produced functional sensors exhibiting exponential responses to changes in relative humidity. The materials were structurally characterized using SEM, EDS, XPS and FTIR. EDS analysis revealed a predominance of O, Ca, C and K in the center of the deposition area while the borders exhibited mainly O, C and K. FTIR analysis suggested the presence of $CaCO_3$, which was experimentally tested and found not to contribute to the sensing response of the devices. The sensors' characterization was carried out by analyzing the modulus of the electric impedance at 1 kHz across varying humidity levels, revealing two distinct operating regimes: regime 1 for RH < 50%, and regime 2 for RH > 50%. The sensitivities obtained for the Acácia Negra-based devices were $0.10 \, \mathrm{dec} \cdot (\%RH)^{-1}$ (regime 1) and $0.04 \, \mathrm{dec} \cdot (\%RH)^{-1}$ (regime 2), while for the Timbó-based devices, the sensitivities were $0.13 \, \mathrm{dec} \cdot (\%RH)^{-1}$ (regime 1) and $0.05 \, \mathrm{dec} \cdot (\%RH)^{-1}$ (regime 2). The limits of detection were 22% RH for Acácia Negra and 23% RH for Timbó. Response and recovery times were measured at 18 s and 37 s for Acácia Negra, and 12 s and 46 s for Timbó, respectively. An equivalent circuit model was proposed, consisting of a constant phase element (CPE) representing the base material and a series (R-CPE) association representing the ionic conduction due to humidity interaction.

Future Work

Ahead are some of the potential future works related to this project:

- 1. Fully characterize the sensors at other frequencies with due statical analysis.
- 2. Characterize sensor behavior under DC conditions, as a low frequency limit. This would contribute to a deeper understanding of the material's electrical behavior and further validate the equivalent circuit model proposed.
- 3. Test the sensor response to volatile organic compounds (VOCs) such as ethanol, acetone, or formaldehyde. This exploration would assess the potential application of the material beyond humidity sensing, extending to environmental or health-related monitoring.
- 4. Perform long-term stability studies. Extended tests under cyclic humidity conditions and over long durations would assess sensor durability, signal drift, and hysteresis effects. These studies are essential for evaluating the long-term viability of the devices in real-world applications.
- Evaluating how temperature affects the humidity response. This could lead to the development of compensation strategies or sensor calibration techniques for improved accuracy.
- 6. Integrating the sensors into compact, low-power systems suitable for IoT applications.
- 7. Investigating the combination of ash with other materials, such as carbon nanotubes (CNTs) to improve the conductivity, or polymers to enhance the sensitivity fo the devices.
- 8. Investigate the use of eco-friendly or biodegradable substrates to further enhance the sustainability of the sensor platform.

- [1] P. Wolkoff, "Indoor air humidity revisited: Impact on acute symptoms, work productivity, and risk of influenza and covid-19 infection," *International journal of hygiene and environmental health*, vol. 256, p. 114313, 2024.
- [2] N. Goad and D. Gawkrodger, "Ambient humidity and the skin: the impact of air humidity in healthy and diseased states," *Journal of the European Academy of Dermatology and Venereology*, vol. 30, no. 8, pp. 1285–1294, 2016.
- [3] G. Guarnieri, B. Olivieri, G. Senna, and A. Vianello, "Relative humidity and its impact on the immune system and infections," *International Journal of Molecular Sciences*, vol. 24, no. 11, 2023.
- [4] S. Shenoy, N. Pathak, A. Molins, A. Toncheva, T. Schouw, A. Hemberg, F. Laoutid, and P. V. Mahajan, "Impact of relative humidity on ethylene removal kinetics of different scavenging materials for fresh produce industry," *Postharvest Biology and Technology*, vol. 188, p. 111881, 2022.
- [5] R. Ambat and K. Piotrowska, "Chapter 1 humidity and electronics: corrosion perspectives," in *Humidity and Electronics* (R. Ambat and K. Piotrowska, eds.), pp. 1–18, Woodhead Publishing, 2022.
- [6] A. V. Arundel, E. M. Sterling, J. H. Biggin, and T. D. Sterling, "Indirect health effects of relative humidity in indoor environments.," *Environmental health perspectives*, vol. 65, pp. 351–361, 1986.
- [7] Q. Zhang, Y. Li, Q. Zhang, F. Ma, and X. Lü, "Application of deep dehumidification technology in low-humidity industry: A review," *Renewable and Sustainable Energy Reviews*, vol. 193, p. 114278, 2024.

[8] X. Su, Y. Geng, L. Huang, S. Li, Q. Wang, Z. Xu, and S. Tian, "Review on dehumidification technology in low and extremely low humidity industrial environments," *Energy*, p. 131793, 2024.

- [9] H. Ma, J. Ding, Z. Zhang, Q. Gao, Q. Liu, G. Wang, W. Zhang, and X. Fan, "Recent advances in graphene-based humidity sensors with the focus on structural design: A review," *IEEE Sensors Journal*, vol. 24, no. 12, pp. 20289–20314, 2024.
- [10] H. M. Mutee ur Rehman, M. Khan, M. M. Rehman, S. A. Khan, and W. Y. Kim, "High-performance humidity sensor for multipurpose applications by recycling of potato peel bio-waste," *Sensors and Actuators A: Physical*, vol. 343, p. 113662, 2022.
- [11] L. Sun, A. A. Haidry, Z. Li, L. Xie, Z. Wang, Q. Fatima, and Z. Yao, "Effective use of biomass ash as an ultra-high humidity sensor," *Journal of Materials Science: Materials in Electronics*, vol. 29, no. 21, pp. 18502–18510, 2018.
- [12] P. H. Zanella, "Caracterização e aplicação de cinzas de acácia-negra e timbó: Sensores químicos," dissertação de mestrado, Universidade Federal do Paraná, Curitiba, 2022. Pós-graduação em Física. Orientador: Prof. Dr. José Pedro Mansueto Serbena.
- [13] J. Janata, Principles of Chemical Sensors. Springer New York, NY, 2 ed., 2009.
- [14] J. R. Stetter, W. R. Penrose, and S. Yao, "Sensors, chemical sensors, electrochemical sensors, and ecs," *Journal of The Electrochemical Society*, vol. 150, no. 2, pp. S11–S16, 2003.
- [15] C. McDonagh, C. S. Burke, and B. D. MacCraith, "Optical chemical sensors," *Chemical Reviews*, vol. 108, no. 2, pp. 400–422, 2008.
- [16] A. Buzek, K. Serwańska-Leja, A. Zaworska-Zakrzewska, and M. Kasprowicz-Potocka, "The shape of the nasal cavity and adaptations to sniffing in the dog (canis familiaris) compared to other domesticated mammals: A review article," *Animals*, vol. 12, no. 4, p. 517, 2022.
- [17] K. Schurer, "Comparison of sensors for measurement of air humidity," in *Properties of Water in Foods* (D. Simatos and J. L. Multon, eds.), vol. 90 of *NATO ASI Series*, pp. 647–660, Springer, Dordrecht, 1985.

[18] H. Farahani, R. Wagiran, and M. N. Hamidon, "Humidity sensors principle, mechanism, and fabrication technologies: A comprehensive review," Sensors, vol. 14, no. 5, pp. 7881–7939, 2014.

- [19] N. Yamazoe and Y. Shimizu, "Humidity sensors: Principles and applications," *Sensors and Actuators*, vol. 10, no. 3-4, pp. 379–398, 1986.
- [20] E. Traversa, "Ceramic sensors for humidity detection: The state-of-the-art and future developments," Sensors and Actuators B: Chemical, vol. 23, no. 2-3, pp. 135–156, 1995.
- [21] M. F. Mario Pelino, C. Cantalini, "Principles and applications of ceramic humidity sensors," Miscellaneous, vol. 16, no. 2, pp. 69–87, 1993.
- [22] N. Alam, Abid, and S. S. Islam, "Advancements in trace and low humidity sensors technologies using nanomaterials: A review," *ACS Applied Nano Materials*, vol. 7, no. 12, pp. 13836–13864, 2024.
- [23] Z. Ma, T. Fei, and T. Zhang, "An overview: Sensors for low humidity detection," Sensors and Actuators B: Chemical, vol. 376, p. 133039, 2023.
- [24] "Hih series humidity sensors; psychrometrics and moisture, reference and application data," tech. rep., Honeywell, Morristown, NJ, USA, 2010. Technical report.
- [25] J. M. Wallace and P. V. Hobbs, *Atmospheric Science: An Introductory Survey*. Academic Press, 2006.
- [26] M. Sajid, Z. J. Khattak, K. Rahman, G. Hassan, and K. H. Choi, "Progress and future of relative humidity sensors: a review from materials perspective," *Bulletin of Materials Science*, vol. 45, no. 4, p. 238, 2022.
- [27] J. Fraden, Handbook of Modern Sensors: Physics, Designs, and Applications. Springer New York, NY, 4 ed., 2010.
- [28] H. J. Kreuzer and Z. W. Gortel, *Physisorption Kinetics*, vol. 1 of *Springer Series in Surface Sciences*. Springer Berlin, Heidelberg, 1986.
- [29] S.-J. Park and M.-K. Seo, *Chapter 2 Solid-Gas Interaction*, vol. 18 of *Interface Science and Technology*, pp. 59–145. Elsevier, 2011.

[30] J. P. Gaspard, "Physisorption and chemisorption," in *Interfacial Aspects of Phase Trans*formations (B. Mutaftschiev, ed.), (Dordrecht), pp. 103–118, Springer Netherlands, 1982.

- [31] A. H. Berger and A. S. Bhown, "Comparing physisorption and chemisorption solid sorbents for use separating co2 from flue gas using temperature swing adsorption," *Energy Procedia*, vol. 4, pp. 562–567, 2011. 10th International Conference on Greenhouse Gas Control Technologies.
- [32] B. Arman Kuzubasoglu, "Recent studies on the humidity sensor: A mini review," ACS Applied Electronic Materials, vol. 4, no. 10, pp. 4797–4807, 2022.
- [33] N. Agmon, "The grotthuss mechanism," *Chemical Physics Letters*, vol. 244, no. 5, pp. 456–462, 1995.
- [34] D. Marx, M. Tuckerman, J. Hutter, and M. Parrinello, "The nature of the hydrated excess proton in water," *Nature*, vol. 397, pp. 601–604, Feb. 1999.
- [35] C. I. G. Martinez, Gas Sensors of Volatile Organic Compounds (VOCs) Mixtures. Phd thesis, Universidade Federal do Paraná (UFPR), Curitiba, Brazil, February 2024. Advisor: José Pedro Mansueto Serbena.
- [36] C. Bentz, L. Baudzus, and P. Krummrich, "Signal to noise ratio (snr) enhancement comparison of impulse-, coding- and novel linear-frequency-chirp-based optical time domain reflectometry (otdr) for passive optical network (pon) monitoring based on unique combinations of wavelength selective mirrors," *Photonics*, vol. 1, pp. 33–46, 03 2014.
- [37] Z. Zhuang, Y. Li, X. Li, and C. Zhao, "A novel polymer-salt complex based on licl doped speek/poly(ether ether ketone)-co-poly(ethylene glycol) for humidity sensors," *IEEE Sensors Journal*, vol. 21, no. 7, pp. 8886–8895, 2021.
- [38] Y. Gu, H. Jiang, Z. Ye, N. Sun, X. Kuang, W. Liu, G. Li, X. Song, L. Zhang, W. Bai, and X. Tang, "Impact of size on humidity sensing property of copper oxide nanoparticles," *Electronic Materials Letters*, vol. 16, no. 1, pp. 61–71, 2020.
- [39] P. Songkeaw, K. Onlaor, T. Thiwawong, and B. Tunhoo, "Transparent and flexible humidity sensor based on graphene oxide thin films prepared by electrostatic spray deposition technique," *Journal of Materials Science: Materials in Electronics*, vol. 31, no. 15, pp. 12206–12215, 2020.

[40] S. Tachibana, Y.-F. Wang, T. Sekine, Y. Takeda, J. Hong, A. Yoshida, M. Abe, R. Miura, Y. Watanabe, D. Kumaki, and S. Tokito, "A printed flexible humidity sensor with high sensitivity and fast response using a cellulose nanofiber/carbon black composite," ACS Applied Materials & Interfaces, vol. 14, no. 4, pp. 5721–5728, 2022. PMID: 35067045.

- [41] S. Hajian, X. Zhang, P. Khakbaz, S.-M. Tabatabaei, D. Maddipatla, B. B. Narakathu, R. G. Blair, and M. Z. Atashbar, "Development of a fluorinated graphene-based resistive humidity sensor," *IEEE Sensors Journal*, vol. 20, no. 14, pp. 7517–7524, 2020.
- [42] Z. Duan, Y. Jiang, M. Yan, S. Wang, Z. Yuan, Q. Zhao, P. Sun, G. Xie, X. Du, and H. Tai, "Facile, flexible, cost-saving, and environment-friendly paper-based humidity sensor for multifunctional applications," ACS Applied Materials & Interfaces, vol. 11, no. 24, pp. 21840–21849, 2019.
- [43] D. Ziegler, F. Boschetto, E. Marin, P. Palmero, G. Pezzotti, and J. Tulliani, "Rice husk ash as a new humidity sensing material and its aging behavior," *Sensors and Actuators B: Chemical*, vol. 328, p. 129049, 2021.
- [44] L. Kumar, D. Saha, S. Khan, K. Sengupta, and T. Islam, "A medium-range hygrometer using nano-porous thin film of gamma-al2o3 with electronics phase detection," *IEEE Sensors Journal*, vol. 12, p. 1625, 10 2011.
- [45] G. R. Biswal, P. Mohanty, K. J. Akram, N. P. Padhy, and T. Islam, "Design and fabrication of an inexpensive capacitive humidity sensor for smart sub-station automation," *IEEE Sensors Journal*, vol. 20, no. 12, pp. 6215–6223, 2020.
- [46] Y. Zhou, "Research on the potential of biomass as a chemical energy source," *Applied and Computational Engineering*, vol. 70, pp. 14–18, 2024.
- [47] K. Zhang, "A review of biomass energy: Comparison of utilization methods and future prospects," E3S Web of Conferences, vol. 606, p. 05007, 2025.
- [48] F. Grau, H. Choo, J. W. Hu, and J. Jung, "Engineering behavior and characteristics of wood ash and sugarcane bagasse ash," *Materials*, vol. 8, no. 10, pp. 6962–6977, 2015.
- [49] M. Okmanis, D. Lazdiņa, and A. Lazdiņš, "The composition and use value of tree biomass ash," *Rural Sustainability Research*, vol. 34, no. 329, pp. 32–37, 2015.

[50] M. F.-D. Juárez, G. Fabiani, T. Mazzier, D. Schönegger, G. Pietramellara, M. Gómez-Brandón, and H. Insam, "Reclamation of acid soils with biomass ashes from pyrolytic wood liquefaction," Waste and Biomass Valorization, vol. 11, pp. 5067–5078, 2020.

- [51] R. Wang, X. ZongGuo, R. Hu, J. Wu, Y. Xu, Z. Yu, L. Yang, G. Yan, J. Liu, and Y. Zhang, "Biomass ash as soil fertilizers: Supercharging biomass accumulation by shifting auxin distribution," *Chemosphere*, vol. 357, p. 141910, 2024.
- [52] A. A. Bogush, C. Dabu, V. D. Tikhova, J. K. Kim, and L. C. Campos, "Biomass ashes for acid mine drainage remediation," Waste and Biomass Valorization, vol. 11, no. 9, pp. 4977–4989, 2020.
- [53] J. Zhai, I. T. Burke, and D. I. Stewart, "Beneficial management of biomass combustion ashes," *Renewable and Sustainable Energy Reviews*, vol. 151, p. 111555, 2021.
- [54] C. Onfray and A. Thiam, "Biomass-derived carbon-based electrodes for electrochemical sensing: A review," *Micromachines*, vol. 14, no. 9, p. 1688, 2023.
- [55] N. S. Trivedi, S. A. Mandavgane, S. Mehetre, and B. D. Kulkarni, "Characterization and valorization of biomass ashes," *Environmental Science and Pollution Research*, vol. 23, no. 20, pp. 20243–20256, 2016.
- [56] G. Zając, J. Szyszlak-Bargłowicz, W. Gołębiowski, and M. Szczepanik, "Chemical characteristics of biomass ashes," *Energies*, vol. 11, no. 11, p. 2885, 2018.
- [57] S. K. Adhikary, D. K. Ashish, and Rudžionis, "A review on sustainable use of agricultural straw and husk biomass ashes: Transitioning towards low carbon economy," *Science of The Total Environment*, vol. 838, p. 156407, 2022.
- [58] V. Viola, M. Catauro, A. D'Amore, and P. Perumal, "Assessing the carbonation potential of wood ash for CO2 sequestration," *Low-carbon Materials and Green Construction*, vol. 2, no. 1, p. 12, 2024.
- [59] A. L. Mora, Aumento da produção de sementes geneticamente melhoradas de Acacia mearnsii De Wild. (acácia-negra) no Rio Grande do Sul. Tese de doutorado, Universidade Federal do Paraná (UFPR), Curitiba, Brasil, 2013.

[60] R. C. V. Higa, M. S. Wrege, S. Mochiutti, A. L. Mora, A. R. Higa, and A. A. Simon, "Acácia negra," in Agrometeorologia dos cultivos: o fator meteorológico na produção agrícola (J. E. B. A. Monteiro, ed.), pp. 313–319, Brasília, DF: Instituto Nacional de Meteorologia, 2009.

- [61] D. J. Boland, M. Brooker, G. Chippendale, N. Hall, B. Hyland, R. Johnston, D. Kleinig, and J. Turner, Forest trees of Australia, vol. 96. Thomas Nelson and CSIRO Melbourne, 1984.
- [62] A. G. Júnior, A. F. dos Santos, A. R. Higa, A. L. Mora, A. A. Simon, C. G. Auer, E. T. Iede, G. R. Curcio, H. R. Rodigheri, R. A. Dedecek, R. C. V. Higa, S. S. Keil, and S. do Rocio Chiarello Penteado, "Cultivo da acácia-negra," boletim técnico, Embrapa Florestas, Colombo, PR, 2016.
- [63] M. Fagg and A. N. B. Gardens, "Acácia-negra (acacia mearnsii)." https://www.cienciaeclima.eco.br/2019/09/potencial-da-acacia-negra-para.html, 2019. Image credit as cited: Australian National Botanic Gardens / Fagg, M.
- [64] P. E. R. Carvalho, "Timbó (*Ateleia glazioveana* baill.): Características silviculturais e possibilidades de uso," Tech. Rep. 57, Embrapa Florestas, Colombo, PR, 2002.
- [65] J. N. Vasconcelos, G. M. P. Santiago, J. Q. Lima, J. Mafezoli, T. L. G. D. Lemos, F. R. L. Da Silva, M. A. S. Lima, A. T. A. Pimenta, R. Braz-Filho, A. M. C. Arriaga, and D. Cesarin-Sobrinho, "Ateleia glazioveana and ocimum basilicum: plants with potential larvicidal and repellent against aedes aegypti (diptera, culicidae)," Research, Society and Development, vol. 10, no. 17, p. e228101724733, 2021.
- [66] P. E. R. Carvalho, "Timbó (Ateleia glazioveana baill.)," in Espécies Arbóreas Brasileiras, vol. 1, pp. 893–899, Brasília; Colombo: Embrapa Informação Tecnológica; Embrapa Florestas, 2003.
- [67] Y. Okano, *Scanning Electron Microscopy*, pp. 563–569. Singapore: Springer Singapore, 2018.
- [68] D. N. Leonard, G. W. Chandler, and S. Seraphin, Scanning Electron Microscopy, pp. 1–16.
 John Wiley Sons, Ltd, 2012.

[69] X. Ming-lian, "The application of scanning electron microscopy in unknown plastic appraisal research," China Plastics Industry, 2015.

- [70] J. Lefebvre, F. Galli, C. L. Bianchi, G. S. Patience, and D. C. Boffito, "Experimental methods in chemical engineering: X-ray photoelectron spectroscopy-xps," *The Canadian Journal of Chemical Engineering*, vol. 97, no. 10, pp. 2588–2593, 2019.
- [71] G. Greczynski, R. Haasch, N. Hellgren, E. Lewin, and L. Hultman, "X-ray photoelectron spectroscopy of thin films," *Nature Reviews Methods Primers*, vol. 3, 2023.
- [72] K. Wilson and A. F. Lee, Appendix K: X-Ray Photoelectron Spectroscopy (XPS), pp. 493–496. John Wiley Sons, Ltd, 2009.
- [73] D. N. Krishna and J. Philip, "Review on surface-characterization applications of x-ray photoelectron spectroscopy (xps): Recent developments and challenges," *Applied Surface Science Advances*, 2022.
- [74] C. Berthomieu and R. Hienerwadel, "Fourier transform infrared (ftir) spectroscopy," *Photosynthesis Research*, vol. 101, pp. 157–170, 2009.
- [75] J. Gaffney, N. Marley, and D. E. Jones, "Fourier transform infrared (ftir) spectroscopy," Characterization of Materials, pp. 1–33, 2012.
- [76] Y. Gong, X. Chen, and W. Wu, "Application of fourier transform infrared (ftir) spectroscopy in sample preparation: Material characterization and mechanism investigation," *Advances in Sample Preparation*, 2024.
- [77] V. T. Mangam, D. Narla, R. K. Konda, and P. N. K. Sarella, "Beyond the spectrum: Exploring unconventional applications of fourier transform infrared (ftir) spectroscopy," *Asian Journal of Pharmaceutical Analysis*, vol. 14, no. 2, pp. 86–94, 2024.
- [78] T. Zhang, Y. He, R. Wang, W. Geng, L. Wang, L. Niu, and X. Li, "Analysis of dc and ac properties of humidity sensor based on polypyrrole materials," *Sensors and Actuators B: Chemical*, vol. 131, no. 2, pp. 687–691, 2008.
- [79] A. Labidi, C. Jacolin, M. Bendahan, A. Abdelghani, J. Guérin, K. Aguir, and M. Maaref, "Impedance spectroscopy on wo3 gas sensor," Sensors and Actuators B: Chemical, vol. 106, no. 2, pp. 713–718, 2005.

[80] A. Pathak, S. Samanta, M. Kaur, and A. Singh, "Impedance spectroscopy studies revealing the influence of zno-rgo heterojunction interface on no2 sensing," Synthetic Metals, vol. 301, p. 117525, 2024.

- [81] A. C. Lazanas and M. I. Prodromidis, "Electrochemical impedance spectroscopya tutorial," ACS Measurement Science Au, vol. 3, no. 3, pp. 162–193, 2023.
- [82] M. Orazem and B. Tribollet, "A Tutorial on Electrochemical Impedance Spectroscopy," *Chem Texts*, vol. 6, p. 12, June 2020.
- [83] O. Heaviside, *Electrical Papers*. London, New York: Macmillan and Co., 1892. Available online: Vol. 1, Vol. 2, Vol. 2 (Harvard).
- [84] E. Warburg, "Ueber das verhalten sogenannter unpolarisirbarer elektroden gegen wechselstrom," *Annalen der Physik*, vol. 303, no. 3, pp. 493–499, 1899.
- [85] K. S. Cole and R. H. Cole, "Dispersion and absorption in dielectrics i. alternating current characteristics," *The Journal of Chemical Physics*, vol. 9, pp. 341–351, 04 1941.
- [86] J. E. B. Randles, "Kinetics of rapid electrode reactions," *Discuss. Faraday Soc.*, vol. 1, pp. 11–19, 1947.
- [87] A. Lasia, Electrochemical Impedance Spectroscopy and its Applications. New York, NY: Springer, 2014 ed., June 2014.
- [88] D. D. Macdonald, "Reflections on the history of electrochemical impedance spectroscopy," *Electrochimica Acta*, vol. 51, no. 8, pp. 1376–1388, 2006. Electrochemical Impedance Spectroscopy.
- [89] J. R. Macdonald and W. B. Johnson, Fundamentals of Impedance Spectroscopy, ch. 1, pp. 1–20. John Wiley Sons, Ltd, 2018.
- [90] B. T. Mark E. Orazem, Electrical Circuits, ch. 4, pp. 75–88. John Wiley Sons, Ltd, 2017.
- [91] K. Ariyoshi, Z. Siroma, A. Mineshige, M. Takeno, T. Fukutsuka, T. Abe, and S. Uchida, "Electrochemical impedance spectroscopy part 1: Fundamentals," *Electrochemistry*, vol. 90, no. 10, pp. 102007–102007, 2022.

[92] G. M. G. da Silva, P. M. Faia, S. R. Mendes, and E. S. Araújo, "A review of impedance spectroscopy technique: Applications, modelling, and case study of relative humidity sensors development," *Applied Sciences*, vol. 14, no. 13, 2024.

- [93] J. Aguilar, M. Beadle, P. Thompson, and M. Shelley, "The microwave and rf characteristics of fr4 substrates," in *IEE Colloquium on Low Cost Antenna Technology (Ref. No. 1998/206)*, pp. 2/1–2/6, 1998.
- [94] Y. Xia and X. Xie, "Reliability of lead-free solder joints with different pcb surface finishes under thermal cycling," *Journal of Alloys and Compounds*, vol. 454, no. 1, pp. 174–179, 2008.
- [95] ASTM International, "ASTM D1762-84(2013): Standard Test Method for Chemical Analysis of Wood Charcoal." https://www.astm.org/D1762-84R13.html, 2013. ASTM International, West Conshohocken, PA.
- [96] Sensirion AG, SHTC3 Humidity and Temperature Sensor: Datasheet, 2021. Accessed: 2025-05-07.
- [97] PalmSens, "Multiemstat4: Portable multi-channel potentiostat." Online. Accessed: Mar. 27, 2025.
- [98] PalmSens, "Multitrace: Software for multi-channel measurements." Online. Accessed: Mar. 27, 2025.
- [99] The Pandas Development Team, "pandas: Python data analysis library." Online, 2024. Accessed: Mar. 27, 2025.
- [100] The NumPy Development Team, "Numpy: The fundamental package for array computing with python." Online, 2024. Accessed: Mar. 27, 2025.
- [101] Plotly Technologies Inc., "Plotly: Python graphing library." Online, 2024. Accessed: Mar. 27, 2025.
- [102] Joshua T. White and Contributors, "impedance.py: A python package for electrochemical impedance analysis." Online, 2024. Accessed: Mar. 27, 2025.

[103] S. V. Vassilev, C. G. Vassileva, and N. L. Petrova, "Mineral carbonation of biomass ashes in relation to their co2 capture and storage potential," ACS Omega, vol. 6, no. 22, pp. 14598–14611, 2021. PMID: 34124483.

[104] W. Ahmad, B. Jabbar, I. Ahmad, B. Mohamed Jan, M. M. Stylianakis, G. Kenanakis, and R. Ikram, "Highly sensitive humidity sensors based on polyethylene oxide/cuo/multi walled carbon nanotubes composite nanofibers," *Materials*, vol. 14, no. 4, 2021.